Report for the

MUSE Beam Properties Review

December 7, 2018

R. Gilman,[1] E.J. Downie,[2] S. Strauch,[3] E. Cline,[1]

I. P. Fernando,[4] W. Lin,[1] P.E. Reimer,[5] and P. Roy[6]

(for the MUSE Collaboration)

[1] *Rutgers University, New Brunswick, New Jersey, USA*

[2] *George Washington University, Washington, DC, USA*

[3] *University of South Carolina, Columbia, South Carolina, USA*

[4] *Hampton University, Hampton, Virginia, USA*

[5] *Argonne National Lab, Argonne, IL, USA*

[6] *University of Michigan, Ann Arbor, Michigan, USA*

The MUSE experiment will address the proton radius puzzle through a precise measurement of simultaneous elastic muon and electron scattering on the proton. Through comparisons of test measurements with simulations using tools including TURTLE, G4beamline, and GEANT4, we demonstrate that the properties of the PiM1 channel are well understood for the MUSE experiment. This report summarizes our findings.

CONTENTS

I. INTRODUCTION

The MUSE experiment requires that the beam momentum in the PiM1 channel be known to 0.2 - 0.3%. This requirement is determined by the effect of the uncertainty of the beam momentum on the elastic scattering cross sections measured in the experiment. The arguments leading to this goal are summarized in Appendix A.

In light of this requirement and the measurements and understanding of the PiM1 channel presented, the BV49 subcommittee report called for a separate beam properties review in the subcommittee report, explicitly requesting the following:

- Modelling of the source distributions for different particle types, to ensure that the small differences observed between beam properties of pions, muons, and electrons are consistent with expectations.
- Discussion of all relevant issues related to beam line simulations, including:
  - Clarification of the discrepancies presented between the G4beamline vs. TURTLE simulations of the PiM1 beam line.
  - Discussion of the properties of the beam line employed as a spectrometer.
  - A description of beam properties measurements taken, and presentation of an error budget associated with the critical electron/muon momentum measurements.

- A clear demonstration that the beam line is sufficiently well understood and systematic effects are under control.

The BV49 subcommittee report on the PSI PiM1 MUSE experiment is reproduced in Appendix B. In this report, we describe the PiM1 channel including the M production target, and then proceed to discuss simulations and data that address the issues identified above.

We consider it consistent with the BV49 subcommittee request that for this beam property review we do not go further into details of the experiment, its physics measurements, or its systematics, other than some descriptions of the apparatus used for measurements of the beam properties presented here. We do not discuss in this report the beam fluxes or the effects of the beam line detectors on the beam, except for the corrections needed to get the momentum of particles coming out of the PiM1 channel into the apparatus.

A. The PiM1 channel

Figure 1 shows the magnetic elements in the PiM1 channel. Since the channel bends the beam to the left in a horizontal plane, the transport coordinates are $+z$ along the beam direction, $+x$ to beam right, and $+y$ vertically downward. The fields of the initial quads QTA1 and QTB1 focus (defocus) the beam in the y (x) direction, QTB2 (de)focuses in the orthogonal directions. The slits FS11 control beam intensity with little effect on the beam spot. The dipole magnet ASM11 along with the quad pair QSL11 + QSL12 generate a momentum dispersed beam spot at the IFP with a nominal dispersion of 7 cm/%. The quad pair QSL13 + QSL14 and dipole magnet ASM12 are set symmetrically about the IFP so that a beam with no momentum dispersion is generated. Finally, the quad pairs QSL15 + QSL16 and QSL17 + QSL18 focus the beam into a spot at the target region. Note that the path length shown in Fig. 1 assumes that particles travel straight through the dipole magnets with a sharp bend at the center of each magnet. Beam particles actually travel along an arc in the dipoles, shortening the path length in each dipole by approximately 27 cm, so that particle trajectories through the channel are 23.12 m long.

The PiM1 secondary beam is produced when the 50.6 MHz, 590 MeV primary proton beam crosses the flange of the graphite disk of the M production target, shown in Fig. 2.

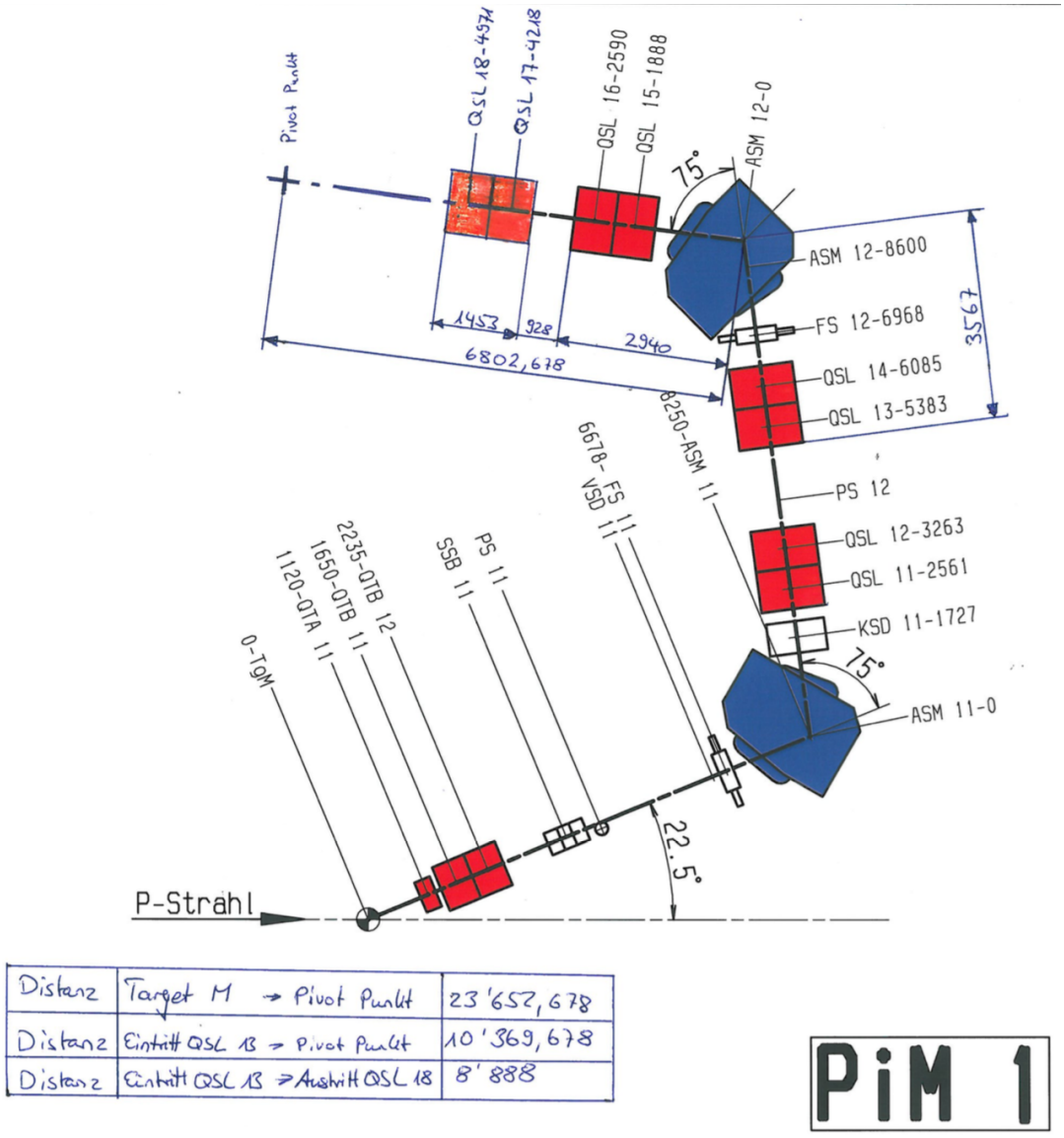

FIG. 1: Magetic elements in the PiM1 channel.

The PiM1 channel "looks" at the M target nearly parallel to the graphite flange, so that the 5-mm, 6σ width of the beam is reduced to the 2-mm transverse (x) full width of the flange. The beam is also taken to be ± 1 mm width in the vertical y direction.

Pions are produced in strong interactions through $pC \to \pi X$. Muons are generated by pion decays, $\pi \to \mu\overline{\nu_\mu}$. Electrons (and positrons) are generated from neutral pion decays. Most common ($\approx$99.8% branching ratio) is $\pi^0 \to \gamma\gamma$ followed by γ conversion in the graphite: $\gamma C \to e^+e^-X$. There is also a small branching ratio ($\approx$1.2%) for Dalitz

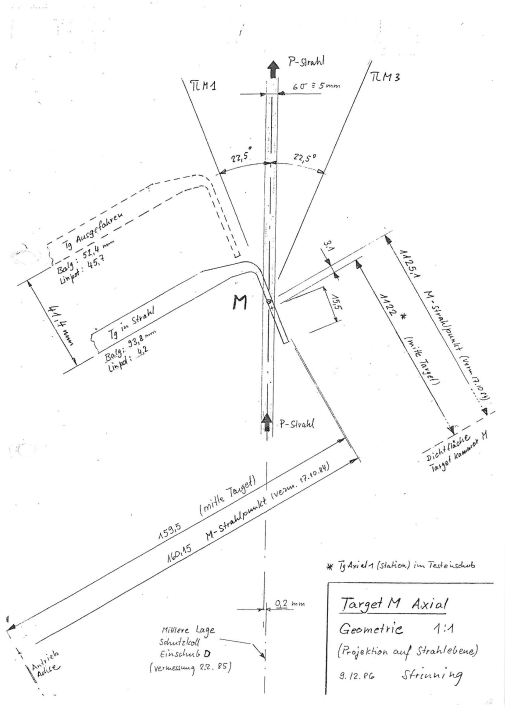

FIG. 2: Geometry of M production target where the PiM1 beam is generated.

decay, $\pi^0 \to e^+e^-\gamma$. Section II B discusses the muon and electron + positron sources in detail.

II. SIMULATIONS OF BEAM PROPERTIES

A. Default TURTLE Simulation of beam properties

1. Simulation Input

The default description of the PiM1 channel was implemented in TURTLE [1]. A sample input deck for a TURTLE calculation of PiM1 is shown in Appendix C. Our description includes some upgrades to the standard description, developed with Davide Reggiani of PSI, that implement the latest position database for magnetic elements, slightly adjusted quadrupole magnetic lengths (to match original quad field measurements), and a more extensive set of apertures including some beam pipe and vacuum chamber elements that were previously omitted from the simulation. All together, the upgrades lead to only minor

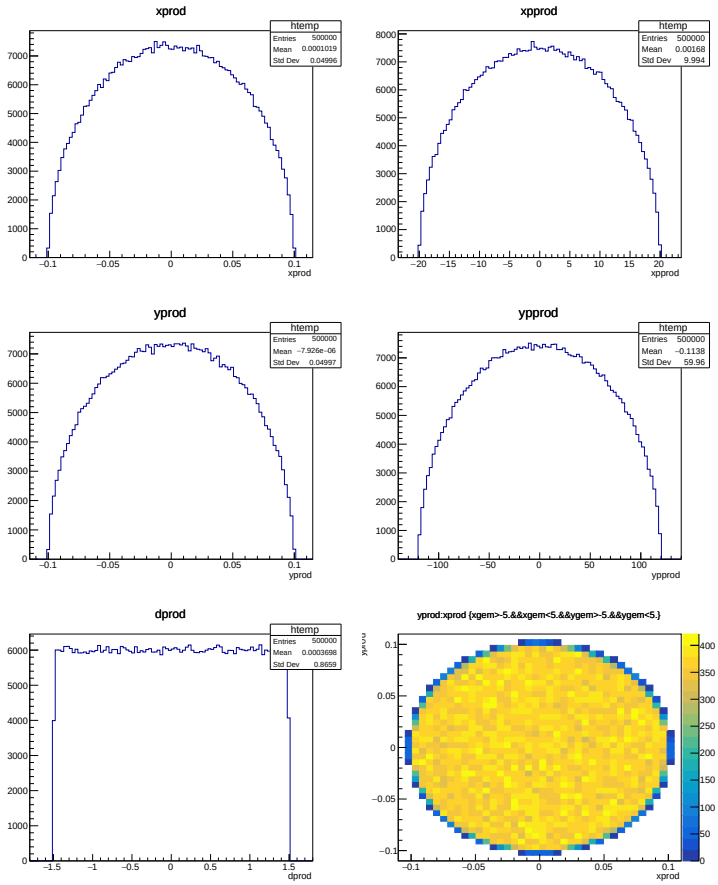

FIG. 3: Default PiM1 "point" source distributions in TURTLE. ***Upper left***: position distribution in x. ***Upper right***: x', the angular distribution in x. ***Center left***: position distribution in y. ***Center right***: y', the angular distribution in y. ***Lower left***: momentum distribution δ in % from nominal momemtum. ***Lower right***: positon distribution y vs x at source for particles which reach the plane of the GEM chambers.

changes in the beam spot and channel matrix elements. Our default calculation uses a muon beam with 155 MeV/c central momentum. Since PiM1 is a magnetic channel, the channel calculations are independent of particle type and beam momentum, as long as we do not take into account decays in flight, scattering from vacuum chamber and pole face elements, and differences in source distributions.

Figure 3 shows our default TURTLE "point-like" source, while Fig. 4 shows the source distributions of particles successfully transported through the magnets to the PiM1 target region. Unless otherwise stated, all plots shown have positions x and y in units of cm,

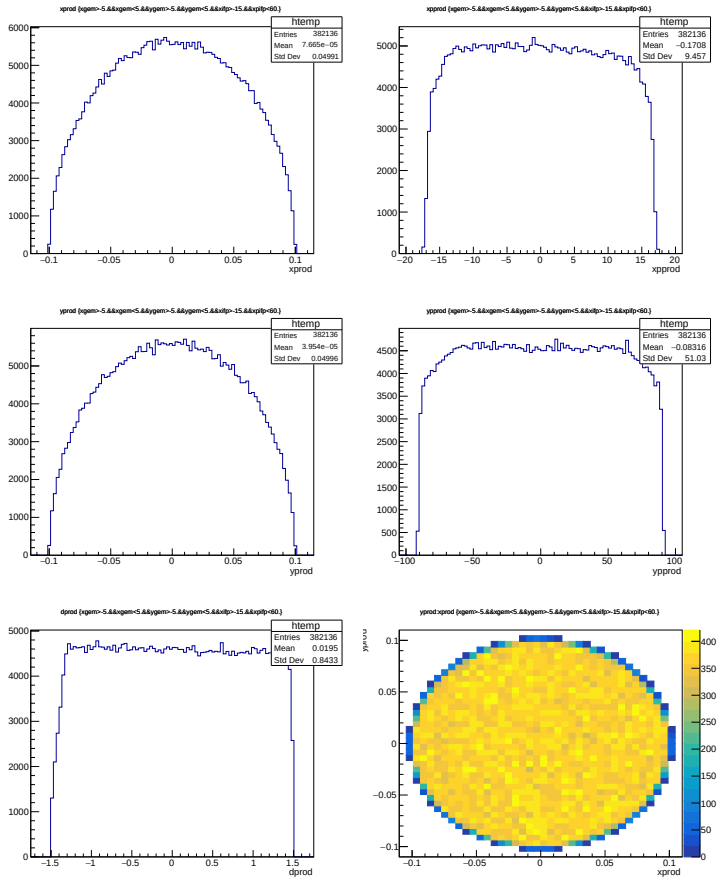

FIG. 4: PiM1 source distributions for particles that reach the plane of the GEM chambers, in the PiM1 target region, for a "point" source. ***Upper left***: position distribution in x. ***Upper right***: x', the angular distribution in x. ***Center left***: position distribution in y. ***Center right***: y', the angular distribution in y. ***Lower left***: momentum distribution δ in % from nominal momemtum. ***Lower right***: positon distribution y vs x at source.

angles x' and y' in units of mr, and momentum δ in units of %. The beam size is ± 1 mm beam size in both x and y. The range of angles thrown needs to be about ± 20 (100) mr in x (y). The momentum range is $\pm 1.5\%$. The beam distributions at the GEM chambers are smaller than the chambers themselves, so it is mainly the PiM1 channel itself that limits the distributions of Fig. 4. There are a small number of events that scatter from beam line apertures and end up at extreme positions at the GEM chambers, which removes a few events from Fig. 4.

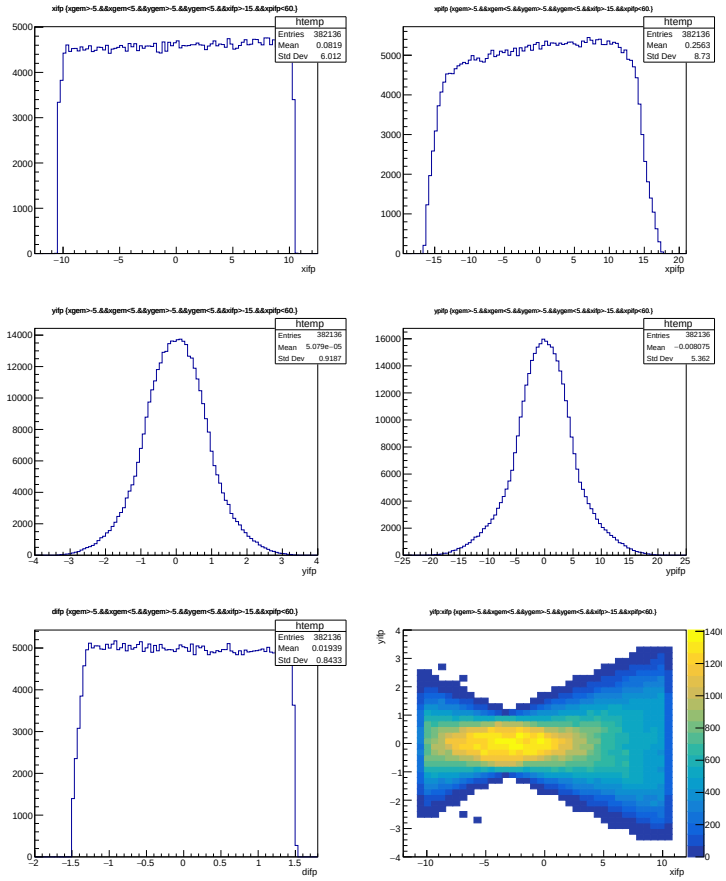

FIG. 5: Particle distributions at the IFP, for a "point" source. ***Upper left***: position distribution in x. ***Upper right***: x', the angular distribution in x. ***Center left***: position distribution in y. ***Center right***: y', the angular distribution in y. ***Lower left***: momentum distribution δ in % from nominal momemtum. ***Lower right***: positon distribution y vs x at IFP.

2. Distributions and Correlations in the PiM1 Channel

Figure 5 shows the resulting particle distributions at the Intermediate Focal Point (IFP). The beam at the IFP is only a few cm high, but about 21 cm wide, reflecting the momentum dispersion and range. The angle range is limited, with nearly parallel trajectories. The waist in the beam is not centered in $x_{\rm IFP}$, which could be adjusted by small changes in the default magnetic fields.

Figure 6 shows the resulting particle distributions at the PiM1 scattering target position. The beam is cm sized in x but smaller in y. The asymmetry in x and x' reflects that the

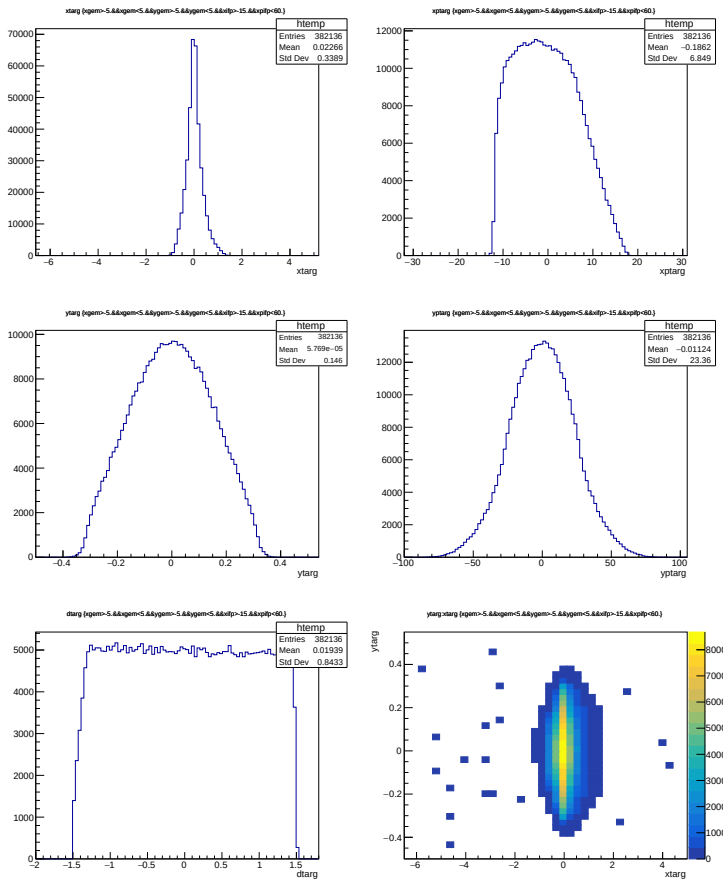

FIG. 6: Particle distributions at the PiM1 target, for a "point" source. ***Upper left***: position distribution in x. ***Upper right***: x', the angular distribution in x. ***Center left***: position distribution in y. ***Center right***: y', the angular distribution in y. ***Lower left***: momentum distribution δ in % from nominal momemtum. ***Lower right***: positon distribution y vs x.

beam bends horizontally; the y coordinates are close to symmetric. The beam has a better focus in position in y, but a worse focus in angle in y'. Aperture scattering leads to a small number of events (about 1 in 10,000) mainly at $-x$, the "low-momentum" side of the beam – there is little to no actual momentum dispersion within the beam spot, as will be shown below.

The distributions can be better understood by looking at correlations between parameters at a given location and at the beam transport matrix elements. Figure 7 shows parameter correlations at the IFP. The top panels show that there is only a small correlation in x' vs. x, while y' vs. y indicates a mild de-focusing. The middle panels indicate the

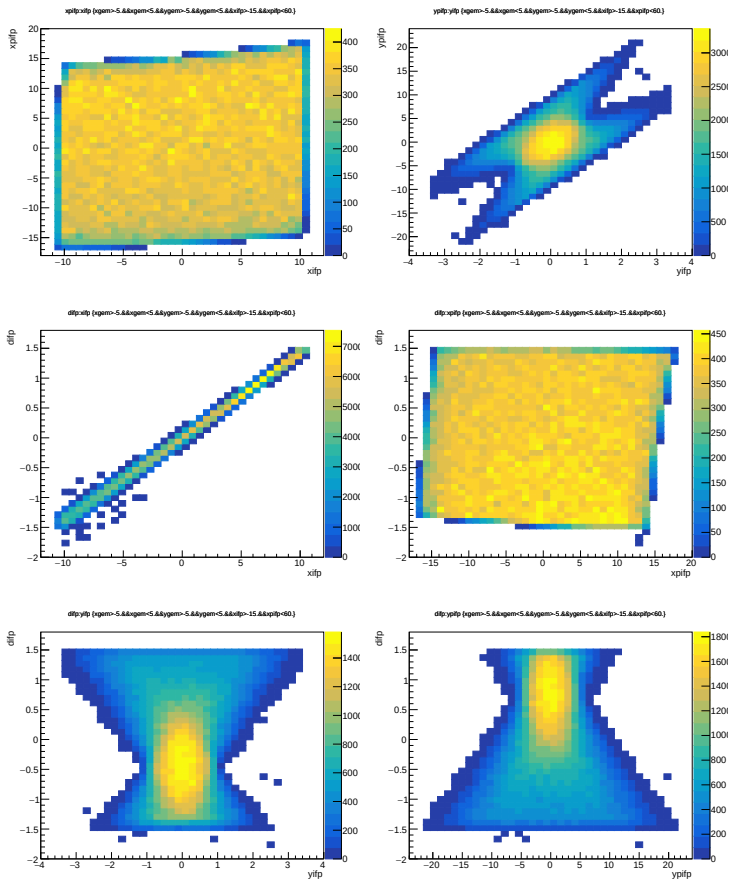

FIG. 7: Correlations at the IFP, for a "point" source. ***Upper left***: x' vs x. ***Upper right***: y' vs y. ***Center left***: δ vs x. ***Center right***: δ vs x'. ***Lower left***: δ vs y. ***Lower right***: δ vs y'.

7 cm/% dispersion in x but little correlation with x'. The δ vs. x correlation is broadened by $\approx \pm 0.1\%$ from the width of the source. The lower panels indicate that for any given δ, the distributions are symmetric about $y = 0$ and $y' = 0$, but the ranges in y vary with δ. There is no first order matrix element connecting y or y' with δ.

Figure 8 shows parameter correlations at the PiM1 scattering target. One can see few-event tails in most distributions from aperture scattering. The top panels show that there are a few events that generate interesting tails in x' vs. x, but no correlation in y' vs. y. Examining in the left column δ vs. x and y, on average particles at any momentum are at $x = y = 0$, but central momentum particles tend to be more at small x over the full range of y, while particles at the ends of the momentum range tend to be at relatively smaller

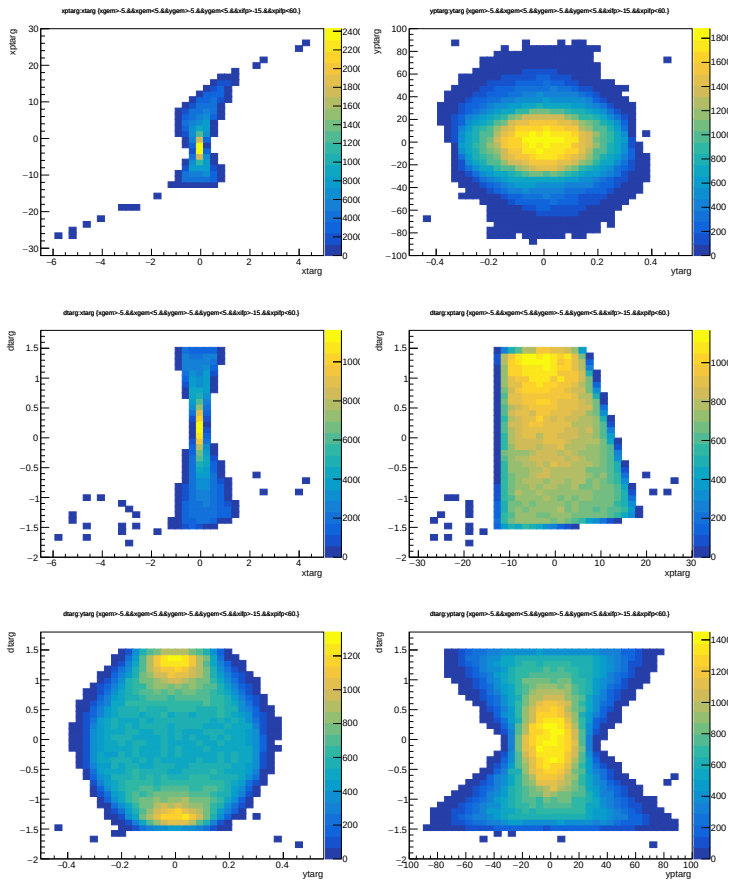

FIG. 8: Correlations at the target, for a "point" source. ***Upper left***: x' vs x. ***Upper right***: y' vs y. ***Center left***: δ vs x. ***Center right***: δ vs x'. ***Lower left***: δ vs y. ***Lower right***: δ vs y'.

y over the full range of x. The waist in δ vs. y' is nicely centered about $\delta = y' = 0$, while the waist in δ vs. x is slightly offset from the origin.

We close this section with the remark that the correlations seen in the simulations are washed out in simulations that use an extended target, which tends to broaden the distributions, as well as being washed out experimentally, as we do not have the few ps time resolution needed to precisely measure the momentum on an event by event basis.

3. P1M1 matrix elements and channel acceptance from TURTLE simulations

The PiM1 channel beam transport matrix elements can be studied in TURTLE simulations in multiple ways. Table I presents first-order matrix elements derived by comparing

	x_{prod}	x'_{prod}	y_{prod}	y'_{prod}	δ
$x_{\rm IFP}$	-1.225	-0.041 cm/mr	-0.085	0	7.07 cm/%
x'_{IFP}	-3.31 mr/cm	-0.932	-0.007 mr/cm	0	1.276 mr/%
y_{IFP}	0	0	10.08	-0.007 cm/mr	0
y'_{IFP}	0	0	53.28 mr/cm	0.062	0
x_{targ}	1.47	0.005 cm/mr	0.339	0	-0.078 cm/%
x'_{targ}	7.25 mr/cm	0.710	1.02 mr/cm	-0.002	-2.18 mr/%
y_{targ}	0	0	-0.316	-0.004 cm/mr	0
y'_{targ}	0	0	284.5 mr/cm	-0.031	0

TABLE I: First-order PiM1 beam transport matrix elements from TURTLE. The numerical values were calculated using offsets of 1 mm in position, 10 mr in angle, and 1% in momentum.

TURTLE calculations with one offset source parameter to calculations with a "pencil" beam with $x = x' = y = y' = \delta = 0$. There are several important points to note. Generally the matrix elements connecting y with x or δ are small. The 7 cm / % momentum dispersion at the IFP is reproduced to within 1% of this value. The IFP x position reflects the particles momentum, broadened mainly by the size of the source. The IFP y position is an order of magnitude enlarged image of the source y position, which, given beam line apertures, limits the source size in the y direction. The target x coordinates are approximately a slightly magnified image of the source. This limits to source size in the experiment to $\approx \pm 5$ cm from the GEM chamber sizes. Without the GEM chamber requirement, we have found the acceptance of the channel extends out in x to $\approx \pm 15$ cm, rather than ± 5 cm.

While the leading order matrix elements are important, as we will see there are only a few distributions that are dominated by these matrix elements, with a tight correlation between parameters at different points along the beam line. Most distributions in PiM1 are significantly broadened by higher order matrix elements. We present a fuller picture of the channel properties by using TURTLE calculations to plot correlations between beam parameters at different points along the beam line. The small beam spot of the default TURTLE calculation limits the ability to see some of the correlations, so we use instead a large source distribution. This also allows a study of the maximum acceptance of the PiM1

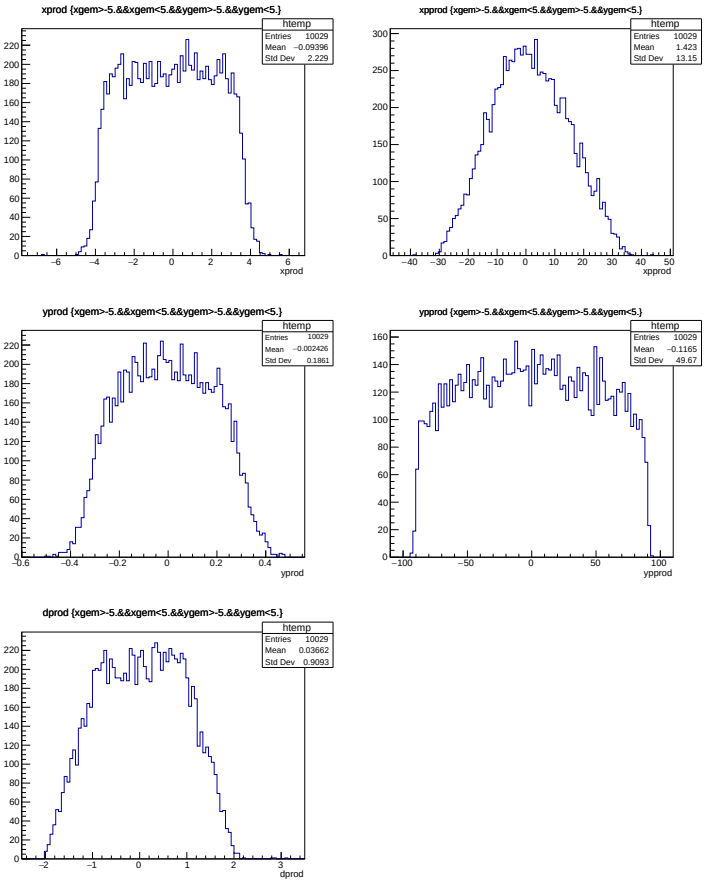

FIG. 9: Production distributions for a large source, requiring particles to be in the GEM chambers in the target region. ***Upper left***: position distribution in x. ***Upper right***: x', the angular distribution in x. ***Center left***: position distribution in y. ***Center right***: y', the angular distribution in y. ***Lower left***: momentum distribution δ in % from nominal momemtum.

channel for source simulations. Since the matrix elements are determined experimentally by tracks in the GEM chambers, and we will compare with experiment in Section III B 5, we require particle trajectories that appear in these plots to pass through a 10 cm $\times$ 10 cm region at the position of the GEMs. The needed source size expands from $\pm$0.1 cm in x, $\pm$0.1 cm in y, $\pm$20 mr in x', $\pm$90 mr in y', and $\pm$1.5% in δ to slightly more than $\pm$5 cm in x, $\pm$0.5 cm in y, $\pm$35 mr in x', $\pm$95 mr in y', and $\pm$2% in δ. The source distributions of particles that reach the GEM chambers in the PiM1 target region are shown in Fig. 9. *We emphasize that these source distributions are intended to show the channel acceptance*

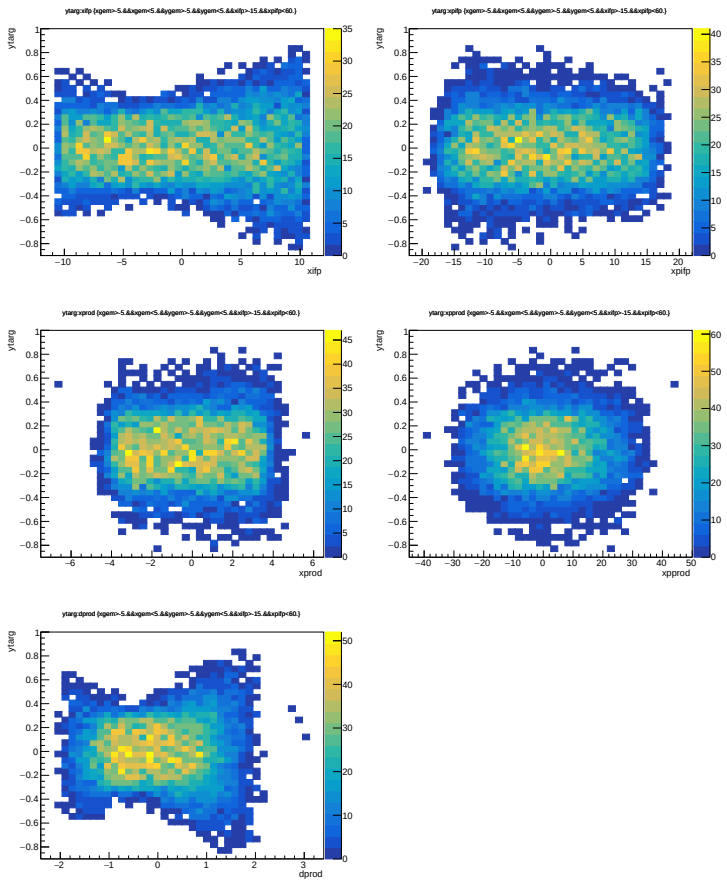

FIG. 10: Dependence of y_{targ} on x and x' at the IFP and source, and on δ. ***Upper left***: y at the target vs x at the IFP. ***Upper right***: y at the target vs x' at the IFP. ***Center left***: y at the target vs x at the source. ***Center right***: y ay the target vs x' at the source. ***Lower left***: y at the target vs momentum distribution δ in % from nominal momemtum at source.

(for particles that might reach the GEMs) and matrix elements, and do **not** *correspond to the physical distributions of any particle type into PiM1.*

Table I and Figs. 7 and 8 showed that the $x + \delta$ coordinates largely decouple from the y coordinate. One does see for example that the ranges in x change with y, but the central values of x or δ do not. We show this decoupling of the x and y directions again for a subset of matrix elements in Fig. 10. The top row shows that the central values of y_{targ} are 0, independent of $x_{\rm IFP}$ and x'_{IFP}. The middle row shows that the central values of y_{targ} are 0, independent of x_{prod} and x'_{prod}, the source distributions. The bottom row shows that the central values of y_{targ} are 0, independent of δ. The momentum δ is of

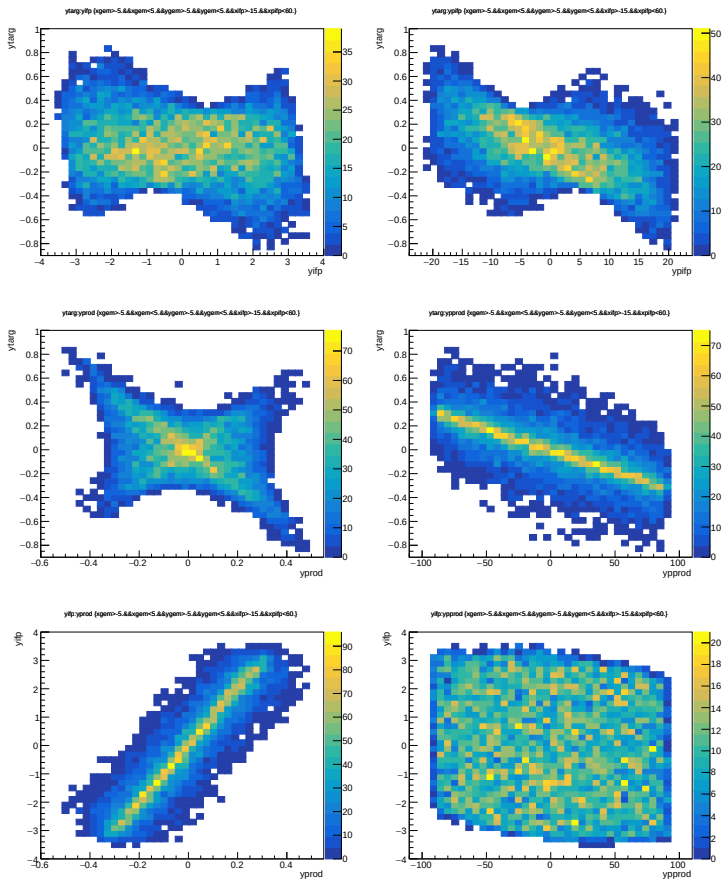

FIG. 11: Dependence of y_{targ} and y_{IFP} on y and y' at upstream locations in the beamline. ***Upper left***: y_{targ} vs y_{IFP}. ***Upper right***: y_{targ} vs y'_{IFP}. ***Center left***: y_{targ} vs y_{prod}. ***Center right***: y_{targ} vs y'_{prod}. ***Lower left***: y_{IFP} vs y_{prod}. ***Lower right***: y_{IFP} vs y'_{prod}.

course the same at all points, neglecting scattering from apertures. Due to these results, we now assume for the remainder of this section that the two orthogonal directions are decoupled, and we do not consider further any matrix elements connecting the $x + \delta$ with y directions.

The beam matrix elements are studied in Figs. 11, 12, 13, and 14. The cleanest dependences for y are that $y_{targ} \approx$ -0.004y'_{prod} cm/mr, while $y_{IFP} \approx 10 y_{prod}$. The beam at the IFP is known to be only a few cm high, which limits the source region to a height of a few mm, consistent with the large source size calculation shown in Fig. 9.

We know from Fig. 7 that there is a y' vs. y correlation at the IFP. Figure 12 shows that y_{prod} and y'_{targ} are both closely correlated with y_{IFP} and y'_{IFP}. In particular, since

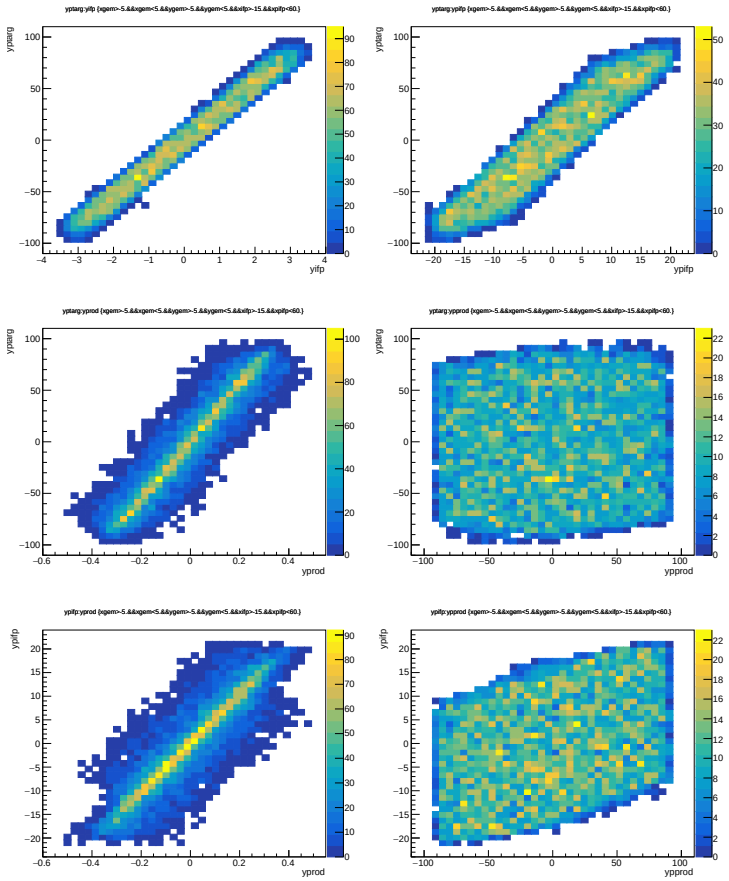

FIG. 12: Dependence of y'_{targ} and y'_{IFP} on y and y' at upstream locations in the beamline. ***Upper left***: y'_{targ} vs y_{IFP}. ***Upper right***: y'_{targ} y'_{IFP}. ***Center left***: y'_{targ} vs y_{prod}. ***Center right***: y'_{targ} vs y'_{prod}. ***Lower left***: y'_{IFP} vs y_{prod}. ***Lower right***: y'_{IFP} vs y'_{prod}.

$y'_{targ} \approx 5\ y'_{IFP}$, material causing multiple scattering at the IFP can lead to much broader y'_{targ} distributions.

Figure 13 shows the matrix elements involving x_{targ} and x_{IFP}. The optics of the channel produce an image of the source distribution at the target with magnification close to unity in position, though not in angle.

Figure 14 shows matrix elements involving x'_{targ} and x'_{IFP}. The broad correlated distributions shown make it clear that higher order matrix elements are important to understanding the optics of these distributions.

Figure 15 shows matrix elements involving δ. Most notable is the dispersion at the IFP, which remains 7 cm / %, but now for any point in x_{IFP} the distribution is about 1% full

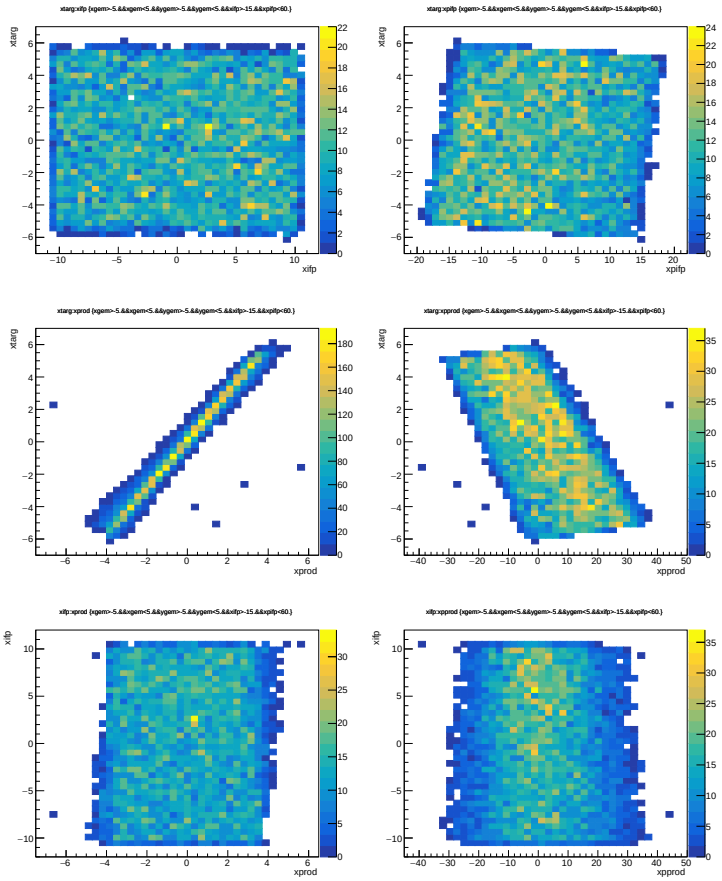

FIG. 13: Dependence of x_{targ} and $x_{\rm IFP}$ on x and x' at upstream locations in the beamline. ***Upper left***: x_{targ} vs x_{IFP}. ***Upper right***: x_{targ} vs x'_{IFP}. ***Center left***: x_{targ} vs x_{prod}. ***Center right***: x_{targ} vs x'_{prod}. ***Lower left***: x_{IFP} vs x_{prod}. ***Lower right***: x_{IFP} vs x'_{prod}.

width, or about 0.3% rms. This calculation provides an upper limit on how much worse the channel momentum resolution can be for particles which have an extended source, as it assumes a flat production distribution. Note that an extended source that is symmetric in the $\pm x$ directions will have worse resolution but no momentum offset compared to a point-like source. For a broad collimator opening at the IFP, with a 1 or 2% momentum bite, the effect will be relatively small. However, an asymmetric source in the $\pm x$ directions will have both worse resolution and an offset in the central momentum, that depends on the asymmetry of the source.

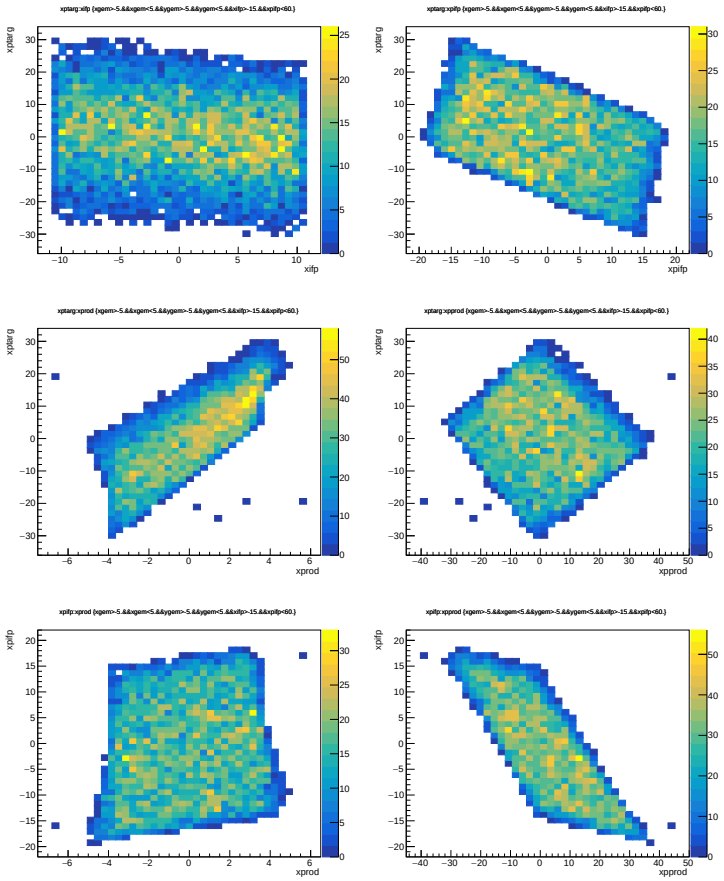

FIG. 14: Dependence of x'_{targ} and x'_{IFP} on x and x' at upstream locations in the beamline. ***Upper left***: x'_{targ} vs x_{IFP}. ***Upper right***: x'_{targ} vs x'_{IFP}. ***Center left***: x'_{targ} vs x_{prod}. ***Center right***: x'_{targ} vs x'_{prod}. ***Lower left***: x'_{IFP} vs x_{prod}. ***Lower right***: x'_{IFP} vs x'_{prod}.

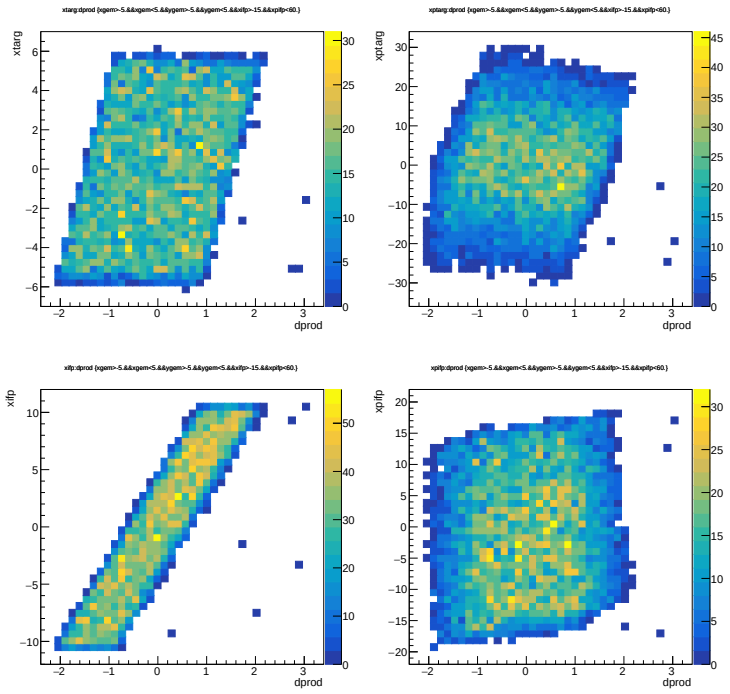

FIG. 15: Dependence of x and x' at the target and IFP on δ. ***Upper left***: x_{targ} vs δ_{prod}. ***Upper right***: x'_{targ} vs δ_{prod}. ***Lower left***: x_{IFP} vs δ_{prod}. ***Lower right***: x'_{IFP} vs δ_{prod}.

B. Model sources

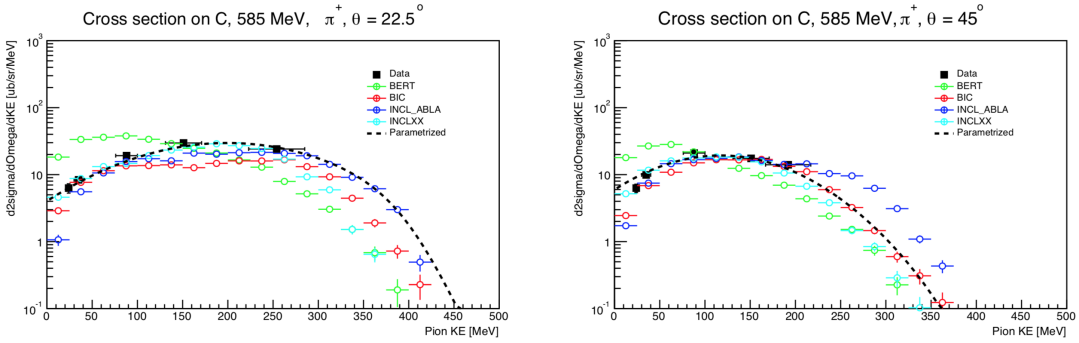

FIG. 16: Positive pion production from $p + C$ at 22.5° and 45°, as a function of pion kinetic energy.

Our initial modeling of the source distributions was based on 4 ingredients:

1. Modeling of pion production by A. Knecht of PSI and collaborators [2, 3].
2. PiM1 channel acceptance, calculated with TURTLE.
3. Geometry in the M production target region.
4. Use of Geant4 and root (for muon production) to simulate how pions produced in the M target generate muons and electrons/positrons within the PiM1 channel acceptance.

Modelling pion production: Figure 16 shows the example of positive pion production modelling done by A. Knecht of PSI and collaborators. The basic result is that the pion production cross sections are roughly flat, independent of energy, at each angle, until one gets to the highest and lowest allowed pion energies. Furthermore, the magnitude of the flat plateau cross section is approximately independent of angle, for angles from 22.5° $\rightarrow$ 135°. The same holds true for π^- production, except that the magnitude of the plateau cross sections is a factor of 4 - 5 smaller. We *assume* that this observation continues to hold true at angles down to 0°. Since the central angle of the PiM1 channel is at about 22.5°, it then becomes clear from the kinematics of $\pi \rightarrow \mu\overline{\nu_\mu}$ decay the calculations shown in Fig. 16 cover the range of pion production energies and angles of interest for decaying into muons

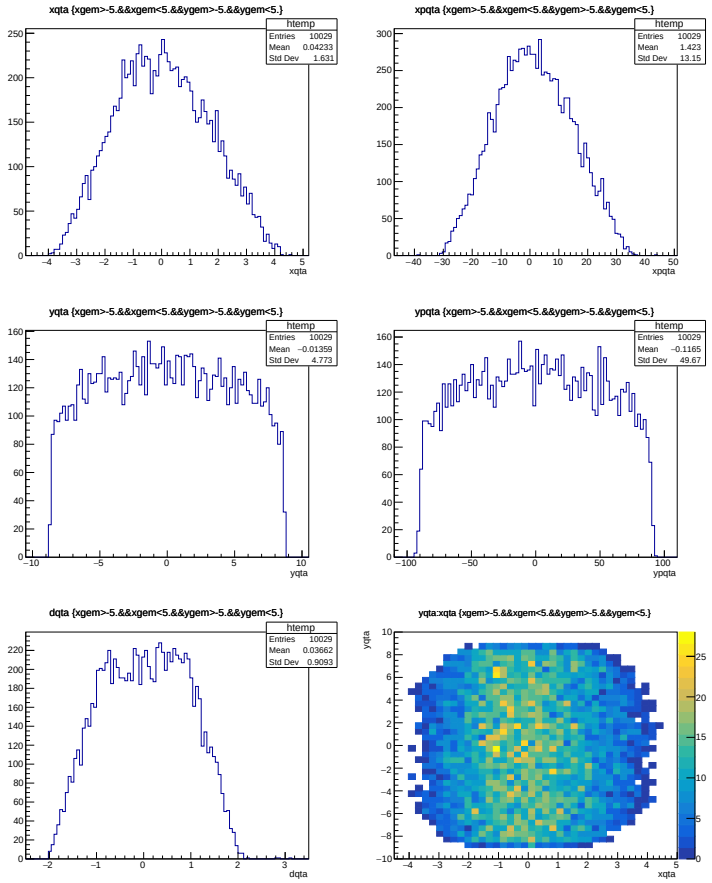

FIG. 17: Distributions of particles at the QTA1 entrance that reach the GEM chambers after the PiM1 channel. ***Upper left***: position distribution in x. ***Upper right***: x', the angular distribution in x. ***Center left***: position distribution in y. ***Center right***: y', the angular distribution in y. ***Lower left***: momentum distribution δ in % from nominal momemtum. ***Lower right***: position distribution y vs x.

that are in the PiM1 channel acceptance – we will show consistency in the simulations below. Thus, it is an adequate assumption for the purpose of source modelling to take the parent pion distributions, that lead to muons in PiM1, to be independent of pion kinetic energy and angle. When we move to modelling of e^+ and e^- source distributions, *we will assume that the cross sections for parent* π^0 *production are also independent of pion kinetic energy and angle.*

Channel acceptance: The PiM1 distributions with a large source were already shown, but for the purpose of source modeling the important question is the acceptance of the first

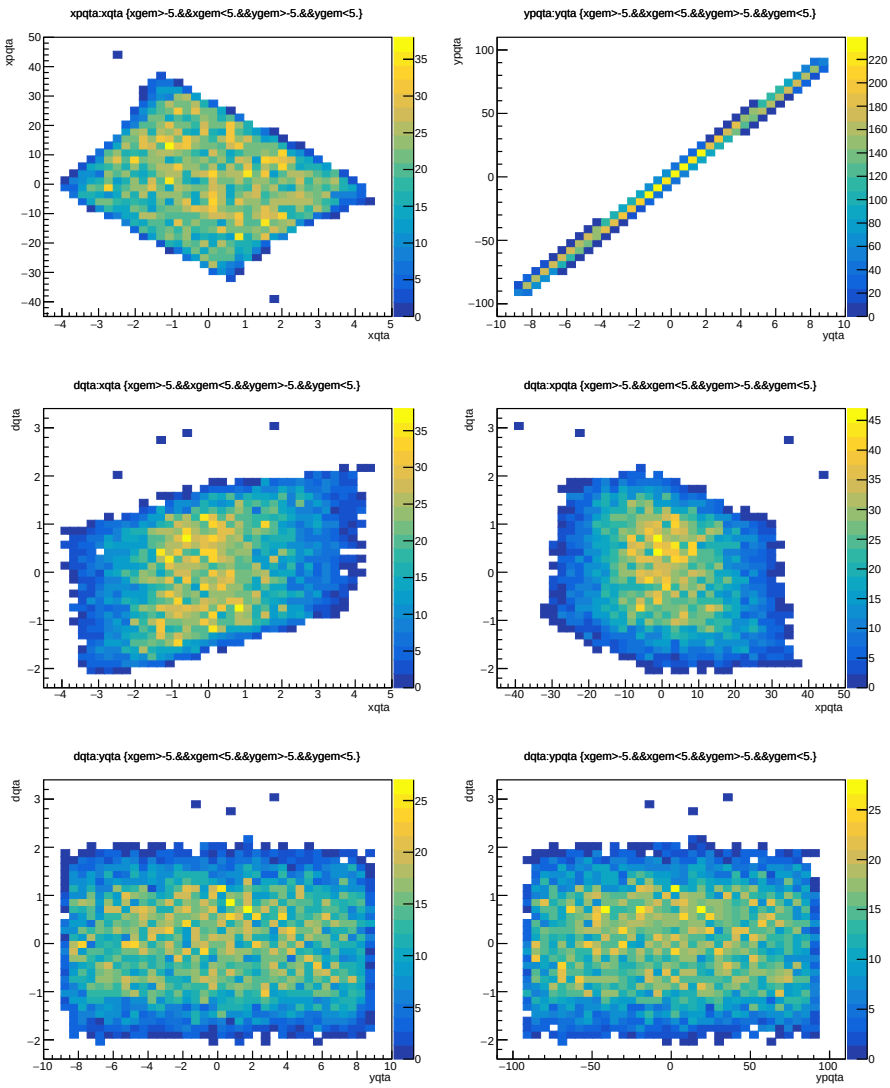

FIG. 18: Correlations of particles at the QTA1 entrance that reach the GEM chambers after the PiM1 channel. ***Upper left***: x' vs x. ***Upper right***: y' vs y. ***Center left***: δ vs x. ***Center right***: δ vs x'. ***Lower left***: δ vs y. ***Lower right***: δ vs y'.

magnetic element, QTA1. Figure 17 shows the distributions of particles that successfully transport though the PiM1 channel into the GEM chambers, at the front face of QTA1. The $\pm$4-cm wide x distribution is narrower than the $\pm$9-cm wide y distribution, reflecting the fact that the initial beam line quadrupoles focus in the y direction and defocus in the x distribution. The wider x distributions also allow the momentum range that passes through the channel to expand from $\pm$1.5% to $\pm$2%.

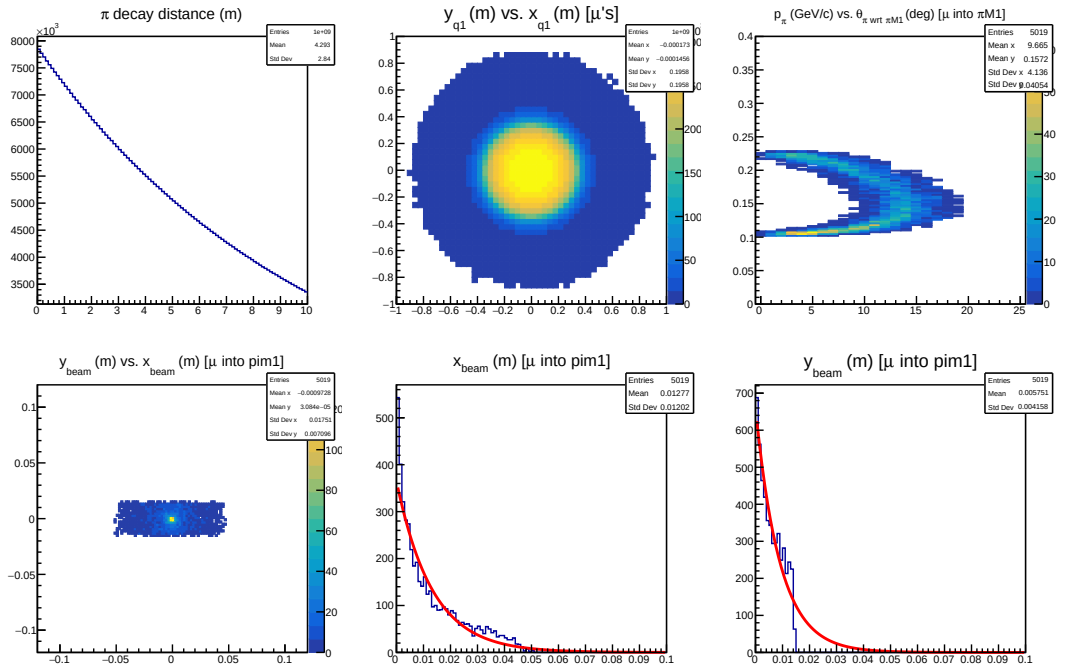

FIG. 19: Output of root simulation of the muon source size, for 120 MeV/c channel setting. Note that variable labels and units differ from the TURTLE standard. ***Upper left***: Decay distance for pions in m. ***Upper middle***: y (m) vs x (m) for muons at the entrance to the first quad. ***Upper right***: Momentum in GeV/c vs angle in degrees of pions that generate muons that pass the first quad aperture cuts. ***Lower left***: y (m) vs x (m) at the source plane of muon tracks that pass the first quad aperture cuts. ***Lower middle***: Distribution of x (m) at the source plane for muon tracks that pass the first quad aperture cuts. Also shown is an exponential fit to the distribution. ***Lower right***: Distribution of y (m) at the source plane for muon tracks that pass the first quad aperture cuts. Also shown is an exponential fit to the distribution.

Figure 18 shows how the parameters of the particles that traverse the channel are correlated at the entrance to QTA1. The top right panel shows the strong, narrow correlation in y'_{QTA} vs. y_{QTA}. As mentioned earlier, we know from the simulations and matrix element y_{IFP} vs. y_{prod} that the channel has a small source size y_{prod} of about ± 6 mm. But as there are no magnetic elements between the source and QTA, and since the acceptance of QTA1 is ± 8 cm, there must be a strong $y'_{QTA} = y'_{prod}$ vs. y_{QTA} correlation for particles to reach large y_{QTA}. The limited acceptance in y_{prod} severely constrains the production of muons and electrons that make it through PiM1.

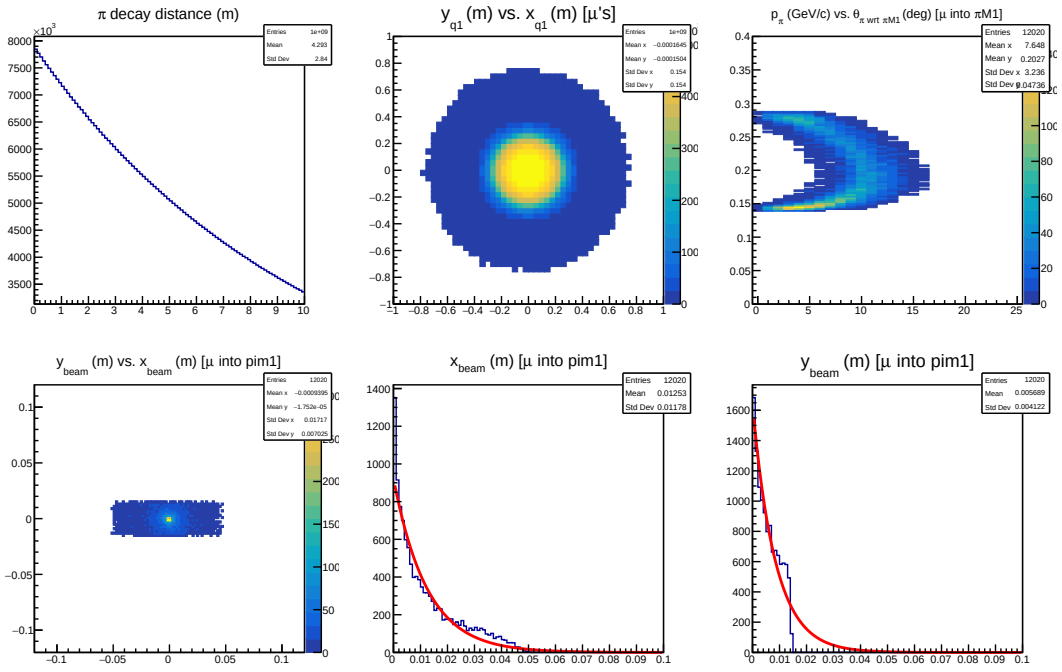

FIG. 20: Same as Fig. 19, but for 155 MeV/c channel setting.

The correlation for x'_{QTA} vs. x_{QTA} is shown in the top left panel of Fig. 18. As x_{QTA} gets more positive, for example, the angle x'_{QTA} becomes more negative – otherwise the defocusing of the quad would bend the particle into the side of the quad. The distribution is broadened by the range of momentum.

The momentum correlations shown in the middle and bottom row panels of Fig. 18. We see a tilt of the distribution of δ vs. x_{QTA}, and perhaps some correlation of δ with x'_{QTA}. There is again no significant correlation of the momentum with y_{QTA} or y'_{QTA}.

The calculations shown were used to generate cuts for the muon and electron source simulations. They define limits on the maximum and minimum x_{QTA}, x'_{QTA}, y_{QTA}, y'_{QTA}, and δ_{QTA}, plus correlation cuts. The correlation of y'_{QTA} in mr vs. y_{QTA} in cm was implemented with $10.55y_{QTA}$+15 $> y'_{QTA} >$ $10.55y_{QTA}$-15. The correlation of x'_{QTA} in mr vs. x_{QTA} in cm is a diamond shaped region, implemented with a combination of 4 cuts, $13.5x_{QTA} + 58 > x'_{QTA}$, $-7.0x_{QTA} + 32 > x'_{QTA}$, $-6.5x_{QTA} - 30 < x'_{QTA}$, and $7.0x_{QTA} - 36 < x'_{QTA}$. The correlation of momentum in % with position x_{QTA} in cm used

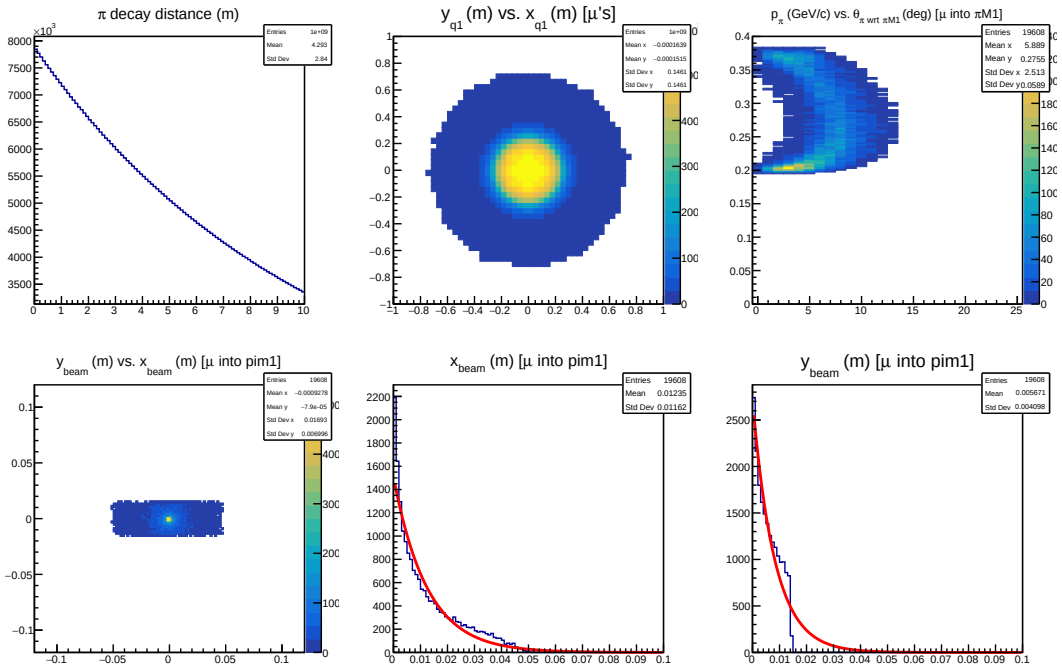

FIG. 21: Same as Fig. 19, but for 210 MeV/c channel setting.

cuts $22.5x_{QTA}+1.9 > \delta_{QTA} > 22.5x_{QTA}-1.8$. No cut was put in for a correlation of δ_{QTA} vs. x'_{QTA}.

Geometry in the M target region: The geometry of the graphite disk of the M target was shown in Fig. 2. The beam passes at an angle through a 2-mm wide flange of the graphite disk. Particles generated in the beam spot that go directly into the PiM1 channel pass through about 2 cm of graphite. The distance from the center of the beam spot to the front face of the first quad, QTA1, is 95.8 cm, as documented in the TURTLE input deck presented in Appendix C.

Muon simulations with root and Geant4: The above information coupled with the physics built into Geant4 now allow the source distributions of muons and electrons (and positrons) to be evaluated. For the case of muons, we have run the simulations with root and verified the results in Geant4, including showing that interactions of the pions and muons in the graphite disk have little impact on the muon source distributions.

Figures 19, 20 and 21 show the outputs of the root simulations. The top left panels show the exponential decay of the pions with distance traveled. The top center panels show the

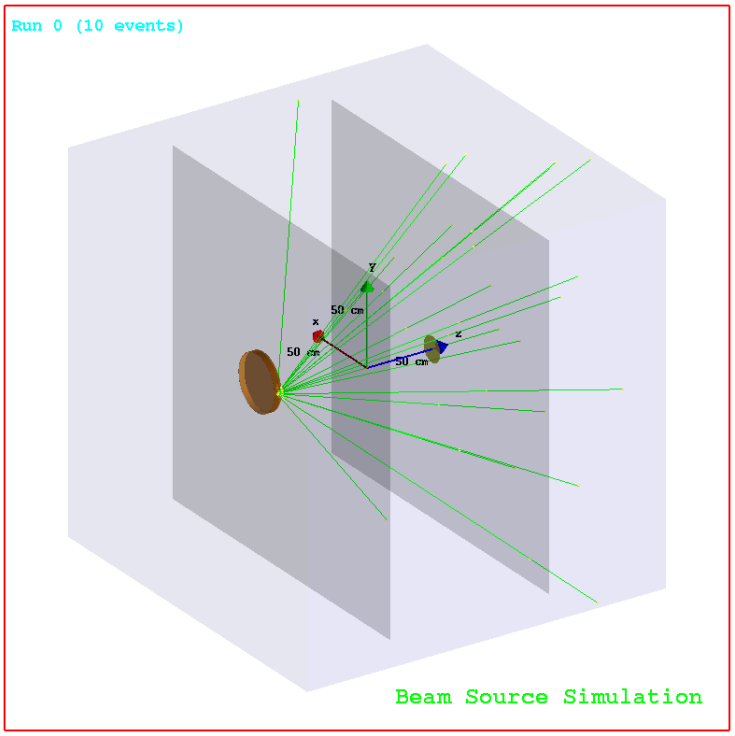

FIG. 22: Geometry of the M target region used in the Geat4 simulations. Note that the Geant4 simulation uses $x = -x_{transport}$ and $y = -y_{transport}$.

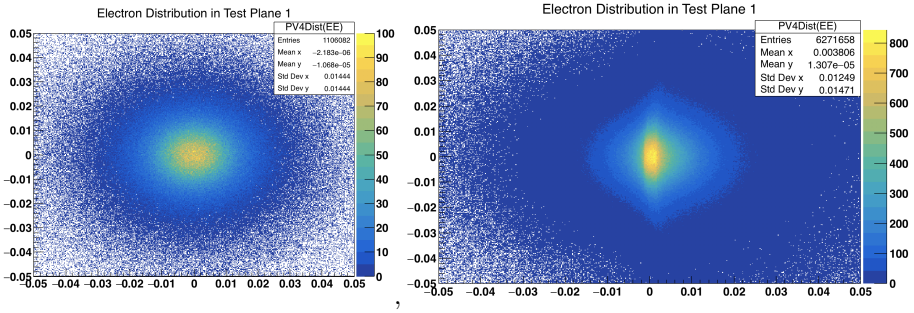

FIG. 23: Electron/positron distributions on the test plane immediately after the position of the M target graphite disk. Units are m. (Left) The distribution when the simulation throws π^0's from the source, but without the graphite disk, so that only Dalitz decays are shown. (Right) The full simulated distribution including both γ conversion in the graphite disk and Dalitz decays.

distributions of muons on the transverse plane at the start of QTA1. The acceptance of QTA1 quoted above of ± 4 cm in x by ± 9 cm in y is much smaller than the simulated muon distribution at the entrance to QTA1. These plots are not identical for all beam momenta

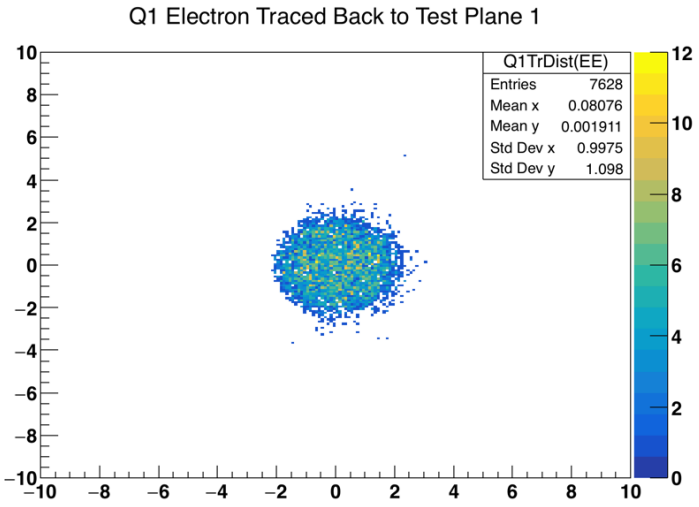

FIG. 24: Electron/positron source distributions for electrons satisfying QTA1 cuts and correlations. Units are mm.

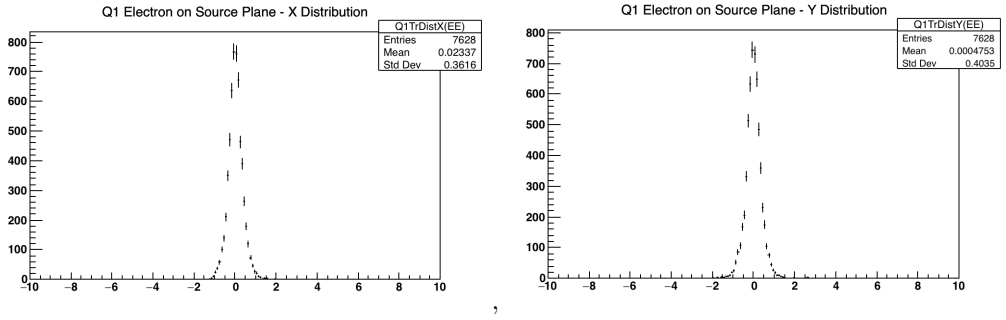

,

FIG. 25: Electron/positron source distributions for electrons satisfying QTA1 cuts and correlations. Units are mm.

since we tailor the distribution of thrown pions somewhat for each momentum to have a more efficient simulation. The top right panels show the distributions of pion momenta vs. angle for pions that generate muons that pass the QTA1 aperture and correlation cuts. The simulated input used 10^9 pions uniformly distributed in kinetic energy and solid angle, for momenta from 0.1 - 0.4 GeV/c and angles up to 21°. The efficiency for producing muons into PiM1 is then $\approx 10^{-5}$. The top right panels also show that the input ranges are sufficient. Kinematic focusing leads to a high density of muons from forward decaying pions, leading to slightly higher momentum muons, seen for angles of a

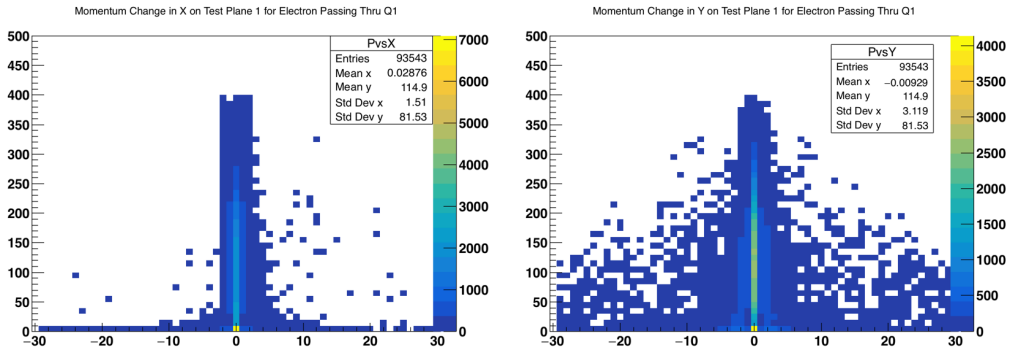

FIG. 26: ***Left***: Electron momentum in MeV/c as a function of x in mm on the test plane for y = 0. ***Right***: Electron momentum in MeV/c as a function of y in mm on the test plane for $x = 0$.

few degrees and momenta near the miminum for each momentum setting. This feature however includes only a few percent of the full muon distribution.

The effective source distributions are shown in the bottom row panels of Figs. 19, 20 and 21. The bottom left panels show the distribution of muon trajectories in y vs. x, for muons that pass the QTA1 aperture and correlation cuts, projected back to the source plane. The full widths of the distributions are about ±5 cm in x and ±1.5 cm in y. Figure 9 showed that for a large source the production region is limited to about ±5 cm in x and ±0.5 cm in y, so the source distributions we are generating will be correctly sized in x, but overly large in y. The bottom middle (right) panels show the distance of the trajectory on the source plane from x (y) = 0, along with exponential fits. The fits have characteristic lengths of 1.32, 1.24, and 1.25 cm for central channel momenta of 120, 155, and 210 MeV/c, respectively, in the x direction, and 0.91, 0.85, and 0.82 cm in the y direction. The statistical uncertainties are a few percent. In Geant4, the graphite disk modifies the exponential slightly, and the extracted exponential fits have characteristic lengths of 1.24, 1.22, and 1.23 cm in the x disrection and 1.04, 0.80, and 0.84 cm in the y direction. The Geant4 lengths are similar to the lengths in root. In the x direction, we see that the simulation produces extra events – at the level of a few percent of the distributions – at both small and large x, around 0 and 3 - 4 cm, and a deficit of events at intermediate x, around 1 cm, compared to the fit. For simplicity in TURTLE simulations

presented below, we will take the length parameters in the x and y distributions to be 1.28 (0.87) cm in the x (y) direction for all beam momenta.

Electron/positron simulations with Geant4: Figure 22 shows the geometry used in the Geant4 source simulations. Note that the simulation coordinate system has $z = z_{transport}$, but $x = -x_{transport}$ and $y = -y_{transport}$. The graphite disk uses a simplified geometry from that shown in Fig. 2, with the 2-mm wide flange perpendicular to the plane of the disk, and the pions originating at constant $z = 0$. We look at particle distributions in 3 test planes, at $z = 0$, the source, at $z = 2.55$ cm, immediately after the graphite disk, and at $z = 94.8$ cm, the entrance plane of QTA1. We test at the entrance plane that the electrons / positrons satisfy the PiM1 channel and acceptance cuts, and generate source distributions for those that do.

Geant4 takes into account electron / positron production through both the ≈98.8% branching ratio $\pi^0 \to \gamma\gamma$ decay, followed by γ conversion in the graphite, and the ≈1.2% branching ratio $\gamma C \to e^+e^-X$ Dalitz decay production. Without the carbon plate, there is not γ conversion, so only the Dalitz decay production contributes. We verified that this leads to an effective source size of order nm, due to the short π^0 lifetime.

Figure 23 shows the electron distributions at the test plane at $z = 2.55$ cm without and with the carbon disk to convert π^0 decays photons into electron-positron pairs. Without the carbon disk, electrons / positrons are only generated by Dalitz decays. These distributions include all generated particles; only the central few mm of particles at this z position will satisfy the QTA1 cuts for the no-carbon-plate case. The right panel shows a small enhancement from the graphite flange, the slightly enhanced arc bending to $+x$ as y moves away from 0. We also see a preference for events on the $+x$ side, the side with the M target. The simulations for both panels of the figure were run for the same number of source π^0's, so the cross section and geometry for photon conversion reduces the dominance of the conversion process over direct production from the branching ratio factor of ≈98.8/1.2 = 82 to a factor of (6.27e6-1.11e6)/1.11e6 = 4.6. Since the mean free path for few hundred MeV/c photons in graphite is several cm, only a fraction of them should be expected to convert in the graphite disk, and the ratio should be reduced by around an order of magnitude.

When we require that the electrons satisfy the QTA1 cuts and correlations, the distribution narrows on the test plane to the few mm sized distribution shown in Fig. 24. The x and y projections of this distribution on the source plane are shown in Fig. 25. In both directions the distributions have an rms width of about 0.4 mm. Recall that photons moving in the $\pm y$ direction pass through more than 2.55 cm of graphite, while photons moving in the $-x$ direction quickly exit the graphite and cannot convert, and photons in the $+x$ direction pass through part of the flange and the carbon disk itself. This geometry probably accounts for the slightly wider distribution in y, and the slight offset in x with no offset in y. Note that for simplicity the initial π^0's in the simulation were produced at a point, rather than through the beam spot, so the 2 mm full width of the flange should be added to this result. But since the simulation indicates that the electron source is significantly smaller than the flange width, it appears that it is sufficient to use the same source size, the flange width, for electrons and pions.

To better understand this observation of the small electron source size, we looked at momentum / angle position correlations in the generated electron distributions, with no momentum or angle cuts on QTA1. Figure 26 shows the results. As we move away from $x = y = 0$ along the y axis, the typical electron momentum drops rapidly, being somewhat higher on the $+x$ side where the graphite disk is. As we move away from $x = y = 0$ along the x axis, the typical electron momentum again drops rapidly, but symmetrically, and not as fast as is the case for moving in the x direction. Having a large electron / positron source requires that photons are generated at large angles to PiM1, traverse several mm or cm of carbon, and then convert to electrons at large angle to the photon, still with sufficient momentum to pass through the PiM1 channel. The probability for this is small. It is more probable in the $\pm y$ direction, due to the greater available amount of graphite, but the channel optics limit the source size much more in the y direction.

We conclude that the electron / positron source size appears to be small, essentially consistent with the pion source size. This leads to the conclusion that the channel properties should be essentially identical for the two different particle species, in the limit that we do not take into account decays in flight or scattering from vacuum chamber and pole face elements.

C. TURTLE simulations with realistic source sizes

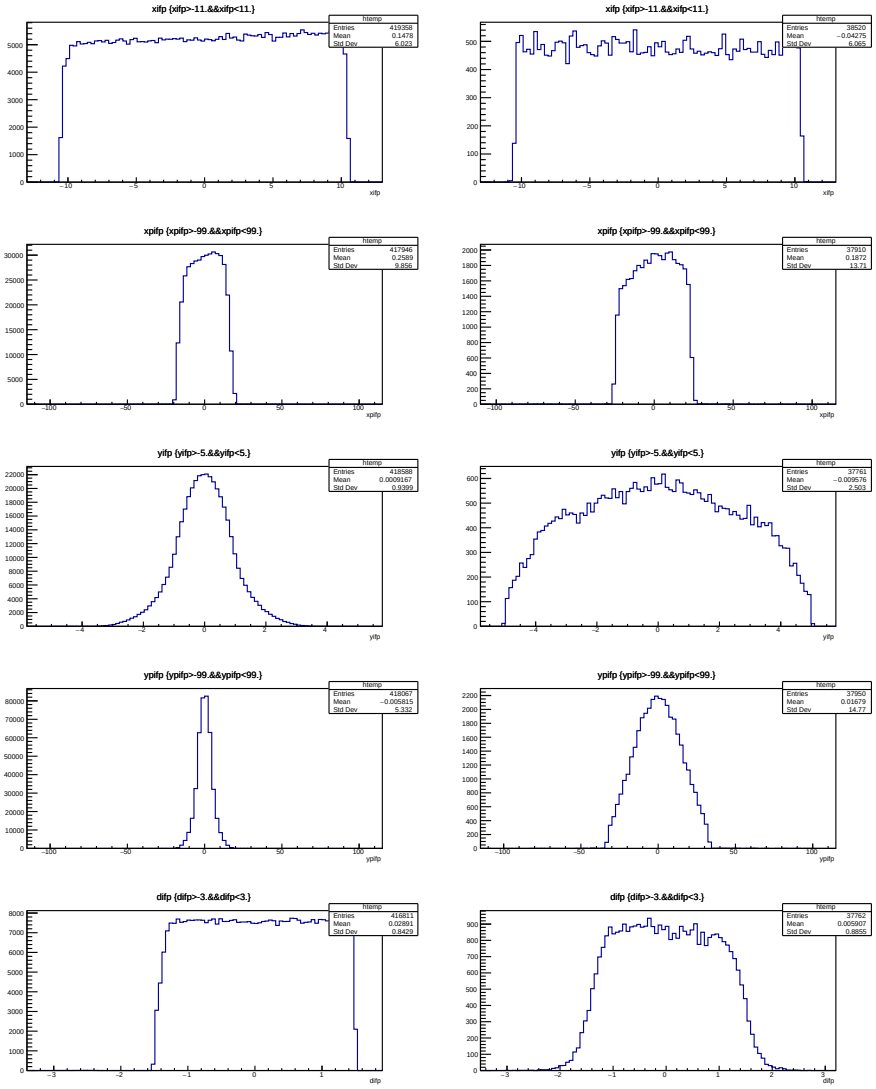

FIG. 27: Simulations of PiM1 IFP distributions, for a point source (Left) and a muon source (Right). ***Top row***: Distributions vs. x (cm). ***Second row***: Distributions vs. x' (mr). ***Center row***: Distributions vs. y (cm). ***Fourth row***: Distributions vs. y' (mr). ***Lower row***: Distributions vs. δ (%).

We can now compare the expected differences in the electron and pion beams vs the muon beam of PiM1. Figure 27 shows the resulting distributions at the IFP, for point and muon sources. The x distributions are the same; the simulation uses a 21-cm wide slit

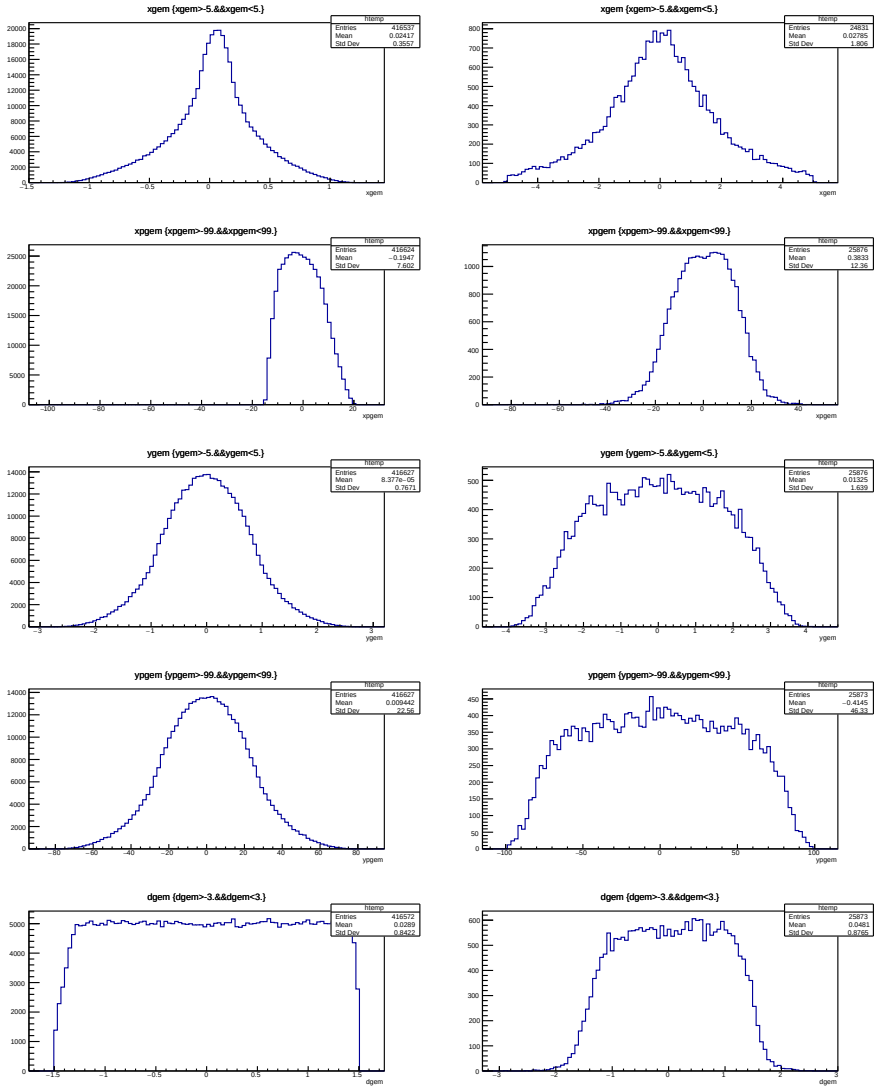

FIG. 28: Same as Fig. 27, except distributions are at the GEM chambers.

to limit the beam width in x at the IFP. The angle range in x' in increases from about ± 20 mr for the point source to ± 25 mr for the muon source. The y and y' distributions about double in size, increasing from about ± 2 cm width to nearly ± 5 cm in y and from about ± 15 mr to ± 30 mr in y'. Recall the the y_{IFP} vs y_{prod} matrix element is ≈ 10, so the increase in y reflects the full $\approx \pm 0.5$ cm acceptance in y_{prod}. The momentum acceptance expands from $\pm 1.5\%$ to about $\pm 2\%$.

Figure 28 shows the resulting distributions at the GEMs, 35 cm upstream from the target. The muon distribution is wider with larger tails in x and x'. Both distributions

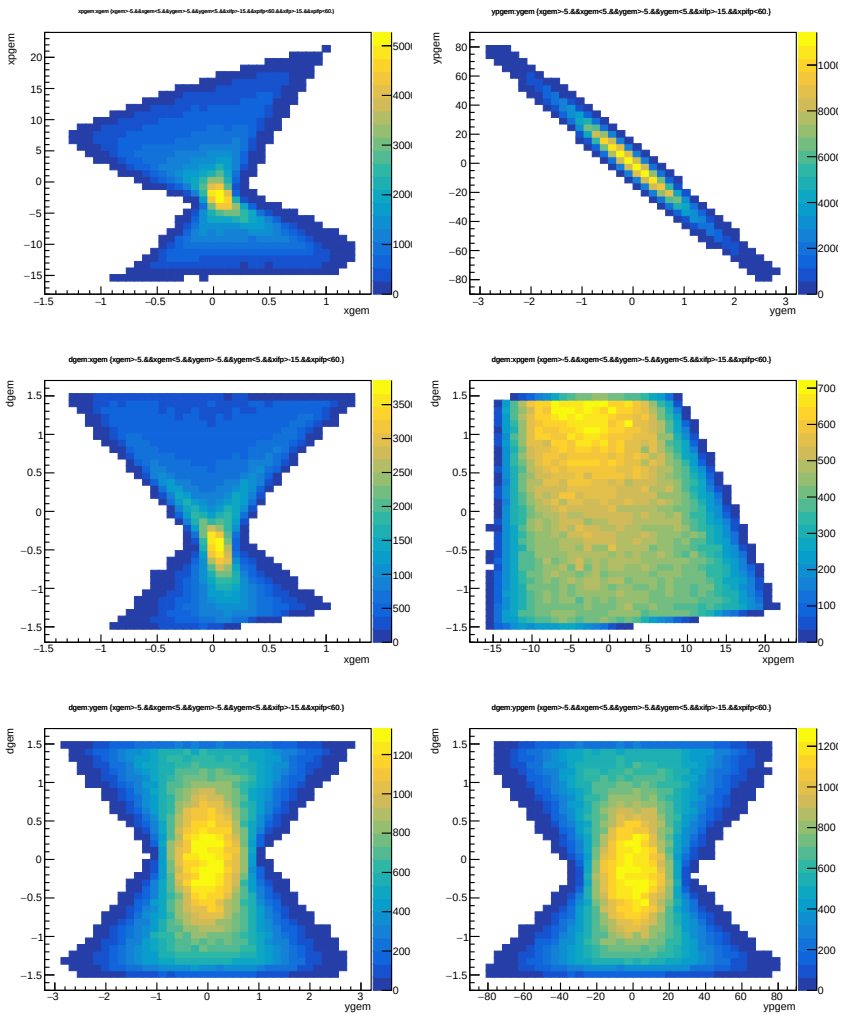

FIG. 29: Parameter correlations at the GEM chambers, 35 cm upstream of the target, for a point source. Standard TURTLE units of cm, mr, and % are used. ***Upper left***: x' vs x. ***Upper right***: y' vs y. ***Center left***: δ vs x. ***Center right***: δ vs x'. ***Lower left***: δ vs y. ***Lower right***: δ vs y'.

are approximately centered in x and x'. The y and y' distributions nearly double in size. The momentum distribution is the same as at the IFP.

The experiment measures the trajectory but not the momentum of each incoming trajectory. Fiducial cuts are placed on the trajectories to ensure the particles are aimed into the target, which we would expect to reduce the efficiency for using muons in the beam, due to their larger distributions. A more important consideration here is whether the

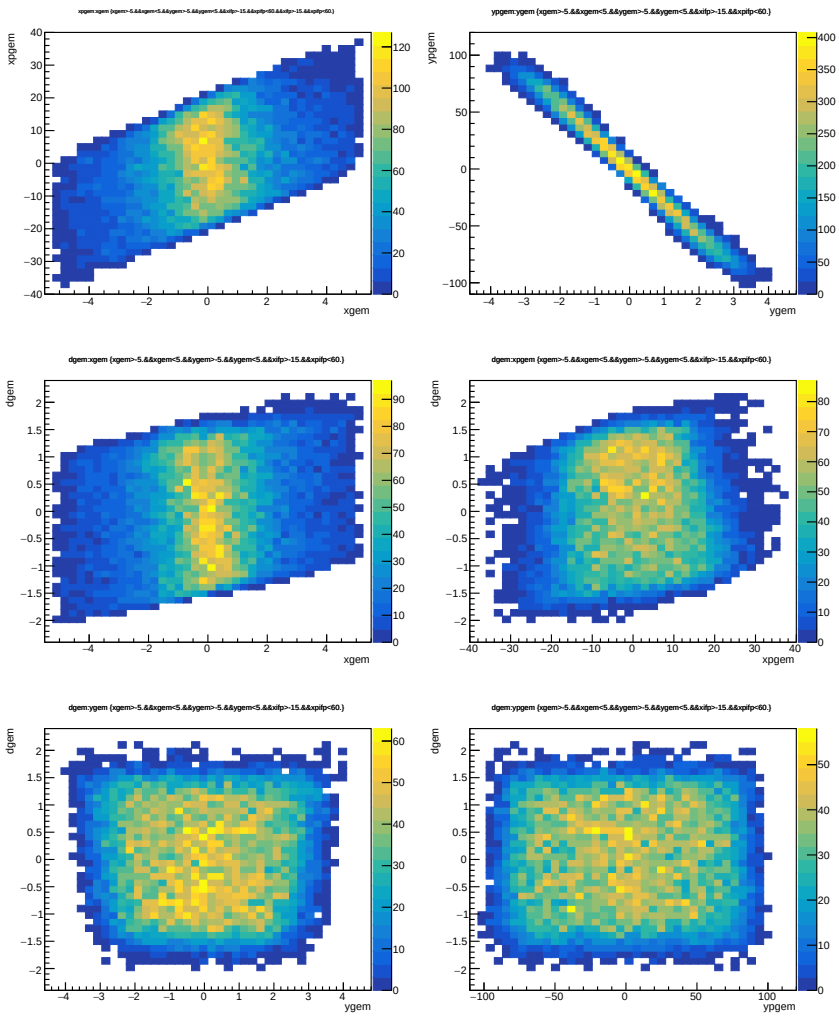

FIG. 30: Same as Fig. 29, except for a muon source.

momentum is evenly distributed through the beam spot. Note that this potential issue can be essentially resolved by employing the same tracking cuts in the GEM chambers during the TOF momentum measurements as are used in the analysis of the production data.

Figures 29 and 30 show parameter correlations at the GEM chambers for point sources and for muons. The large source size clearly modifies all of the correlations except for the the variation of y' with y, which only broadens slightly. The range of the correlations are broadened and filled in. For a point source, the central momenta are better focused into the central peak of the beam spot in x, while the ends of the momentum acceptance

contribute relatively more to the tails of the beam spot, as we observed before. However this is done in a close to symmetric way, so that the average momentum is the same. This observation does indicate that operating with a narrow collimator at the IFP to reduce the momentum acceptance and rates will tend to lead to a smaller beam spot in x. For the extended muon source, the momentum spectrum appears to almost uniform in the vertical y direction, but the momentum in the tails varies oppositely on the two sides of the beam. The additional momentum acceptance with the extended source, from $\pm 1.5\%$ to $\pm 2\%$, appears almost entirely on the edges of the beam spot, to the sides of the central peak, and the $\pm$ contributions appear on opposite sides of the beam spot. This obervation points to the need to use fiducial cuts on the beam that are symmetric about the center of the beam. Since the experimental system is left/right symmetric, and this momentum correlation is linear, it will lead to a small left vs. right detector asymmetry in cross sections that cancels in the average[1].

[1] For the 3-4% of the beam in the momentum tails, there is about a 1.5% cross section difference, so the effect appears to be below 0.1%. An effect of this size will be hard to determine precisely.

D. TURTLE simulations of using the PiM1 channel as a spectrometer.

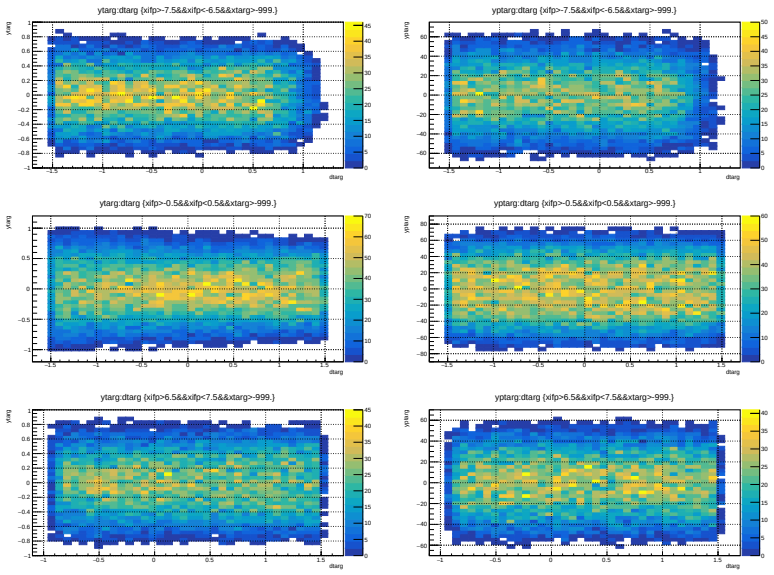

FIG. 31: ***Left column***: Dispersion in y_{targ} in cm/% for particles from 3 points at the IFP, (upper) x_{IFP} = -7 ± 0.5 cm, (center) 0 ± 0.5 cm, and (lower) 7 ± 0.5 cm. ***Right column***: Dispersion in y'_{targ} in mr/% for particles from the same 3 points at the IFP.

In this Section we are going to consider the use of the PiM1 channel as a relative momentum spectrometer, studying how, if the particles have different momentum distributions, the difference is reflected in the beam spot in the target region.

In Section II A 3 we displayed the PiM1 matrix elements, which allow us to study the beam momentum through the particle distributions at the target. Built into this determination however are the correlations at the IFP due to the description of the upstream half of the channel. In this section we adopt a more general approach of generating a random distribution of events at the IFP that lacks the correlations of Section II A 3, and transporting the particles to the target to determine how the distributions there are affected by the spread in momentum at each point in the IFP. We consider two cases: first the channel is set to the default magnet settings, and second all quadrupoles after the IFP are turned off. The "source" distributions at the IFP match the size of the point distribution beam at the IFP, with ±10.5 cm in x, ±20 mr in x', ±2.5 cm in y, ±15 mr in y', and ±1.5% in δ, but lacking correlations between parameters.

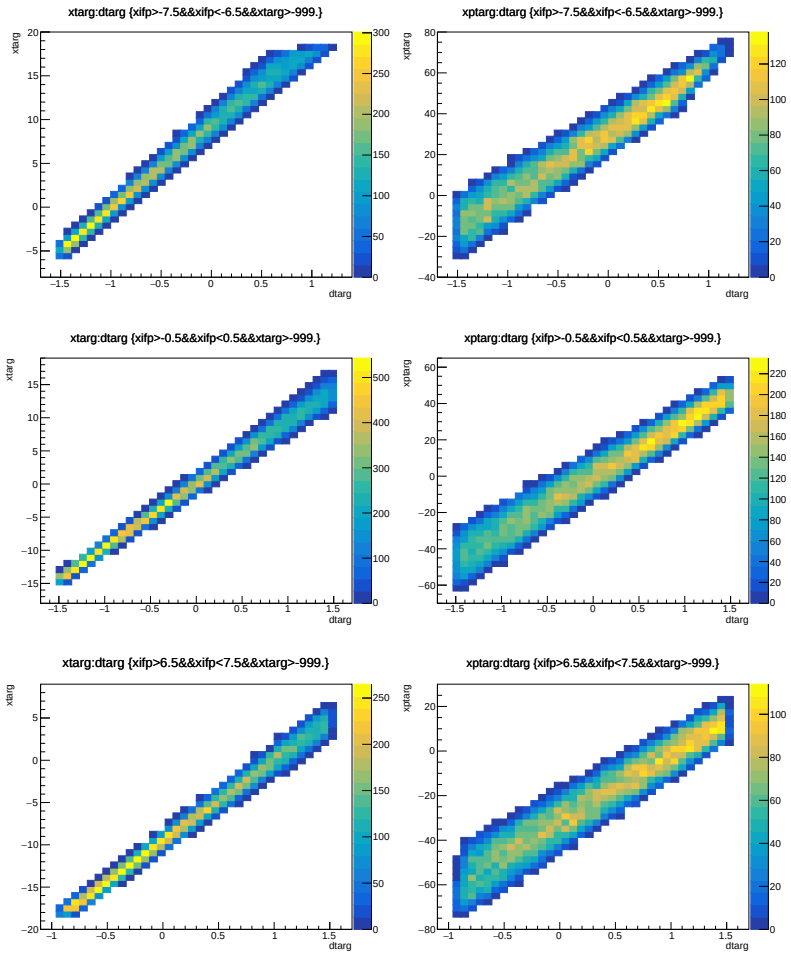

FIG. 32: ***Left column***: Dispersion in x_{targ} in cm/% for particles from 3 points at the IFP, (upper) x_{IFP} = -7 ± 0.5 cm, (center) 0 ± 0.5 cm, and (lower) 7 ± 0.5 cm. ***Right column***: Dispersion in x'_{targ} in mr/% for particles from the same 3 points at the IFP.

We show in Fig. 31 that the y and y' distributions arising from these simulations are uncorrelated with δ in the case that the quadrupoles are turned on. This is consistent with calculations we have shown before, and for brevity we omit other plots showing no correlation of y or y' with δ.

Figure 32 shows the resulting dispersion of x and x' in the first case, with quads on. The dispersion at the IFP is 7 cm / %, and in the left column we see that for x_{IFP} = -7 cm, $x_{targ} = 0$ for δ = -1%, for $x_{IFP} = 0$ cm, $x_{targ} = 0$ for $\delta = 0\%$, and for x_{IFP} = 7 cm, $x_{targ} = 0$ for $\delta = +1\%$, as expected. For each of the 3 choices of x_{IFP}, we see

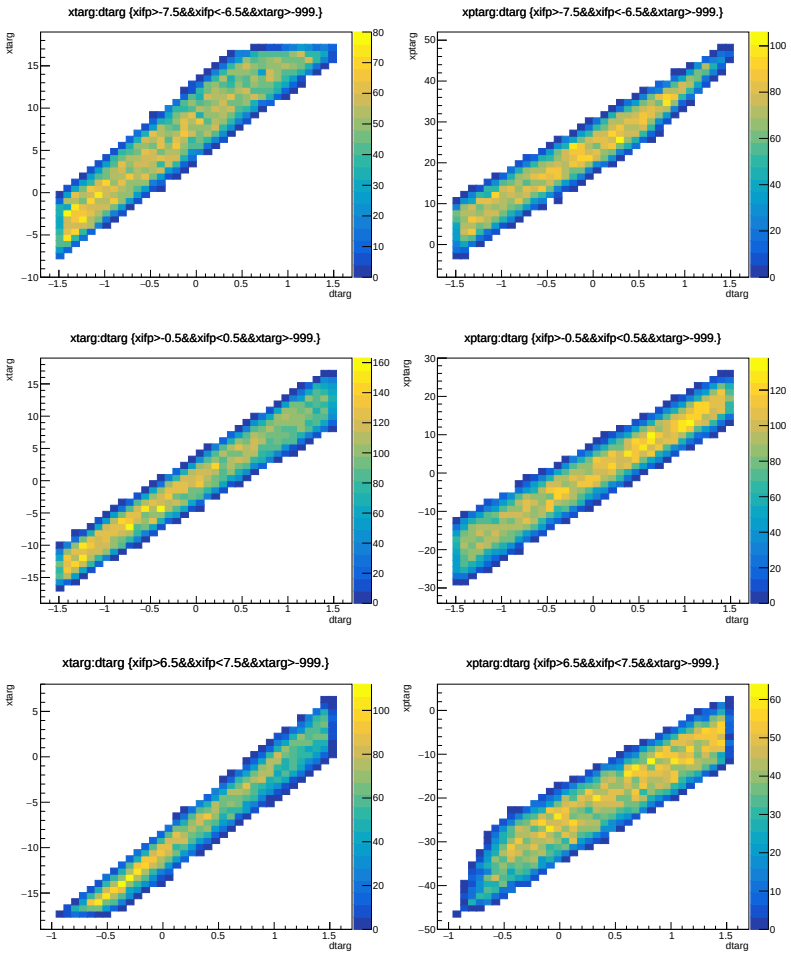

FIG. 33: Same as Fig. 32, but with all quads after the IFP turned off.

that the dispersion at the target is similar, ≈ 9 cm/%. Thus, if we select a narrow region at the IFP experimentally, the position and width in x of the beam spot is a measure of the central momentum and width in momentum at the IFP. If different particles have different average momenta, there is the 9 cm/% dispersion. For a beam arising from a point source, the 1-cm wide region at the IFP corresponds to a 0.14% momentum range, and generates an x_{targ} range of a few cm – more precisely about 1 cm FWHM according to the default TURTLE simulation shown in Fig. 6. The first-order matrix elements presented ($\langle x_{IFP}/x_{prod}\rangle = -1.225$) along with the ≈1.3 cm muon source size and a dispersion of 7 cm/% suggest that for muons a 1-cm wide slit at the IFP has a momentum range of at least 1.3 × 1.225 / 7 cm/% ≈ 0.23%, which being about twice as large as for a point

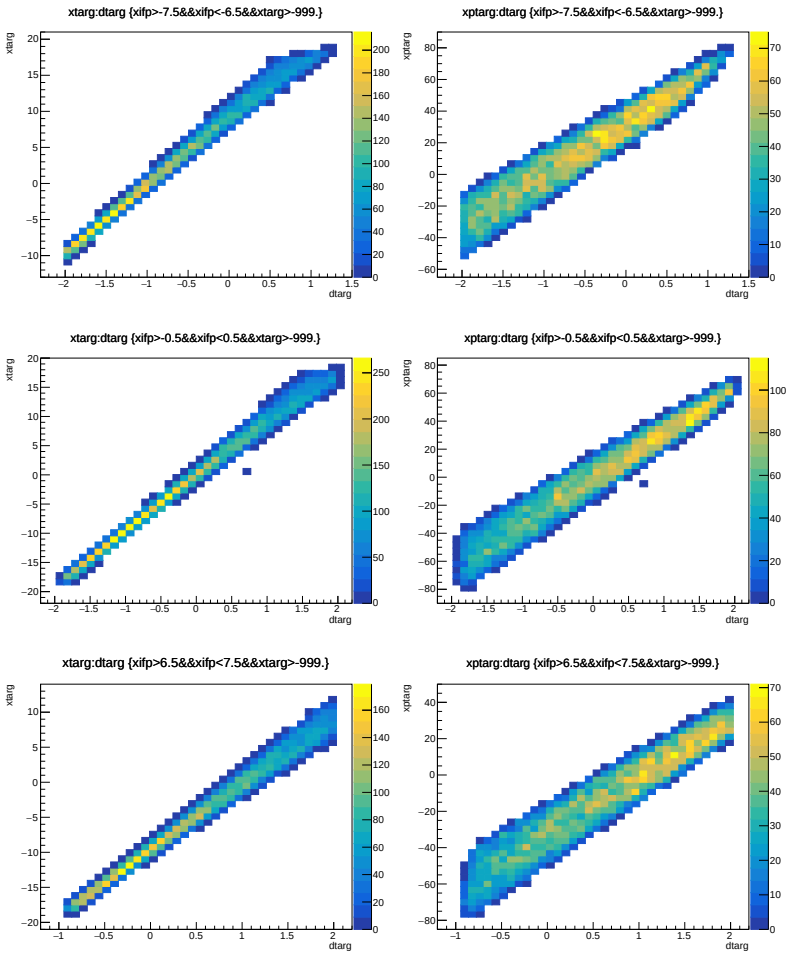

FIG. 34: Same as Fig. 32, but starting from a larger source distributions at the IFP, reflecting the larger range of angles and positions at the IFP generated by a muon source at the M target.

source, and which should make the beam spot about twice as large. The right column of Fig. 32 shows similar effects for the angle x', with a dispersion in angle of $\approx$ 25 mr / %, but The range of δ covered is larger for a fixed x' than for a fixed x, so x is a more sensitive quantity.

Since the quadrupoles focus and potentially steer particles, we also considered whether turning all quadrupoles off and leaving only the dipole field on would be useful. Figure 33 shows the resulting dispersion in this second case, with quads off. The distributions are quite similar to those of Fig. 32. The correlations of x_{targ} with δ have increased from a few cm width to several cm wide, while the correlations of x'_{targ} with δ have decreased

from about 25 mr to 15 mr width. The dispersion in x decreases from $\approx$ 9 cm/% to 7 or 8 cm/%, while the dispersion in angle decreases from $\approx$ 25 mr / % to about half as much. That the distributions in these two cases are not much different, and that the distributions do not spread much in x even with the quads off, over the $\approx$10.6 m flight path from the IFP to the GEMs, indicates that there is significant focusing of the distributions from the curvature at the entrance and exit of the ASAM12 dipole pole faces. The quads off measurement thus is a simpler but less sensitive measurement of the relative beam momentum distributions of the different particles.

As a check of whether our conclusions are affected by too small a source distribution, the calculations were redone using the larger source size of the muon distribution beam at the IFP. The large source used $\pm$10.5 cm in x, $\pm$27 mr in x', $\pm$5 cm in y, $\pm$35 mr in y', and $\pm$2% in δ, and again lacked correlations between parameters. Figure 32 shows the resulting dispersions at the target for the case with quadrupoles on. Comparing these results to Fig. 32, the range of the correlations is larger – there is more momentum acceptance leading to a broader beam spot – but the slope and width of the correlation is largely unchanged. Thus our conclusions above remain valid.

To summarize, when taking measurements with a narrow collimator opening, the width of the beam spot in x and x' reflects the range of momentum of the particles within the collimator opening. Particles with a broader momentum range, for the same point at the IFP, will have a broader beam spot at the target. If different particles have different average momenta, the centers of their distributions will be shifted. The dispersion is about 9 cm/% in x and 25 mr / % in x' with the quads on, and somewhat less with the quads off. A 0.1% relative average momentum measurement requires determining the relative centers of the distributions to 9 mm or 2.5 mr, which should be relatively easy to do for the GEM chambers. Some care must be taking ensuring uniformity of detector response and triggering.

E. G4beamline vs TURTLE comparison

The G4beamline [4] simulation software is specifically designed to simulate particles travelling in beam lines using the GEANT4 [5] toolkit. This implies that G4beamline and

TURTLE fundamentally differ in the way that they propagate particles through electromagnetic fields. TURTLE is the child of a long and very accurate linage of beam transport codes that use matrix algebra to act on a vector $X = (x, x', y, y', \ell, \delta)$ that represents the particle's position and kinematics and matrices that represent the electromagnetic fields. In principle, if one did not have intermediate apertures, want to include multiple scattering, want to track decay daughter particles, *etc.*, the entire beam line could be modeled by one matrix formed by the product of the individual matrices. The matrices are generally calculated to second order and include fringe fields. Many accelerators have been designed based on these simulations alone.

In contrast, GEANT4 and therefore G4beamline are solely stepping programs. At each step, the electromagnetic field surrounding the particle is determined; the corresponding relativistic Lorentz force is calculated and applied to the particle to propagate it to the next step. This means that G4beamline requires magnetic field maps for each element. In simple cases, such as the quadrupoles in the PiM1 channel, G4beamline provides sufficient tools such that it is possible to describe the shape of the poles and field strength and allow G4beamline to calculate the field itself. The PiM1 dipoles, however, were constructed with angled, curved pole faces. These were more difficult to model with the "sectorbend" magnet type provided by G4beamline, so a field map was generated instead.

The MUSE G4beamline model of the PiM1 beam line has significantly matured over the past year. The general model of the channel is illustrated in Fig. 35. To demonstrate the agreement between the TURTLE and G4beamline simulations, we compared simulations using similar μ^+ point-source distributions. Both the G4beamline and TURTLE source distributions are shown in Fig. 36 for a central momenta of the input sources are 155 MeV$\pm$1.5%. Figure 35 shows a sample of 5000 of these events as they traverse through the beam channel in the X-Z plane with G4beamline.

The simulation of the channel naturally depended on an accurate description of the magnet placement. The quadrupole positions were carefully verified with existing measurements that were also incorporated into the TURTLE input deck. The dipole magnets, ASM11 and ASM12 were carefully modeled to incorporate both the curved and angled pole faces. These were critical in achieving the correct dispersion at the intermediate focal point and are illustrated in Fig. 37.

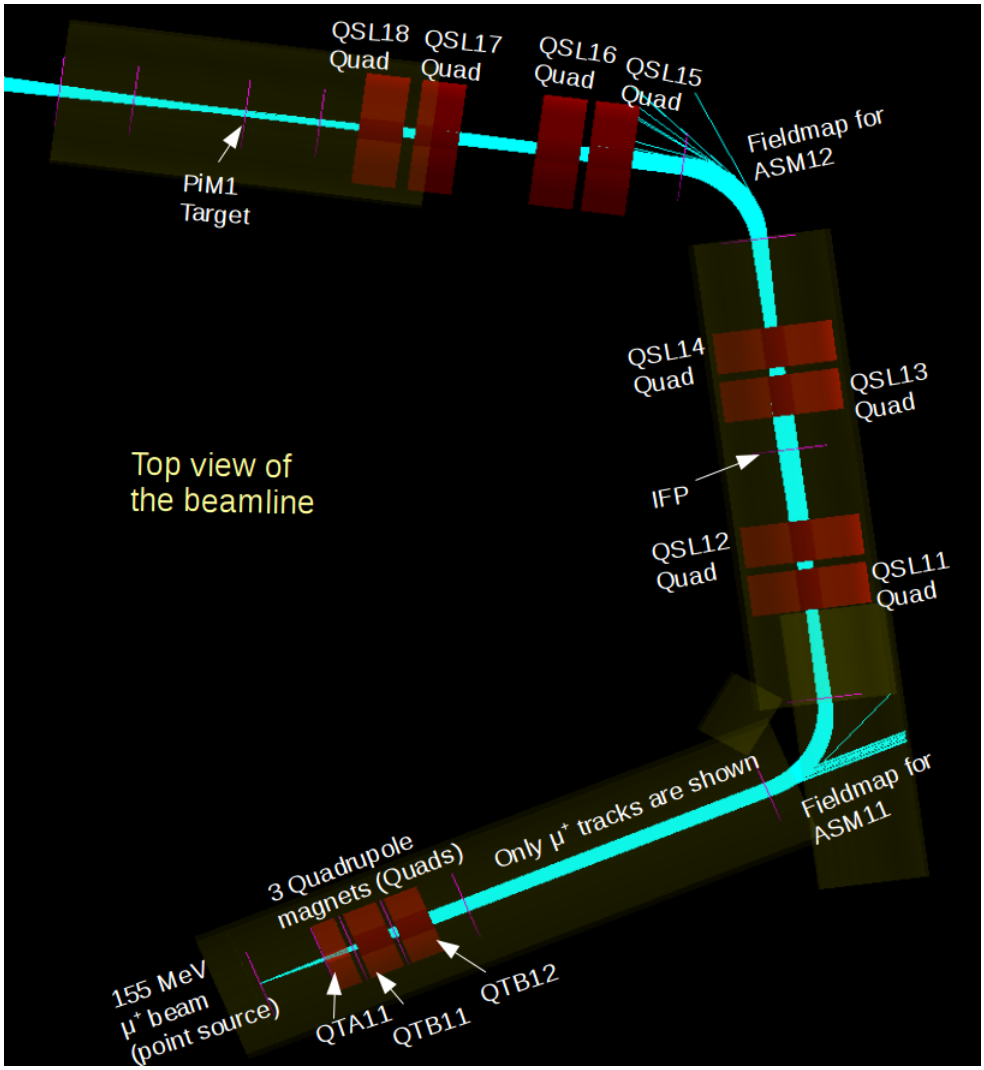

FIG. 35: The MUSE G4beamline model of the PiM1 channel. This image shows 5000 μ^+ events from a point source (described in the text). The quadrupole magnets (QTA, QTB, QSL) focus or defocus the beam in x or y directions depending on their polarities. The dipoles ASM11 and ASM12 primarily bend the beam but their pole faces also provide focusing effects. The magenta lines correspond to virtual detectors. The almost transparent cylinders enclosing the beam line correspond to shields, which eliminate particles that are scattered outside of the beam line.

We placed several virtual detectors, shown as magenta lines in Fig. 35, to study the spatial distributions and correlations at various places along the beam line. Figures 38 to 44 show such distributions and their comparison with TURTLE. Fig. 38 to 40 show that there is a good agreement between G4beamline and TURTLE up to the start of the

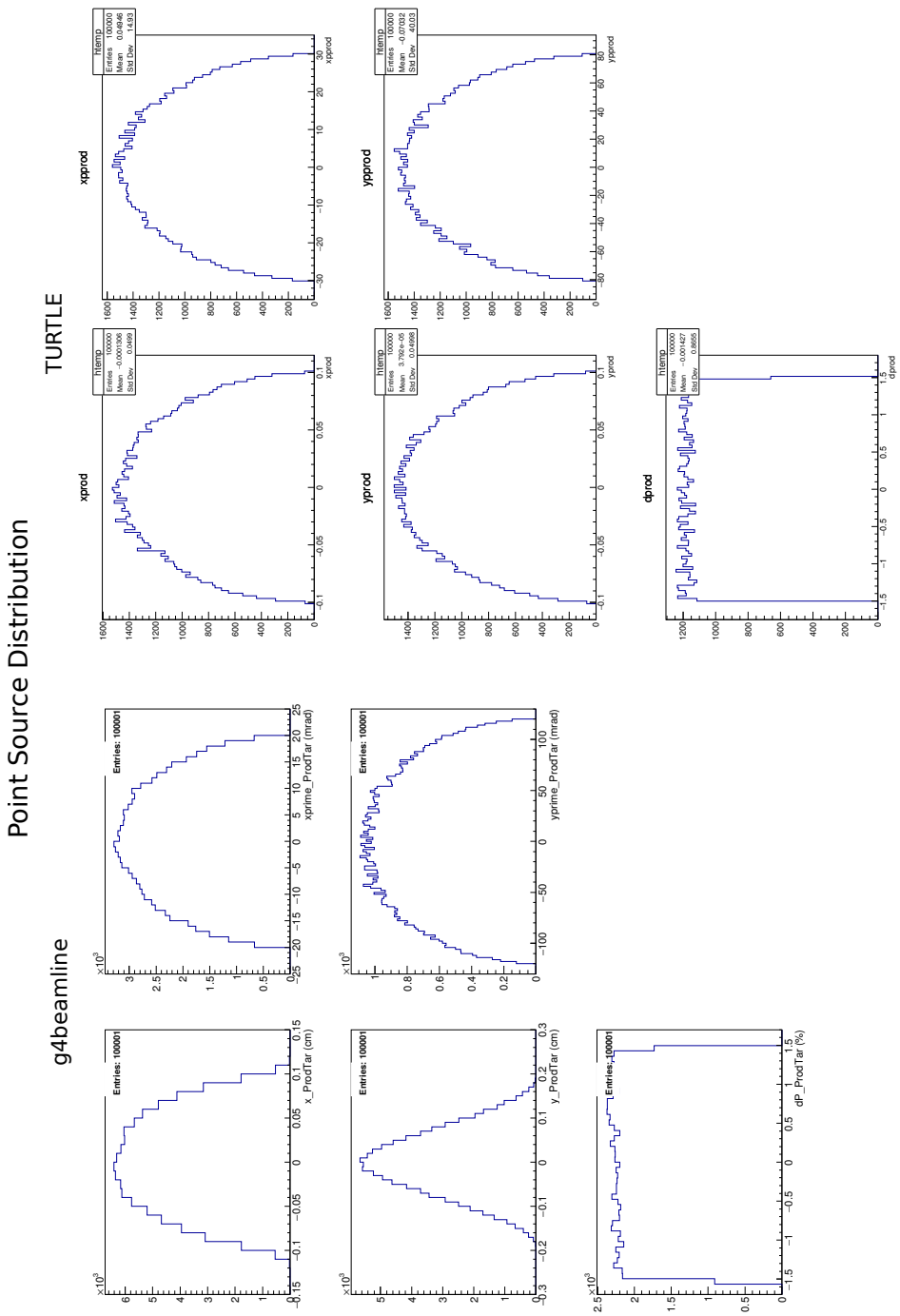

FIG. 36: A comparison of the source distributions in G4beamline and TURTLE for a 155 MeV μ^+ beam. Each simulation panel shows x (cm), x' (mrad) distributions (top row); y (cm), y' (mrad) distributions (middle row); and δ distribution (bottom row).

first dipole, thus indicating that the quadrupole magnets are simulated in a consistent

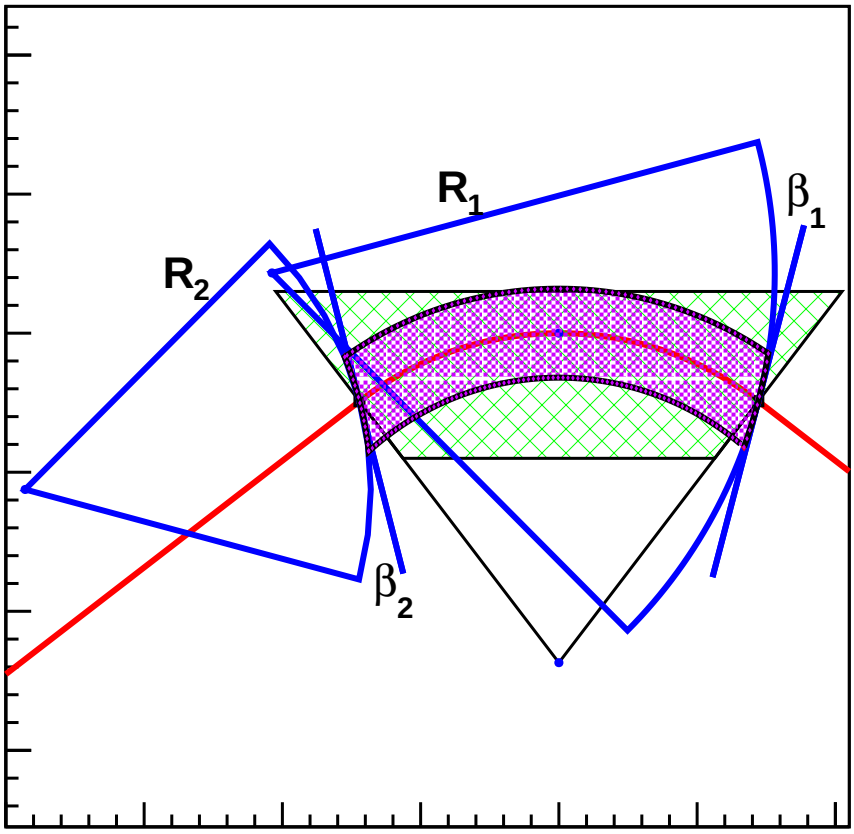

FIG. 37: Diagram showing the pole face angles and radii of curvature for the first (ASM1) dipole. The second (ASM2) dipole is a mirror image.

way by the two types of software packages. However, at the end of the first dipole, the correlations agree only to first order, as is shown in Fig. 41. This suggests that the dipole field map needs to be fine-tuned. The IFP is located almost half-way between the first dipole and the second dipole. We see that at the IFP (Fig. 42), the correlations seen using G4beamline between x, x' and δ agree to leading order with TURTLE. In fact, the momentum dispersion matches with the 7 cm/% dispersion observed using TURTLE. The correlations between y, y' and δ agree qualitatively. For instance, the bottom row shows that the central values of $y_{\rm IFP}$ are 0, independent of δ in both simulations, and the δ distributions are symmetric and centered at $y(y') = 0$. The level of agreement will likely improve once we fine-tune the field map of the ASM11 dipole.

After exiting the IFP, the beam interacts with another set of quadrupole magnets and the ASM12 dipole magnet before reaching the PiM1 target. Here again, the correlations agree qualitatively between the two simulations as shown in Fig. 43, but the level of agreement is slightly worse than what we have at the IFP. We suspect that it is due to the field map of ASM12, which is missing the entrance and exit fringe fields. These fringe fields provide important vertical focusing that would qualitatively explain the differences shown in the distributions [6]. Fig. 44 shows a comparison of the particle distributions at the PiM1 target location. Both simulations show that the y distributions are narrower than the x distributions, they are symmetric and centered at 0. The x' distributions are asymmetric with more tail on beam-right. On the other hand, the y' distributions are symmetric and centered at 0. Note that we cannot directly compare the x, y, x' and y' ranges because they were not identical in the input sources for the two simulations (see Fig. 36).

Based on the above discussion, we conclude that we have a reasonable agreement between G4beamline and TURTLE simulations. Additional work needs to be done to improve the field maps of the ASM11 and ASM12 dipoles in G4beamline. The fringe fields of the dipoles were taken into account in TURTLE but not in G4beamline. We believe that we can improve the level of agreement by adding fringe fields to the dipole field maps. This is work-in-progress.

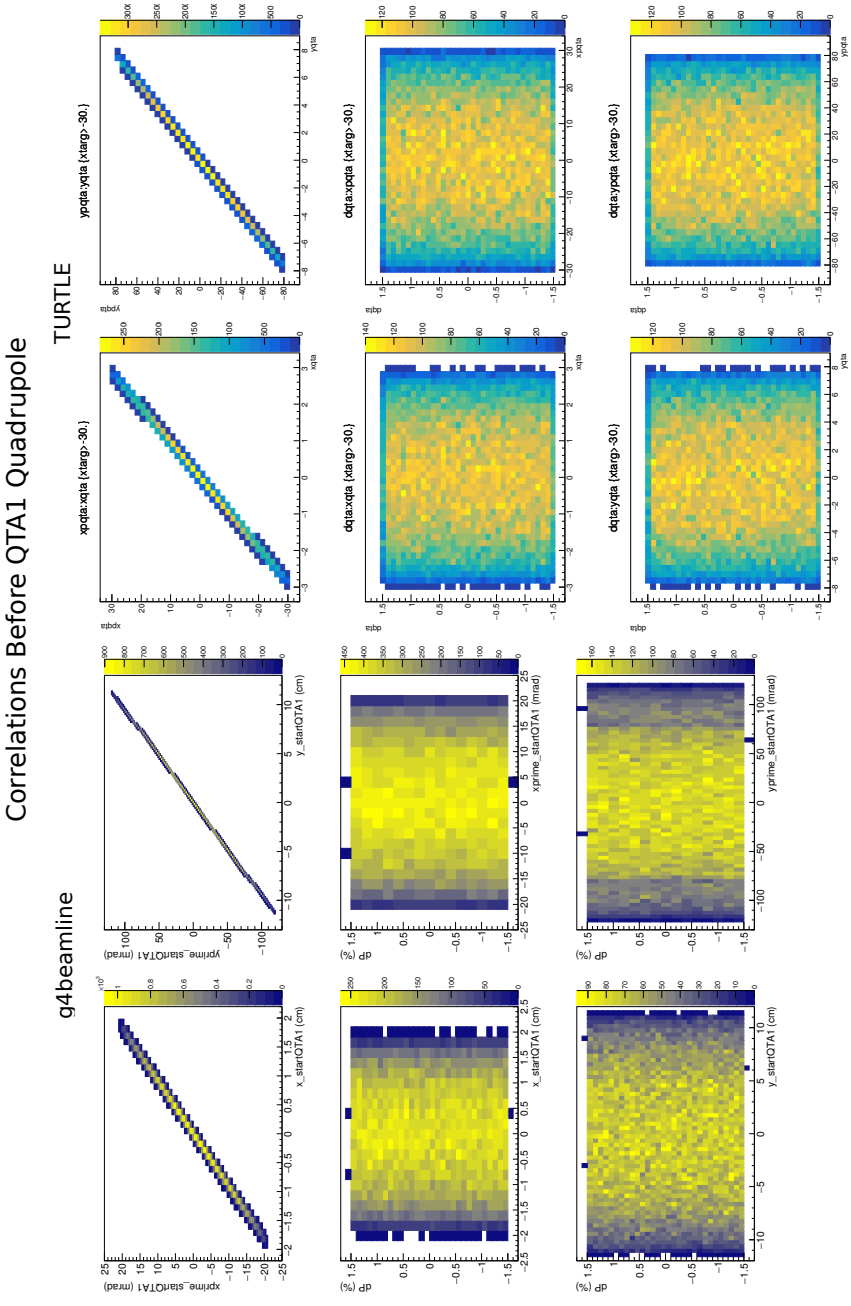

FIG. 38: A comparison of the correlations in G4beamline and TURTLE near the start of QTA11 quadrupole magnet, for a μ^+ point source. Each simulation panel shows x' versus x, y' versus y distributions (top row); δ versus x, δ versus x' distributions (middle row); and δ versus y, δ versus y' distributions (bottom row). The units are 'cm' for the spatial coordinates and 'mrad' for the angles.

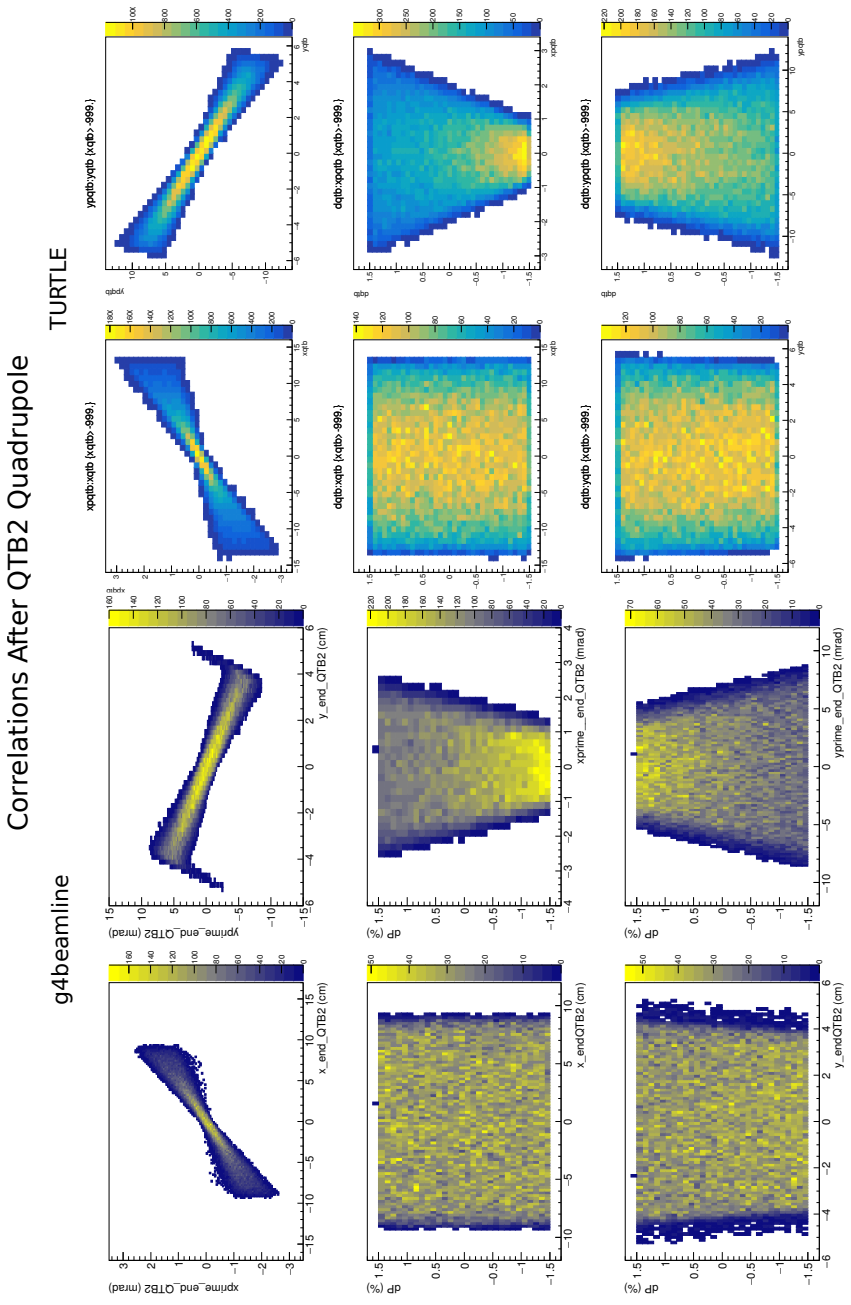

FIG. 39: A comparison of the correlations in G4beamline and TURTLE near the end of QTB12 quadrupole magnet, for a μ^+ point source. Each simulation panel shows x' versus x, y' versus y distributions (top row); δ versus x, δ versus x' distributions (middle row); and δ versus y, δ versus y' distributions (bottom row). The units are 'cm' for the spatial coordinates and 'mrad' for the angles.

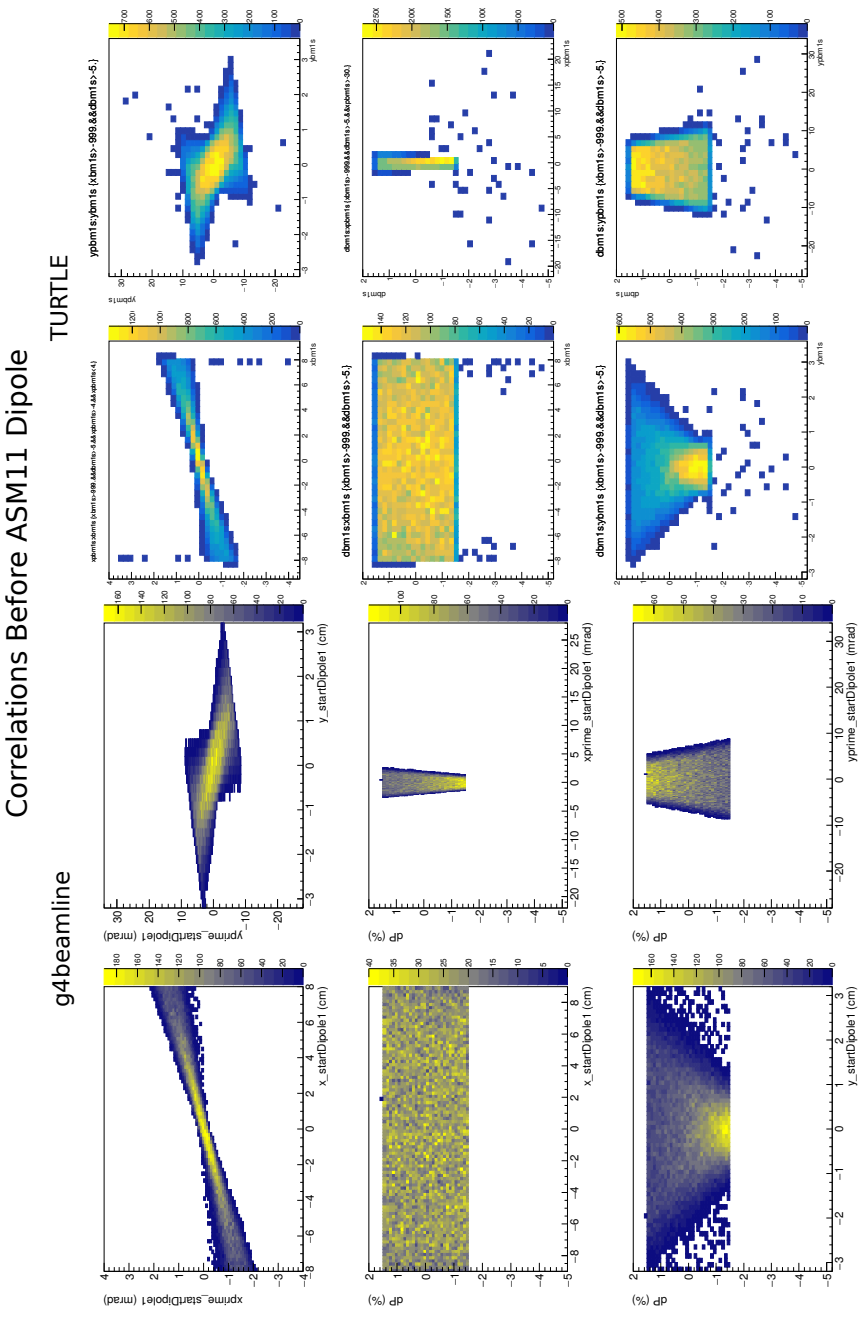

FIG. 40: A comparison of the correlations in G4beamline and TURTLE near the start of the ASM11 dipole, for a μ^+ point source. Each simulation panel shows x' versus x, y' versus y distributions (top row); δ versus x, δ versus x' distributions (middle row); and δ versus y, δ versus y' distributions (bottom row). The units are 'cm' for the spatial coordinates and 'mrad' for the angles.

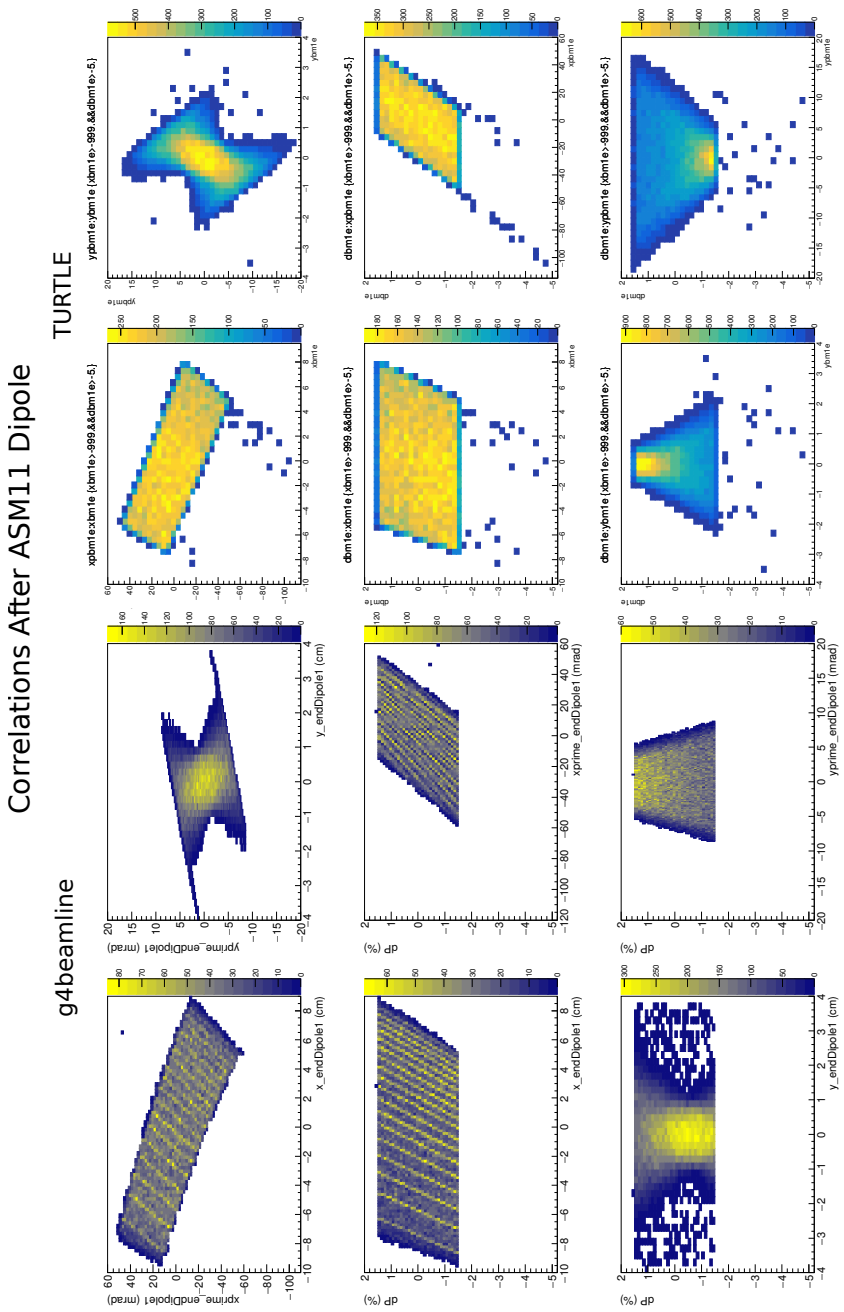

FIG. 41: A comparison of the correlations in G4beamline and TURTLE near the end of the ASM11 dipole, for a μ^+ point source. Each simulation panel shows x' versus x, y' versus y distributions (top row); δ versus x, δ versus x' distributions (middle row); and δ versus y, δ versus y' distributions (bottom row). The units are 'cm' for the spatial coordinates and 'mrad' for the angles.

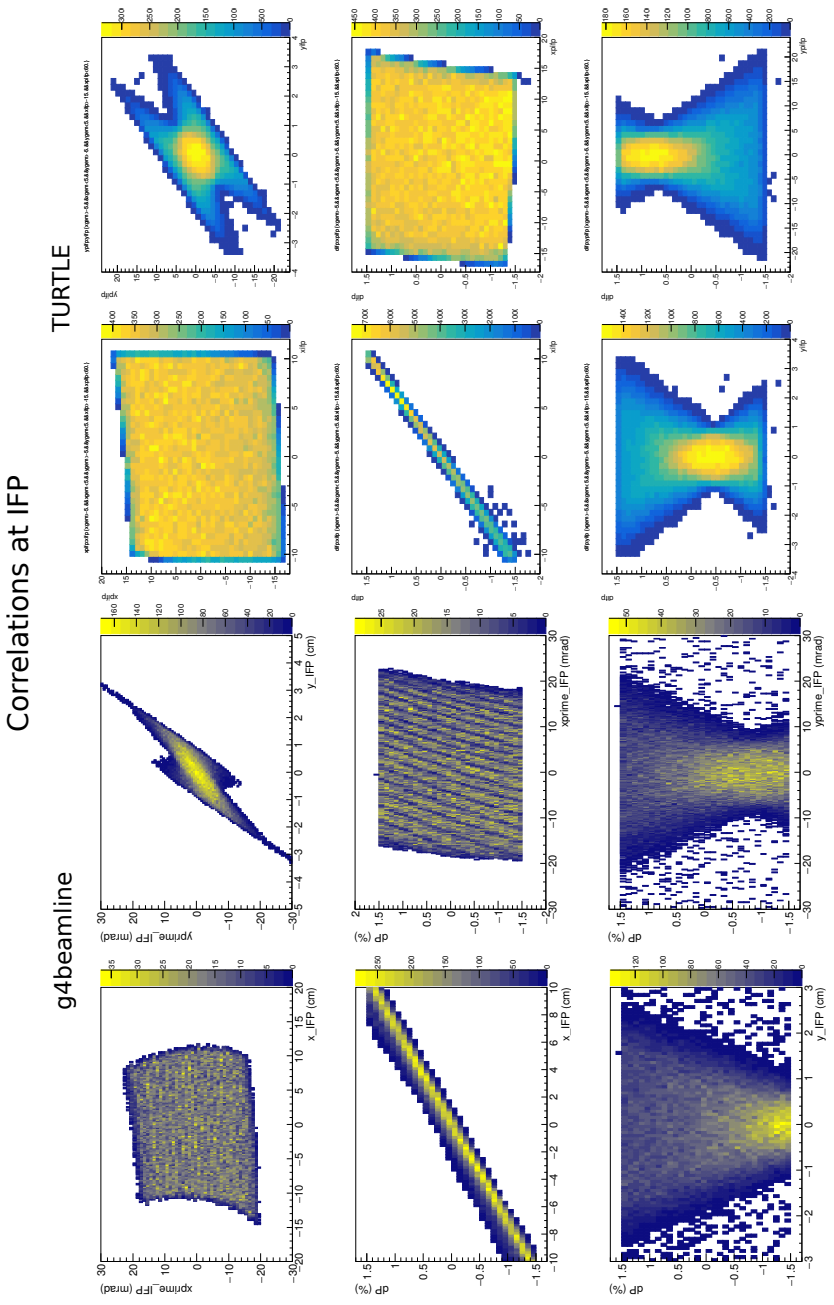

FIG. 42: A comparison of the correlations in G4beamline and TURTLE at the IFP, for a μ^+ point source. Each simulation panel shows x' versus x, y' versus y distributions (top row); δ versus x, δ versus x' distributions (middle row); and δ versus y, δ versus y' distributions (bottom row). The units are 'cm' for the spatial coordinates and 'mrad' for the angles.

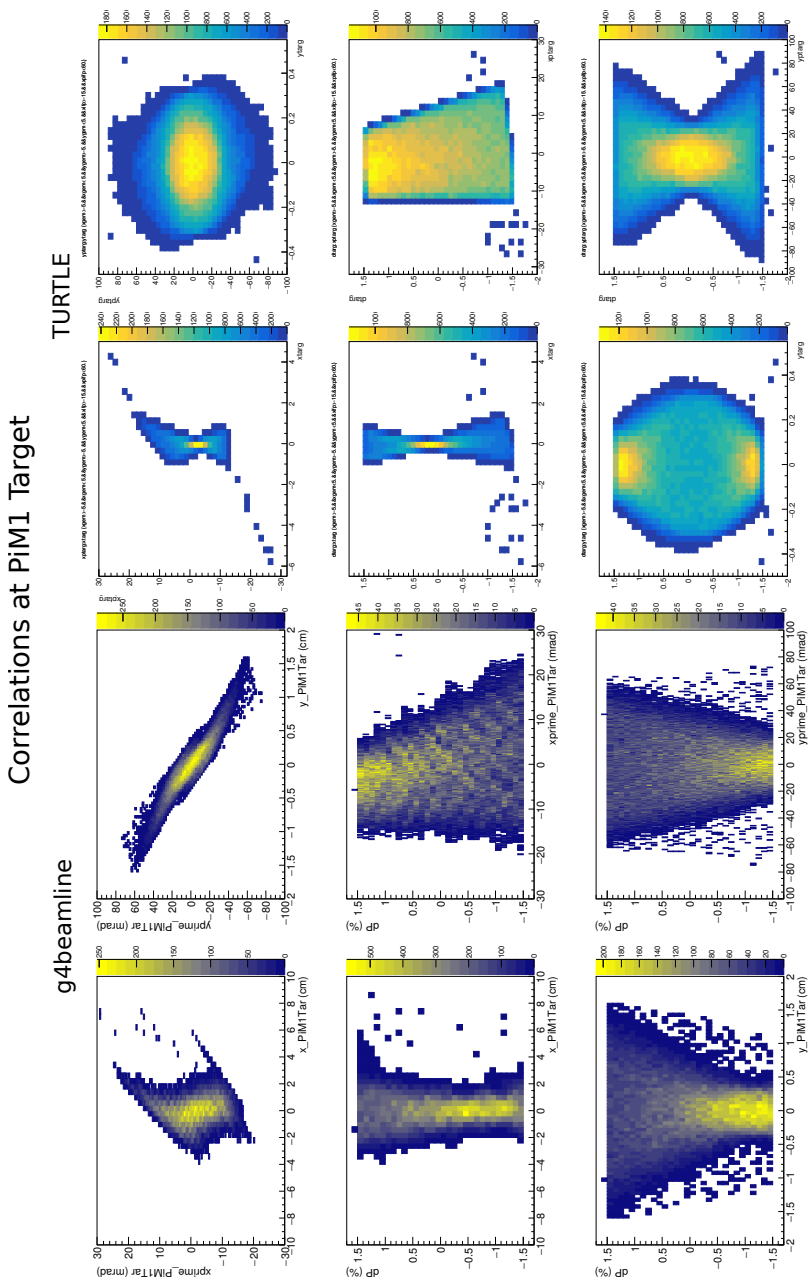

FIG. 43: A comparison of the correlations in G4beamline and TURTLE at the PiM1 target location, for a μ^+ point source. Each simulation panel shows x' versus x, y' versus y distributions (top row); δ versus x, δ versus x' distributions (middle row); and δ versus y, δ versus y' distributions (bottom row). The units are 'cm' for the spatial coordinates and 'mrad' for the angles.

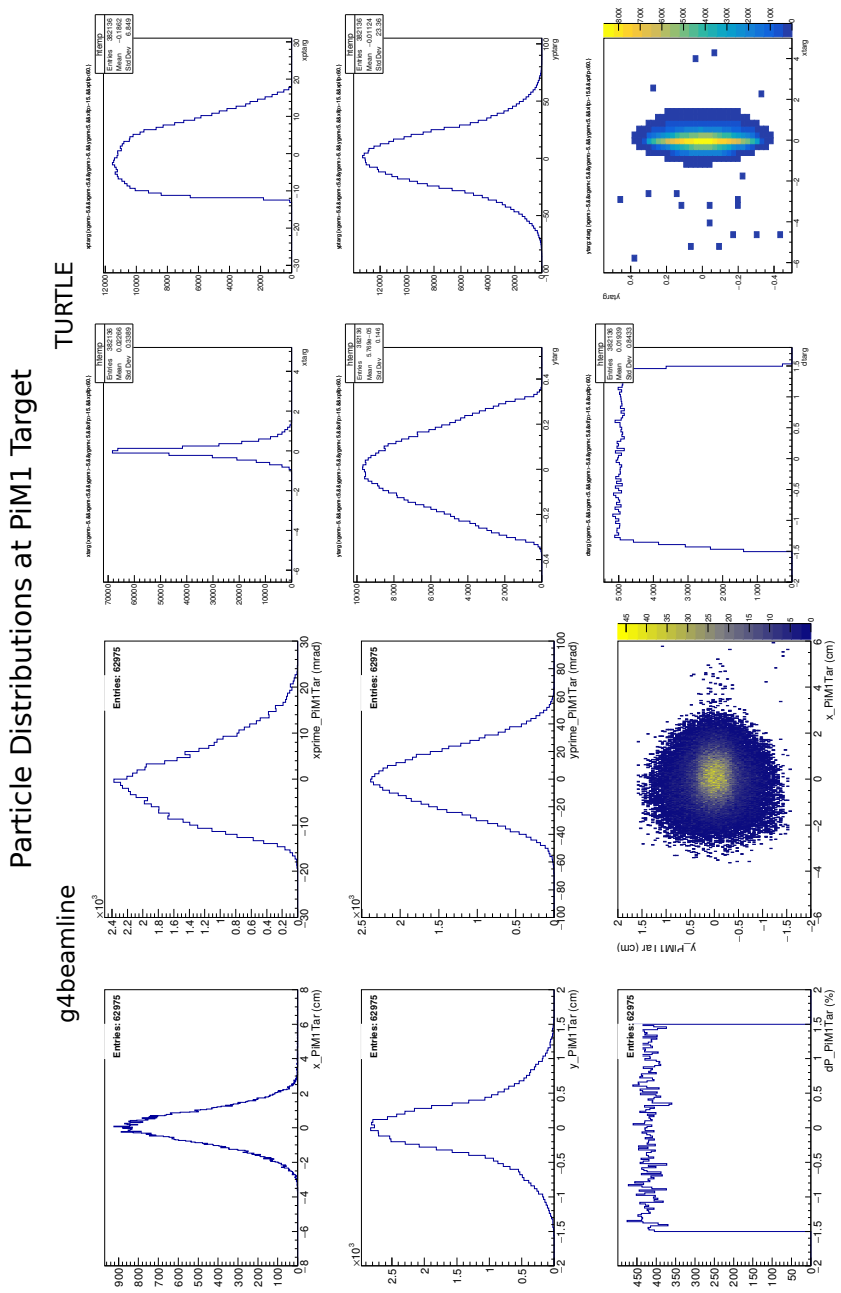

FIG. 44: A comparison of the particle distributions in G4beamline and TURTLE at the PiM1 target location, for a μ^+ point source. Each simulation panel shows x (cm), x'(mrad) distributions (top row); y (cm), y' (mrad) distributions (middle row); and δ distribution, beam spot in X-Y plane (bottom row).

TABLE II: Beam flux at the target for full PiM1 channel acceptance with 2.2 mA primary proton current. The total flux is based on previous measurements, while the relative fluxes of each particle types are based on MUSE measurements. Also shown in parentheses is the flux of each particle type when the combined flux is limited to the MUSE planned total flux of 3.3 MHz.

Momentum (MeV/c)	Polarity	Total Flux (MHz)	e Flux (MHz)	μ Flux (MHz)	π Flux (MHz)
115	+	8.3	8.05 (3.20)	0.17 (0.07)	0.08 (0.02)
153	+	16.9	10.65 (2.08)	2.03 (0.40)	4.23 (0.83)
210	+	79.2	9.50 (0.40)	6.34 (0.26)	63.36 (2.64)
115	−	7.4	7.29 (3.25)	0.07 (0.03)	0.04 (0.02)
153	−	11.9	10.71 (2.97)	0.38 (0.11)	0.81 (0.22)
210	−	24.0	11.28 (1.55)	0.96 (0.13)	11.76 (1.62)

F. Simulations in G4beamline starting with the proton beam

The TURTLE and G4beamline simulations discussed already are based on either model sources without physics input or on the pion production modeling of [2, 3]. An interesting possibility is to use G4beamline starting from the proton beam, taking advantage of GEANT4's implementation of particle shower cross sections. *Hypothetically,* if the cross sections for low-energy, hadronic showers are known well enough it would be possible simply to input a beam of 590 MeV protons onto a well described target and allow the shower code to produce the pions that in turn decay into the particles seen in the PiM1 beam channel. There are two difficulties with this approach. The first problem results from the small rate of particles accepted into the PiM1 channel per proton striking the production target as shown in Tab. II. The proton beam current is approximately 2.2 mA $= 15 \times 10^{15}$ protons/second. Consider 153 MeV. The PiM1 channel will have a rate of 11×10^6 electrons/second, or in rough numbers, 1.4×10^9 protons are needed to produce an electron that is accepted by the channel. We have found that with G4beamline, we can process about 10 kHz of protons. This translates to about 0.6 electrons/day being simulated. Thus for expediency, we have stepped past the initial proton-production target interaction step.

The second difficulty is the reliability of the hadronic shower codes at the relevant low energies. GEANT4 is excellent at reproducing the characteristics of high energy showers and electromagnetic showers. It is even successful at modeling energy deposited by low energy α particles for DNA damage studies. (See for example [7].) Recently, cascade models for intermediate energy (few GeV) hadronic showers have been successfully implemented in GEANT4 [8]. Unfortunately, detailed low-energy hadronic shower codes remain elusive. GEANT4 is able to qualitatively predict macroscopic features including energy deposited by the showers, the Molière radius of the shower and the depth of the shower in calorimetry. In terms of microscopic details of the shower, however, a comparison of GEANT4 shower simulations with the PiM1 channel is likely to teach us more about GEANT4 than about PiM1.

III. MEASUREMENTS OF BEAM PROPERTIES

We focus here on measurements of the beam momentum, since measurements of beam particle trajectories and particle identification are done for every scattering event on an event by event basis. The momentum of individual beam particles cannot be determined by our system, only the average momentum and momentum distribution of the beam coming out of the channel. We have performed two types of measurements, time of flight (TOF) measurements and dispersion measurements.

TOF is a standard technique. Measurements are made for at least two different separations of a pair of scintillators, to cancel electronic offsets and other systematics, and the velocity determined along with the mass of the particle being measured determine the particle momentum. We have previously reported to BVR committees measurements at the level of 0.2 - 0.3% uncertainty for muons and pions, using a small SiPM scintillator and a thick fast scintillator with Hamamatsu PMTs. The measurements used a specialized setup, with a scanner table to move the small scintillator over a distance of 50 cm with $\approx$10 μm precision. These measurements, taken with variable settings of the IFP collimator, confirmed the 7 cm/% dispersion at the IFP. The results indicated that our timing measurements started encountering systematic issues at the level of a few to several ps.

The MUSE experimental setup includes a beam hodoscope detector, consisting of SiPM scintillators similar to the one used before in TOF measurements, mounted on a sliding table that can be doweled into several positions. There is also a beam monitor detector, consisting of 4 thick, high-precision scintillators followed by SiPM hodoscopes planes, which slides on a rail and could be clamped against stops at either end of its range of motion. These detectors were used within the MUSE experimental setup, including GEM chambers, a veto detector, and the cryotarget vacuum chamber, to test out operating the production TOF system, including the raw data analysis and calibration procedures, and a refined TOF analysis procedure, described in more detail below, that combines Monte Carlo simulations with data to extract path lengths from the electrons and momenta for the pions and muons for individual paddle combinations.

During the data taking and subsequent analysis, several weaknesses in our initial implementation were noticed, which we plan to address with system or procedural upgrades.

- It remains the case that the precision of the TDCs becomes a question at the several ps level. We are working on methods to test and possibly improve the TDC calibrations and time determinations.

- The QDC signals for the detectors used modules with high dead times. We moved the beam monitor scintillator signals onto delay cables to QDCs to eliminate the dead-time issue, so that pulse size signals are available on an event by event basis for analysis. In the current data sample, one can only use the signals for an overall check of the simulation, comparing simulated and measured spectra shapes, or use the signals at the cost of losing much of the statistics, with only timing signals available for all event data. Of particular note is that particles can generate photons that convert part-way through the scintillator, leading to a longer flight path, later times, and smaller signals for the particle-photon coincidence, as we have seen in the data.

- Particles can, after passing through the upstream detectors, scatter off apertures such as the beam veto or scattering chamber structures, arriving with a longer flight path and later at the beam monitor. This is a feature of our production system that did not happen in our previous test system. This feature also appears in the simulations. A precise survey is needed for the Monte Carlo.

- The detectors are moved manually. In a few cases we know the detectors were not moved to the correct positions, since the analysis determines a length that indicates an alternate dowel hole was used for the beam hodoscope table. It seems clear operationally that we should use cameras or electronics to document the positions of the detectors each time they are moved.

- Issues with the collimator controls and position readback made this system not as reliable as in the past. While there was a procedure to reset and recalibrate it, the documentation is not always clear as to whether the collimator was set correctly. The checks we have performed to date indicate that the collimator was correctly set, but it seems clear operationally that we should use cameras, as a backup to the electronics, in order to securely document the opening of the collimator.

Dispersion measurements are also in principle a standard technique. The procedure was discussed in Section II D. We compare the beam distributions of different particle types, and how the particles are bent by the dipole and quadrupoles) to study how consistent their momenta are. Measurements were done with and without a pair of GEM chambers at the IFP, and, for a few measurements, without the downstream quadrupoles on. The GEMs measured particle-dependent beam distributions at the IFP, and matrix elements between the IFP and target region. Note that particles measured by the IFP GEMs undergo multiple scattering and energy loss as a result of their GEM interaction. Both of these effects are species-dependent and lead to differences in the particle species-separated distributions, even assuming their distributions were the same before the GEMs.

A. Time-of-flight measurements

1. *Formalism*

The time-of-flight (TOF) of a particle with average speed βc over a distance L is $t = L/(\beta c)$. Measured values of the time-of-flight may be different from t by a constant τ which includes delays in the detector response, cables, and electronics. As τ is unknown but constant, we do not consider absolute values of the TOF but only TOF differences. [2] A sketch of the experimental setup is shown in Fig. 45 and a list of path-lengths is given in Tab. III. Of the four different setups, we take setup L_0 as a reference in the following

[2] We *assume* here that for the TOF differences τ is an offset due mainly to detector geometry and electronics that does not change between the different detector configurations. The offset due to the position of particles in a detector is taken care of by using mean times of double-ended detectors. The TDC calibration should take care of electronics timing drifts with time or temperature.

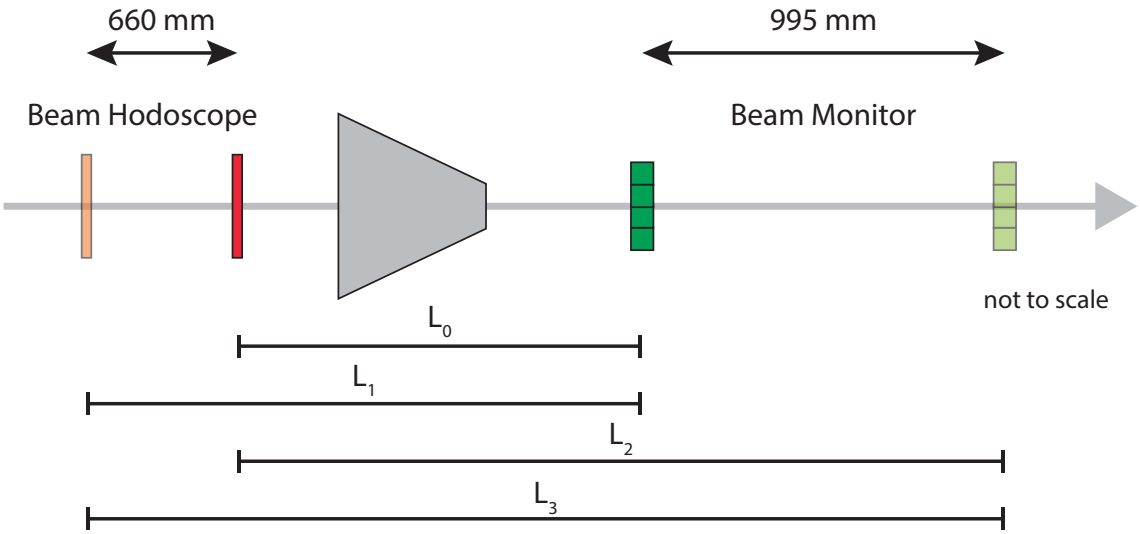

FIG. 45: Not-to-scale sketch of the MUSE setup during time-of-flight measurements. The beam is entering from the left. The beam-hodoscope and beam-monitor detectors were each positioned in two positions along the beam axis, creating four different path-lengths for the time-of-flight measurement between the two detectors.

TABLE III: Path-length L_i and path-length-difference ΔL_i relative to the L_0 setting for various configurations of the time-of-flight measurements along with simulation results of average pion speeds and energy losses at 117 and 210 MeV/c channel momentum, respectively. The path-length is given from the beam-hodoscope plane D to the beam monitor. The path-lengths from plane C are 20 mm longer.

Setup	L_i (mm)	ΔL_i (mm)	β_π^{117}	β_π^{210}	ΔE_π^{117} (MeV)	ΔE_π^{210} (MeV)
L_0	1884.4	0	0.6240	0.8294	3.53	2.27
L_1	2544.4	660	0.6246	0.8295	3.38	2.22
L_2	2879.4	995	0.6230	0.8292	3.66	2.42
L_3	3539.4	1655	0.6234	0.8293	3.61	2.29

analysis. Figure 46 shows as example three TOF spectra at various momenta for the L_1 detector setup. The TOF is taken from paddle six of plane D of the beam-hodoscope to paddle one of the beam-monitor. In all cases the TOF peaks for the three particle species are well resolved. In the simplest approximation the muon and pion speeds can then be determined from the relative times-of-flight of these particles in comparison with

the times-of-flight of electrons:

$$\beta^{\mu,\pi} = c\frac{t_i^{\mu,\pi} - t_0^{\mu,\pi}}{t_i^e - t_0^e}. \tag{1}$$

A detailed analysis, however, needs to take into account peak shapes and background. The present analysis is therefore done by comparing the measured spectra with simulated time distributions. The Geant4-based simulation includes a realistic parameterization of the particle beam, energy losses in the air and detector material, as well as all the apertures in the particle path through the MUSE setup, including the scattering chamber. It takes into account scattering processes that change path lengths and energy loss processes that change particle speeds. Typical pion energy losses and particle speeds are given in Table III. Examples of speed distributions are given in Fig. 48. It is important that the analysis takes these variations into account as they correspond to momentum variations that are similar to the goal accuracy of $dp/p \lesssim 0.3\%$. Background from particle interactions with the scattering chamber is visible in Fig. 46 as a peak at about 19.5 ns in the 161 MeV/c example. That background is closer to the pion peak at 210 MeV/c and outside the limits of the histogram at 117 MeV/c. Also, this experimental background has to be properly modeled as it can affect the determination of the time-of-flight of the particles of interest.

a. Determination of the actual flight-path differences The difference of the measured TOF of electrons for two settings is related to the path-length differences of the settings,

$$(t_i^{\rm exp} - \tau) - (t_0^{\rm exp} - \tau) = (L_i^{\rm exp} - L_0^{\rm exp})\,\frac{1}{c}\,;$$

and similarly for the simulated TOF,

$$t_i^{\rm sim} - t_0^{\rm sim} = \left(L_i^{\rm sim} - L_0^{\rm sim}\right)\frac{1}{c}\,.$$

With $\Delta L_i = L_i - L_0$,

$$\Delta t_i = \left(t_i^{\rm exp} - t_i^{\rm sim}\right) - \left(t_0^{\rm exp} - t_0^{\rm sim}\right) = \left(\Delta L_i^{\rm exp} - \Delta L_i^{\rm sim}\right)\frac{1}{c}.$$

The time differences $\delta_i = t_i^{\rm exp} - t_i^{\rm sim}$ and $\delta_0 = t_0^{\rm exp} - t_0^{\rm sim}$ are mostly equal to the time offset τ. The difference of these differences, the time mismatch $\Delta t_i = \delta_i - \delta_0$, is generally small. Non-zero values are due to deviations between experiment and simulation in the actual

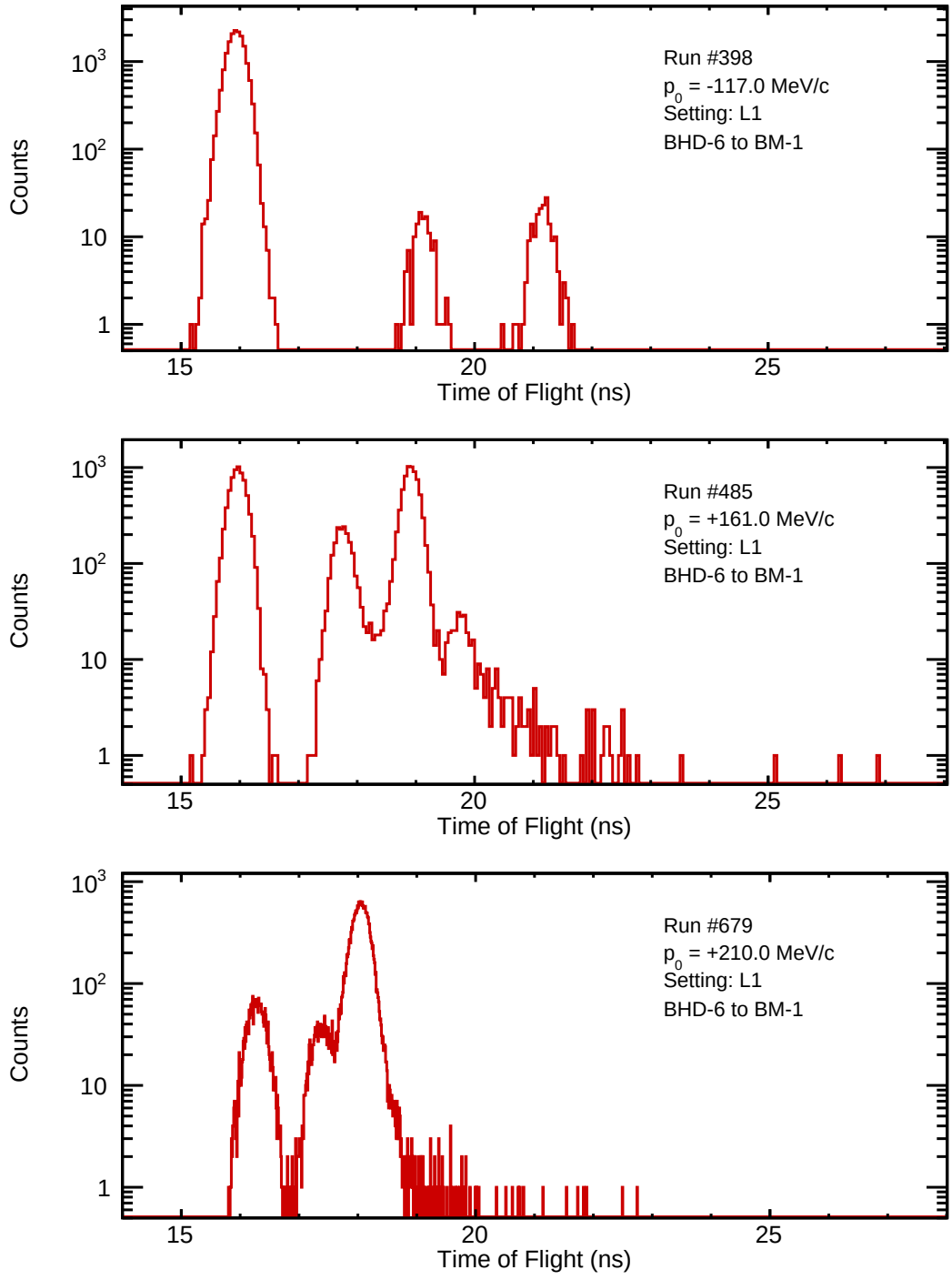

FIG. 46: Three example spectra of the TOF from the beam-hodoscope, plane D, to the beam-monitor in the L_1 setting at nominal channel-momentum of 117, 161, and 210 MeV/c. From low to high TOF, the peaks correspond to electron, μ, and π particles. In these distributions, the TOF includes cable offsets.

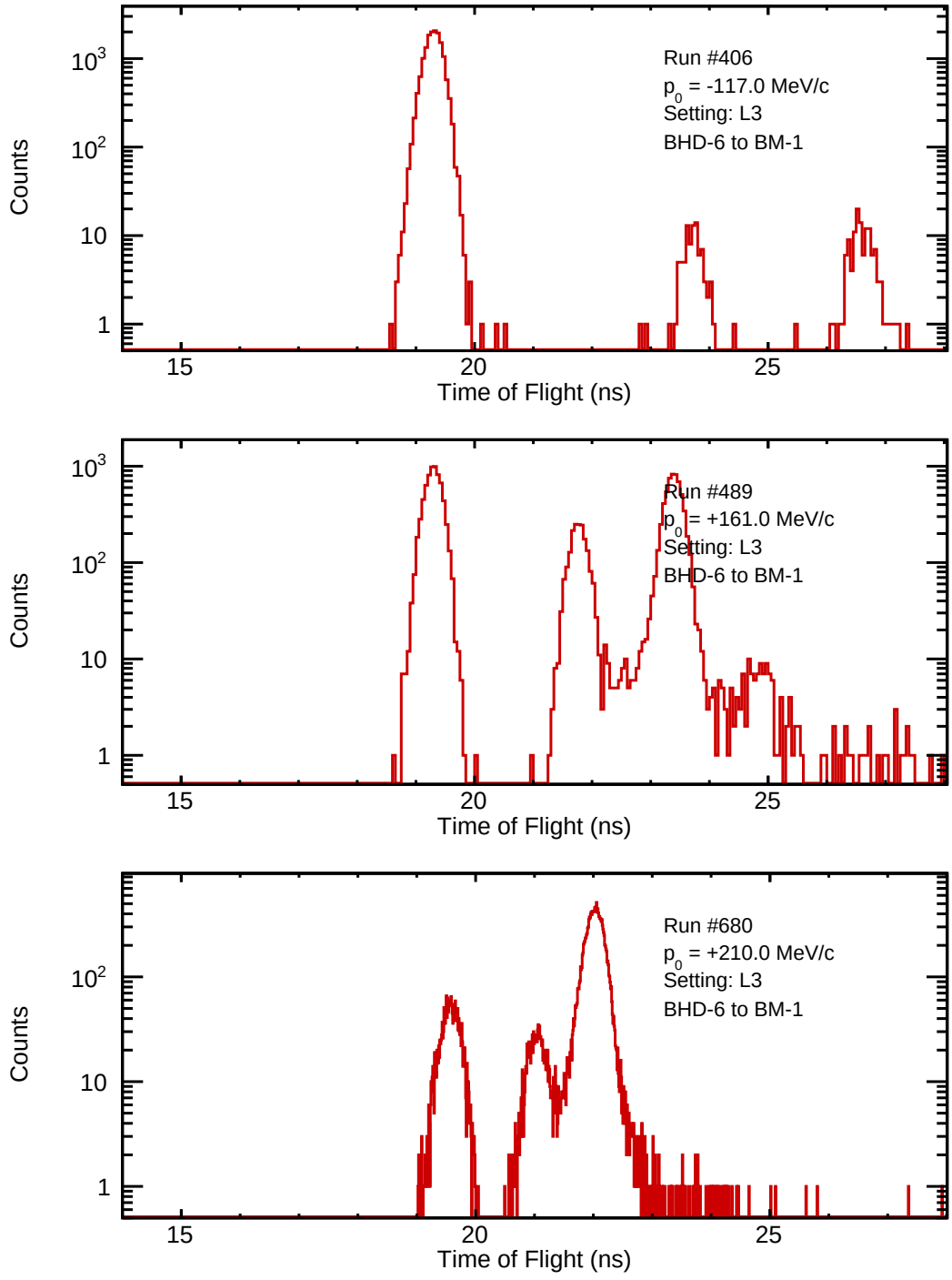

FIG. 47: Three example spectra of the TOF from the beam-hodoscope, plane D, to the beam-monitor in the L_3 setting at nominal channel-momentum of 117, 161, and 210 MeV/c. From low to high TOF, the peaks correspond to electron, μ, and π particles. In these distributions, the TOF includes cable offsets.

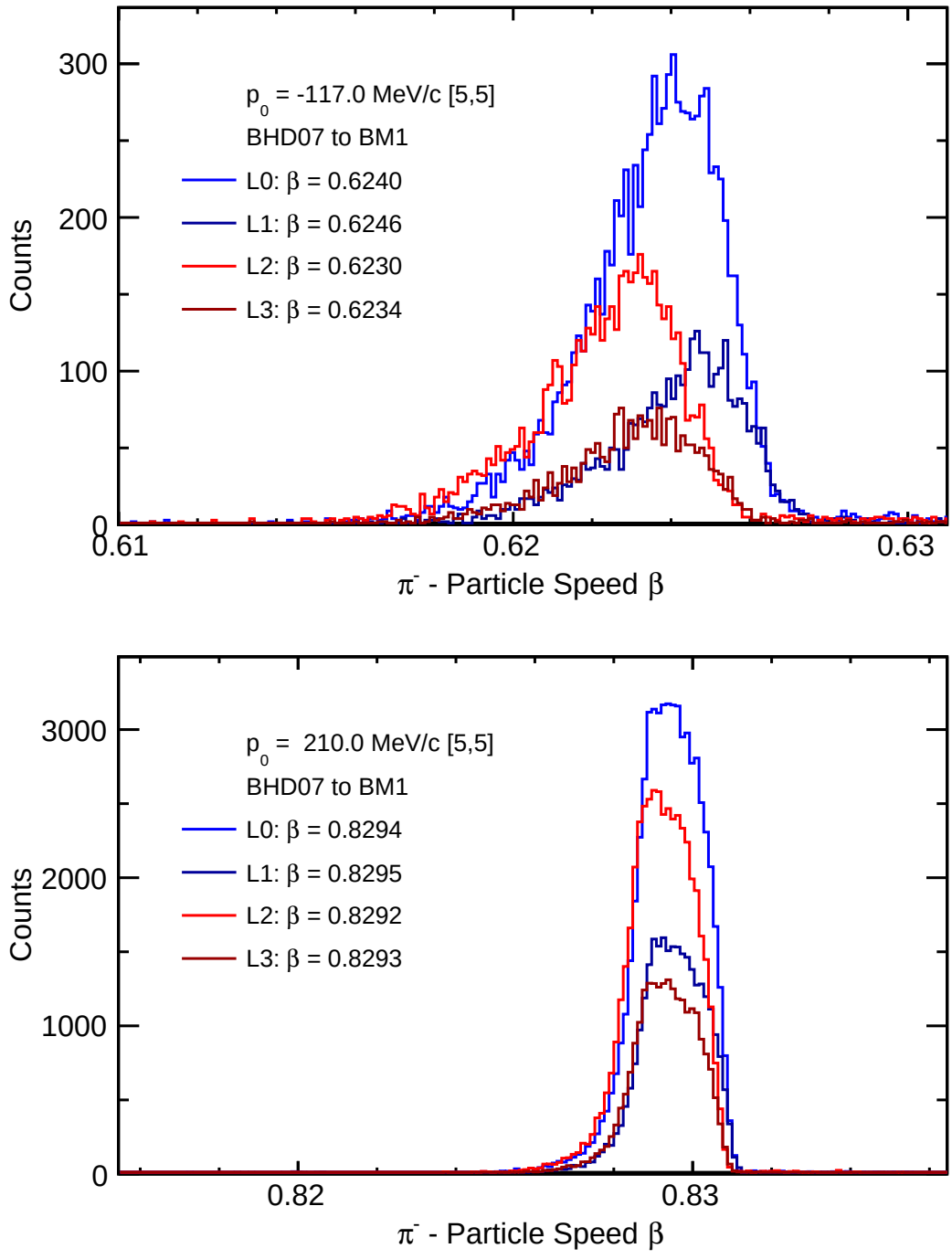

FIG. 48: Examples of simulated speed distributions for pions at channel-momentum settings of 117 and 210 MeV/c.

and assumed values for the path-lengths and, for muons and pions, the particle momenta. If the simulation describes the experiment fully, $\Delta t_i = 0$ for all settings. As described below, Δt_i is determined by a fit of the simulated to the measured TOF distributions. With the obtained Δt_i^e for the electron TOF and from the assumed path-length difference in the simulation, ΔL^{sim}, the actual path-length difference can be obtained,

$$\Delta L_i^{\mathrm{exp}} = \Delta L_i^{\mathrm{sim}} + c\Delta t_i^e \ . \tag{2}$$

We have extracted the experimental path-length differences mostly to study systematic effects. Its final value does not directly enter the momentum determination, but can be compared with the well-known path change when the beam-hodoscope is repositioned on the dowel-pin controlled sliding table, $\Delta L_1 = 660$ mm.

b. Determination of average particle speeds The timing mismatch between measured and simulated muon and pion TOF depends on the average speeds β_i of particles for the flight paths L_i.

$$c\Delta t_i^{\mu,\pi} = \left(\frac{L_i^{\mathrm{exp}}}{\beta_i^{\mathrm{exp}}} - \frac{L_0^{\mathrm{exp}}}{\beta_0^{\mathrm{exp}}}\right) - \left(\frac{L_i^{\mathrm{sim}}}{\beta_i^{\mathrm{sim}}} - \frac{L_0^{\mathrm{sim}}}{\beta_0^{\mathrm{sim}}}\right) \tag{3}$$

$$= \frac{\Delta L_i^{\mathrm{exp}}}{\beta_i^{\mathrm{exp}}}\left[1 + \underbrace{\frac{L_0^{\mathrm{exp}}}{\Delta L_i^{\mathrm{exp}}}\left\{1 - \frac{\beta_i^{\mathrm{exp}}}{\beta_0^{\mathrm{exp}}}\right\}}_{\epsilon^{\mathrm{exp}}}\right] - \frac{\Delta L_i^{\mathrm{sim}}}{\beta_i^{\mathrm{sim}}}\left[1 + \underbrace{\frac{L_0^{\mathrm{sim}}}{\Delta L_i^{\mathrm{sim}}}\left\{1 - \frac{\beta_i^{\mathrm{sim}}}{\beta_0^{\mathrm{sim}}}\right\}}_{\epsilon^{\mathrm{sim}}}\right] \tag{4}$$

The terms ϵ are at most 0.5% for the worst case of low-momentum pions; moreover, they are approximately equal, $\epsilon^{\mathrm{exp}} \approx \epsilon^{\mathrm{sim}}$ for a proper simulation. Ignoring these terms result in an undetectable modification of the time mismatch Δt by a factor $1 - \epsilon$,

$$c\Delta t_i^{\mu,\pi} \approx \frac{\Delta L_i^{\mathrm{exp}}}{\beta_i^{\mathrm{exp}}} - \frac{\Delta L_i^{\mathrm{sim}}}{\beta_i^{\mathrm{sim}}}. \tag{5}$$

This approximation allows the determination of the experimental particle speeds:

$$\beta_i^{\mathrm{exp}} = \frac{\Delta L_i^{\mathrm{exp}}}{c\Delta t^{\mu,\pi} + \frac{\Delta L_i^{\mathrm{sim}}}{\beta_i^{\mathrm{sim}}}} \tag{6}$$

$$= \beta_i^{\mathrm{sim}} \frac{\Delta L_i^{\mathrm{sim}} + c\Delta t_i^e}{\Delta L_i^{\mathrm{sim}} + c\beta_i^{\mathrm{sim}}\Delta t_i^{\mu,\pi}}. \tag{7}$$

Equation (7) was used in this analysis with the fitted time mismatches Δt_i and the path-length and speed results of the simulation. With the approximation that speed differences between various setups are small, $\beta_i \approx \beta_0$, Eq. (7) reduces to Eq. (1). While this

approximation was not made in the analysis, it shows that the experimental determination of the μ and π speeds is a *relative* time measurement to the e measurements and a comparison with the speed of light. Linear scale errors of the time measurements cancel.

c. Determination of the incident particle momentum To a good approximation, the average particle momentum can be determined from the average particle speeds $\beta_i^{\rm exp}$. The so determined momentum, however, is not the initial momentum at the beginning of the MUSE setup. To obtain the initial momentum, the average energy of the particle that travels from the beam hodoscope to the beam monitor needs to be corrected for the energy loss ΔE on that path. We determine ΔE from the results of our simulation as the difference of the kinetic energy of the incident particle and the kinetic energy of the particle with average speed β_i,

$$\Delta E_i^{\rm sim} = E_0^{\rm sim} - E^{\rm sim}(\beta_i^{\rm sim}) \tag{8}$$

Typical values of ΔE are given in Table III. The initial particle momentum is then given by the experimentally determined kinetic energy of the particle and the energy-loss correction from the simulation:

$$p_0^{\rm exp} = \sqrt{(E_0^{\rm exp} + m)^2 - m^2} \tag{9}$$

with

$$E_0^{\rm exp} = E_i^{\rm exp}(\beta^{\rm exp}) + \Delta E_i^{\rm sim}. \tag{10}$$

2. Simulations

a. Setup We have simulated the TOF measurement using a realistic beam parameterization and the full MUSE setup. The simulation includes all relevant physics processes including particle-energy losses through the air and the MUSE detector, multiple scattering, Bremsstrahlung production, and particle decay. For each particle type, channel momentum, and channel polarity we threw one million events. Hits of the primary and secondary particles were recorded in the paddles of the beam hodoscope and beam monitor. Hit information includes the hit position and time, as well as the energy deposition in the detector.

b. Pulse height Cuts were made in the simulated pulse-height distributions to reflect the detection threshold of the measured distributions in the beam-hodoscope and beam-monitor.

c. Time response The particle TOF was determined by the time difference between the first interaction of a (primary or secondary) particle with the scintillation material of a given beam-monitor or beam-hodoscope paddle. We have not simulated the detailed time response of a scintillation detector such as the light transport to the photomultiplier. The assumption is made that for a given particle type the time response does not change when the detector is repositioned. In the relative measurement, the unknown but constant time response cancels. The simulated time response does not include the limited time resolution of the detector or readout electronics. The finite time resolution of the experiment is taken into account in the fitting of the simulated distributions to the measured ones; see Sec. III A 3 a.

Figure 49 shows simulated electron time-of-flight distributions for the L_1 setup. The

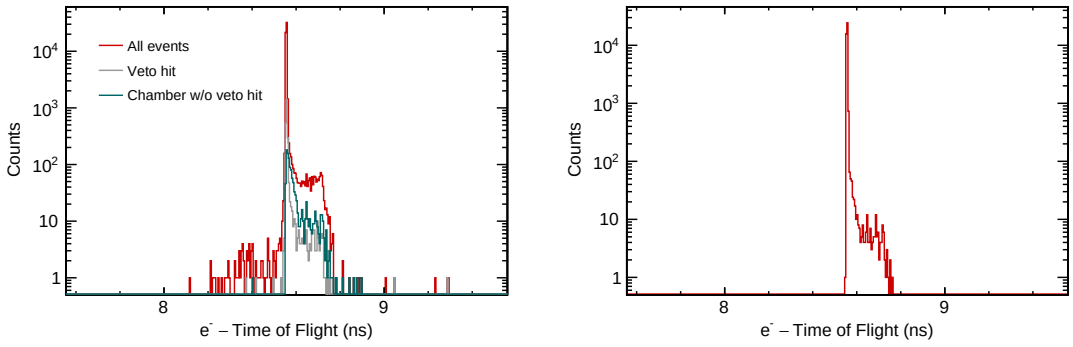

FIG. 49: Simulated electron time-of-flight distributions for the L_1 setup and a nominal channel momentum of 161 MeV/c. TOF is measured from beam hodoscope paddle C7 to beam-monitor paddle one. The left panel shows all simulated events (red), the events that interacted with the veto detector (gray), and the events that interacted with the scattering-chamber without leaving a signal in the veto detector. The right panel shows the same distribution after applying the detector-exclusivity and veto-detector cuts.

nominal channel momentum is 161 MeV/c, and the TOF is measured from beam hodoscope paddle C7 to beam-monitor paddle one. The red histogram in the left panel shows

all simulated events. A very narrow peak dominates it at the expected electron flight time. A good fraction of the events also shows flight times that are up to about 200 ps larger. The 200 ps correspond to the thickness of the width of the beam-monitor scintillator bars of 6 cm. These background events are mostly due to upstream Bremsstrahlung processes followed by Compton scattering in the beam-monitor or due to secondaries from processes in neighboring beam-monitor material that create hits in the decisive BM bar. These events *stop* the time-of-flight measurement 'too late' compared to direct hits by electrons. Similar interaction, primarily Bremsstrahlung and Compton scattering, in the beam hodoscope *start* the TOF measurement 'too late' and cause background at the shorter time of flights. However, the much thinner beam hodoscope paddles make these effects very unlikely. Both of these classes of background events can be substantially suppressed with the requirement to only use events with one and only one hit in a given beam hodoscope plane and one and only one hit in the big bars of the beam monitor; the 'exclusivity cut.' The gray histogram shows those events that also had interactions with the MUSE veto detector. These events are easily removed by a veto-detector cut in the final analysis. The green histogram marks events that interacted with the scattering chamber. This background is present in all four settings. It is most prominent in the L_1 setting, where the sliding table, and with it, the veto detector is moved upstream. In the L_1 configuration, the beam monitor is also upstream providing a large acceptance for the background events. The right panel in Fig. 49 shows the electron time-of-flight distribution after applying the detector-exclusivity and veto-detector cuts. The cuts largely reduce the background. This distribution was used in the fit of electron time-of-flight data.

Figure 50 shows, similarly to Fig. 49, a simulated muon time-of-flight distribution for the L_1 setup. The dominant TOF peak of the primary particles is wider than in the case of electrons, presumably due to variations in the muon speeds. The event distribution in the left panel shows background from muon interactions with the veto detector and scattering chamber.

Finally, Fig. 51 shows a simulated pion time-of-flight distribution. The distribution features a broad background from pion decays with the decay muon arriving at the beam monitor. The spectrum otherwise shows qualitatively similar features to the muon distribution.

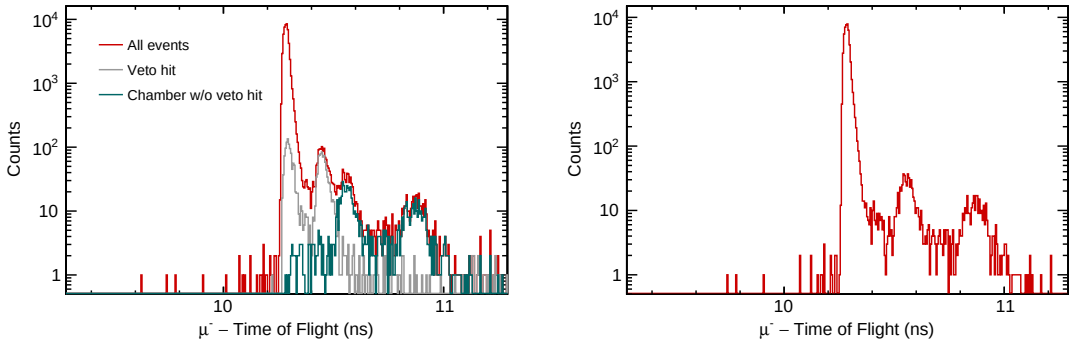

FIG. 50: Same as Fig. 49 but for muons.

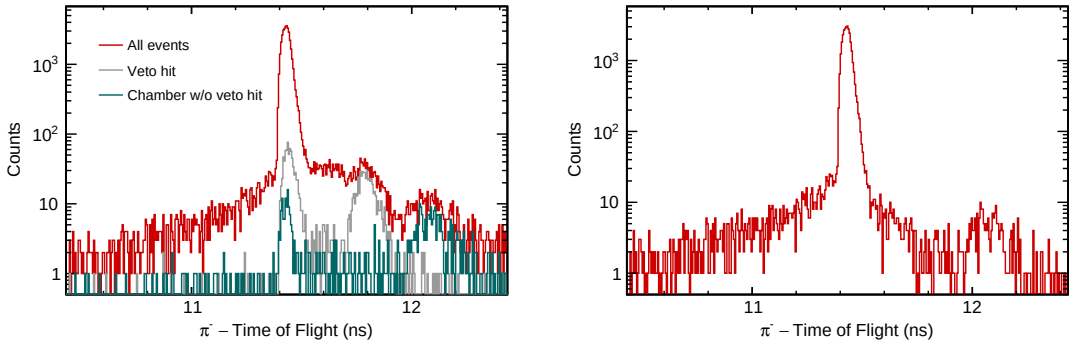

FIG. 51: Same as Fig. 49 but for pions.

d. Path length The path length was determined in the simulation as the distance between the particle hit positions in the beam-hodoscope and beam-monitor, respectively. Figure 52 shows the simulated distribution of electron path-lengths in the L_1 setup and with a channel momentum of 161 MeV/c. The sharp rise at short path lengths is marked with a vertical dashed line. It correspond to the geometrical distance between the front face of the beam-hodoscope plane C and the front face of the beam monitor paddles, $\Delta z = 2564.4$ mm. The second vertical line indicates the mean value of the path-length distribution, $\langle L \rangle$, and is about 0.5 mm larger. In this analysis, we have used the mean value. Differences between the mean value for the path length and the geometrical difference of detector positions are typically less than 1 mm. For the momentum determination,

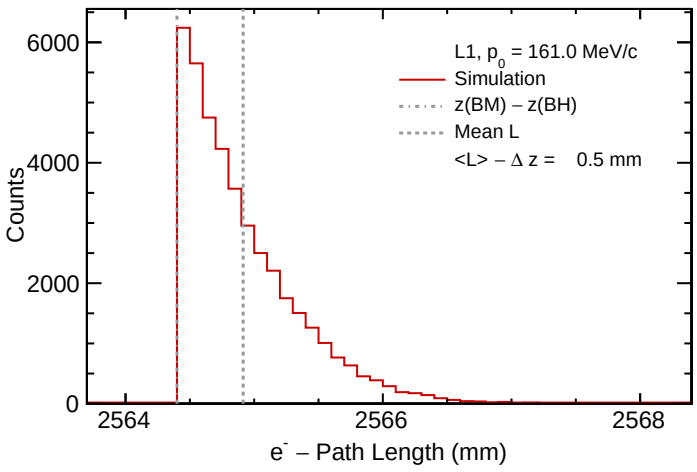

FIG. 52: Example of a simulated path-length distribution for electrons in the L_1 setup and with a channel-momentum of 161 MeV/c. The beam-hodoscope plane C was used for this simulation.

only the path-length differences matter. Using Δz or $\langle L \rangle$ does typically not affect the estimate of the path-length difference by more than 0.1 mm.

e. Average speed The average particle speed was determined in the simulation per event from the path length and time-of-flight. A typical histogram of pion speeds is shown in Fig. 53 for the L_1 setup at 161 MeV/c. The distribution is fit with a Gaussian function shown as a dashed curve in Fig. 53. We have used in the analysis the peak position of the Gaussian function as an estimate of the average particle speed. Alternatively, we have also used the mean value of the histogram. The differences are small as long as the histogram mean value is determined in a range close to the peak. Either method gives statistically consistent results for the momentum. Background events may have different speeds and we attempted to not include those in the speed average as the time-of-flight comparison with the experiment is also only made close to the signal peak. Typical average speed results for the 117 MeV/c and 210 MeV/c settings are given in Table III.

3. Analysis

a. Fits Experimental time-of-flight distributions were prepared for each channel-momentum setting, for all beam hodoscope paddle and beam monitor paddle combina-

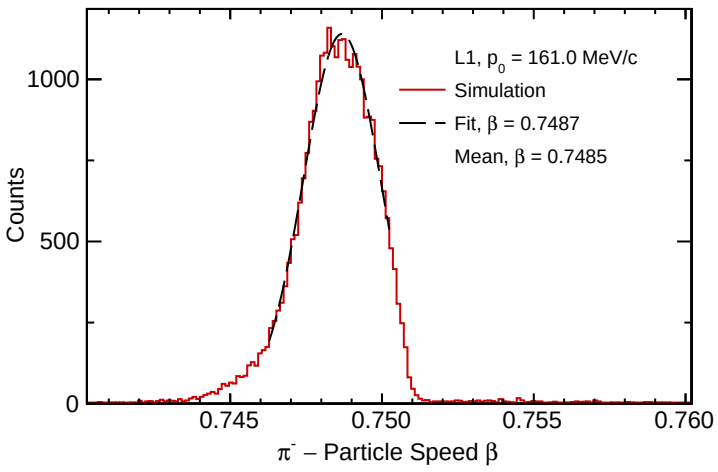

FIG. 53: Example of a simulated speed distribution for pions in the L_1 setup and with a channel-momentum of 161 MeV/c. The beam-hodoscope plane C was used for this simulation.

tions with sufficient statistics, and electrons, muons, and pions separately. The particle identification was made with the beam hodoscope time using the accelerator RF. The detector exclusivity cut was applied, and the MUSE veto detector was used to suppress background. Simulated time-of-flight distributions that match the experimental event-selection cuts closely were folded with a Gaussian distribution to imitate detector and electronic time-resolution effects and fit to the experimental distribution using simulated data. The fit function has three free parameters:

1. The standard deviation of the Gaussian distribution that was used to fold the simulated spectrum.

2. The time difference δ between the experimental and simulated distribution. This parameter encompasses multiple effects: detector, electronic, and cable delays, as well as mismatches between the assumed and actual path length or momentum of the particles.

3. The normalization of the simulated data to fit the yield of the experiment.

Figures 54 and 55 give examples of such fits. We have chosen the L_0 setup as an example which is the reference setup with the shortest path length, and the L_1 setup,

which has a well known increased path-length by 660 mm and is also the setup with the largest amount of background. In this example, the channel momentum was set to 161 MeV/c momentum and negative polarity, the collimator was set to its central position, and flight times were measured from the beam hodoscope paddle C9 to the beam monitor bar one. Electrons, muons, and pions were selected by RF time for the three panels in each figure, respectively. The muon time-of-flight distribution shows side peaks that are random coincidences from the much more abundant electrons and pions. These side peaks, however, are well separated from the muon peak of interest. The red curves are the folded, shifted, and normalized simulated distributions that are fit to the data. The time shift, δ, and the standard deviation, σ_t, are fit parameters and are indicated. For comparison, with the 'intrinsic' widths of the time-of-flight peaks, the green histograms show the original simulated distributions that have been shifted to fit the data but are not folded with a Gaussian distribution. Those distributions are arbitrarily scaled to one half of the time-of-flight peak. We include for comparison also results of a simple fit of a Gaussian distribution to the data as a dotted curve.

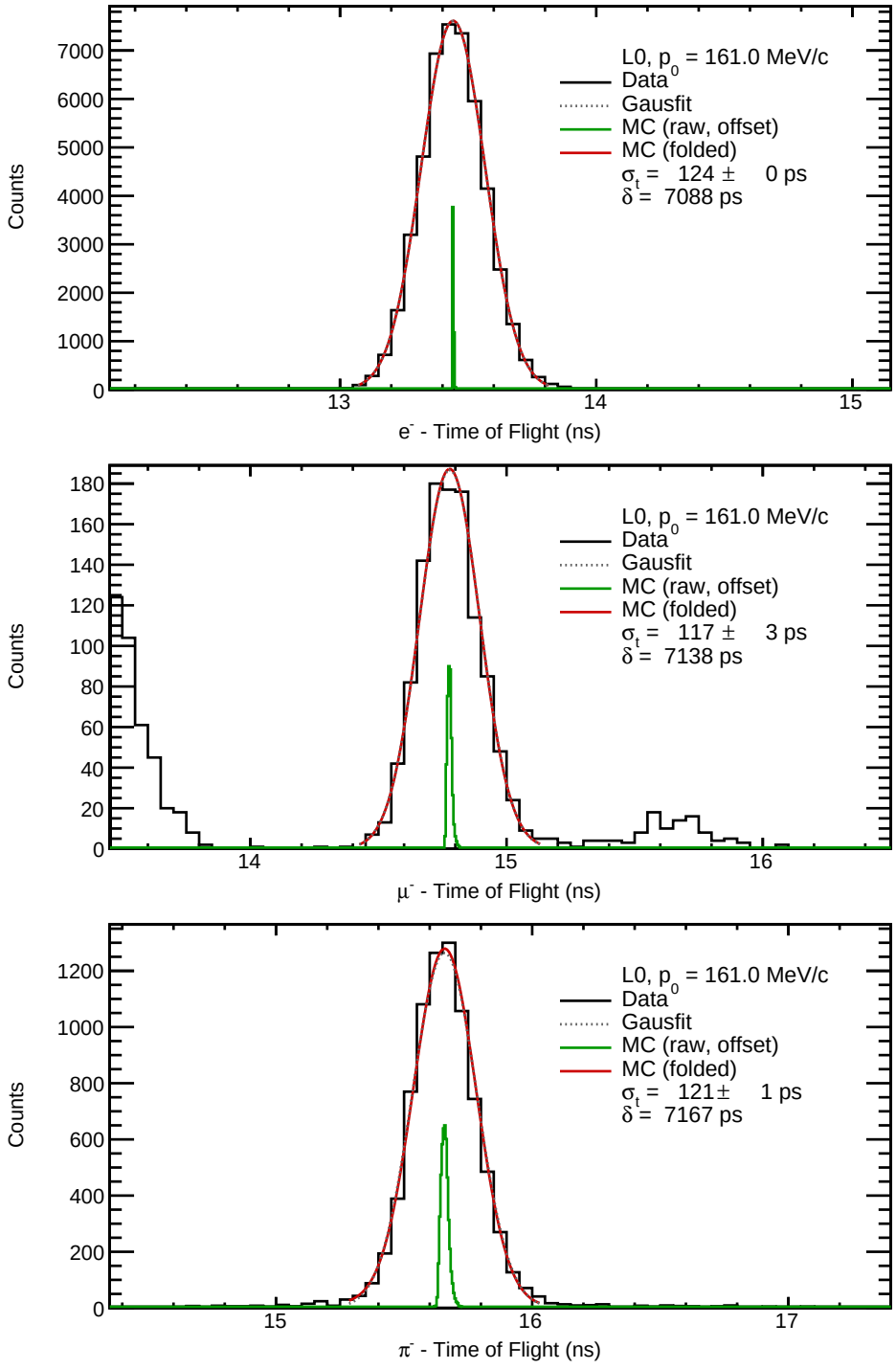

FIG. 54: Three example spectra of fitted electron, muon, and pion time-of-flight spectra from the beam-hodoscope, paddle C9, to the beam-monitor paddle one in the L_0 setting at the nominal channel-momentum of 161 MeV/c.

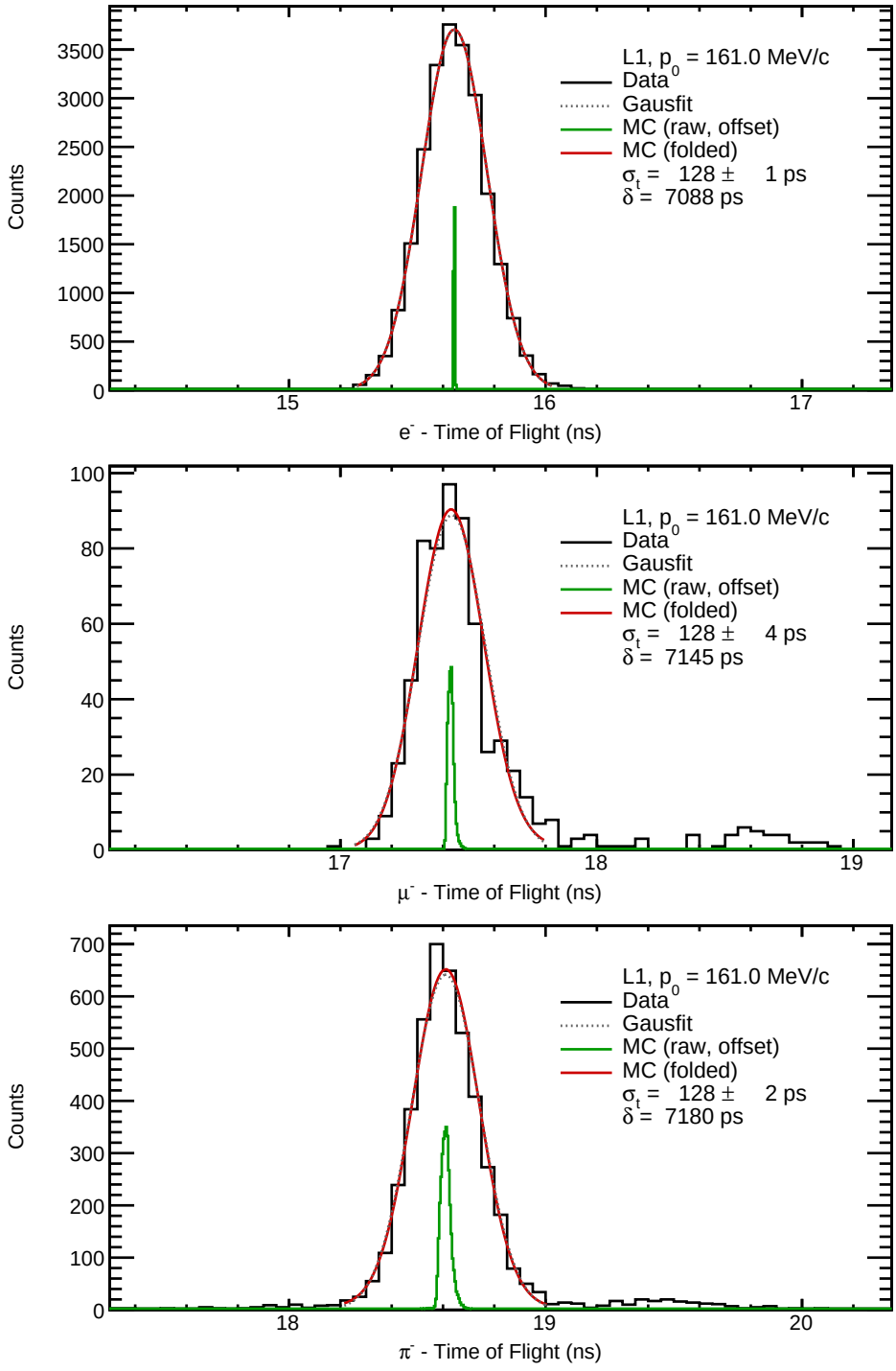

FIG. 55: Three example spectra of fitted electron, muon, and pion time-of-flight spectra from the beam-hodoscope, paddle C9, to the beam-monitor paddle one in the L_1 setting at the nominal channel-momentum of 161 MeV/c.

Overall, the fitted values of σ are approximately 125 ps. These values correspond to the experimental detector and readout-electronics time resolution. The goal of MUSE is a system-wide time resolution of less than 100 ps; an amount that has previously been achieved. The 2018 Summer test runs show a slightly poorer resolution. A direct comparison of the results for σ between the L_0 and L_1 settings shows an approximately 7 ps larger width for the L_1. This difference might be indicative of an additional and unresolved source of background in the L_1 setup that is not fully incorporated in the simulated data.

The fitted time shifts, δ, are approximately 7 ns. These shifts account mostly for cable and electronic delays. The values of δ^e for electrons in the L_0 and L_1 settings are equal, indicating that the path-length difference that is assumed in the simulation between these two settings, 660 mm, is well confirmed by the experimental data. In the L_0 setting, the time-shift values for muons, δ_0^μ, and pions, δ_0^π, are larger than δ_0^e, showing that the average particle speed in the experiment was less than in the simulation which assumed an initial 161 MeV/c momentum.

Figure 56 shows a summary of all fits to experimental time-of-flight spectra from the beam-hodoscope, paddle C9, to the beam-monitor paddle one for all detector positions L_0 through L_3. The colored histograms are the particle-type separated experimental data. As evident by the events underneath the electron peak, some of the data are plagued by random coincidences. The colored curves represent a total of twelve independent fits to all particle types in each setting.

Following Eqs. (7) and (9), experimental results of the initial momenta were determined from the time shift differences Δt_i for electrons, muons, and pions for each of the setups L_1, L_2, and L_3 relative to the L_0 setup. The statistical uncertainties from the fitted values δ and from the determination of the simulated values of ΔL^{sim}, β_i^{sim}, and ΔE^{sim} were propagated to find the statistical uncertainty of the momentum. The uncertainties of δ are the dominant contribution.

Results for a detailed analysis, following Eqs. (7) and (9), of the time-of-flight distributions of Fig. 56 are given in Table IV. Uncertainties include statistical uncertainties only. As expected, the longer flight-path differences give the most precise result for the momentum measurement. The channel momentum was set to 161 MeV/c. The actual particle momentum at the IFP, however, was slightly lower due to energy losses in the

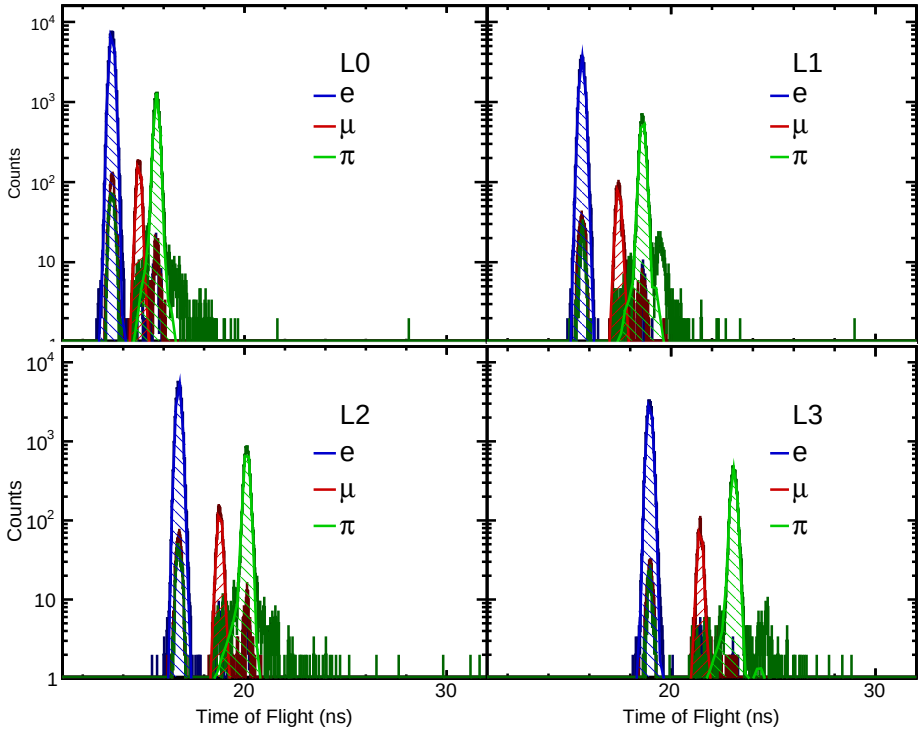

FIG. 56: Summary of all fits to experimental time-of-flight spectra from the beam-hodoscope, paddle C9, to the beam-monitor paddle one for all detector positions L_0 through L_3. The nominal channel-momentum was set to 161 MeV/c, negative polarity. See text for details.

GEM detector that was installed there; see Fig. 63. Our Geant4 simulation started at the beginning of the MUSE setup and did not include energy losses of particles upstream of the setup. Accounting for the different energy loss of the muons and pions in the GEM detector at the IFP gives momentum corrections of the order 0.57 MeV/c and 0.74 MeV/c for muons and pions. The resulting final particle momenta of 160.4 ± 0.4 MeV/c and 159.9 ± 0.1 MeV/c, respectively, are in excellent agreement. The statistical uncertainty for the pions is better than 0.1%, while the muon momentum is determined to 0.25% statistically, consistent with our goal.

TABLE IV: Results of the analysis of the time-of-flight distributions in Fig. 56 for a nominal channel momentum of 161 MeV/c. The actual particle momentum at the IFP, however, was slightly lower due to energy losses in the GEM detector that was installed there; see Fig. 63.

Setup	Δt_i^e (ps)	$c\Delta t_i^e$ (mm)	p_0^μ (MeV/c)	p_0^π (MeV/c)
ΔL_1	0.7 ± 1.0	0.2 ± 0.3	159.8 ± 1.3	159.6 ± 0.3
ΔL_2	-4.9 ± 0.9	-1.5 ± 0.3	160.1 ± 0.7	159.3 ± 0.2
ΔL_3	-9.6 ± 1.1	-2.9 ± 0.3	159.6 ± 0.5	159.2 ± 0.2
Average:			159.8 ± 0.4	159.2 ± 0.1
Average (incl. IFP energy-loss correction):			160.4 ± 0.4	159.9 ± 0.1

4. Results

a. Overview To date, we have analyzed over 400 time-of-flight data sets. The sets differ in channel-momentum setting, polarity, and detector combinations. As discussed earlier, the analysis of one set involves fitting electron, muon, and pion time-of-flight spectra for the four different detector setups L_0 through L_3. We have more data taken that we continue to analyze. An overview of the present status of the analysis is given in Table V. The table lists for the collimator position x_c and the selected relative momentum $(dp/p)_c$ the results for the difference between the extracted and assumed path-length difference between the L_1 and L_0 settings, $dL_1 = \Delta L_1^{\rm exp} - 660$ mm, and the weighted average of the muon and pion momenta extracted from the two configurations with the longest flight paths (L_2 and L_3). These values were further corrected for the energy loss of particles in the IFP. The final two columns give the relative momentum change with respect to the extracted value at the central collimator setting. All uncertainties are determined as the standard deviation of the derived values for the various detector combinations. Detector combinations with very poor statistics or failed fits were not included in the averages of Table V. On average, 15 combinations of beam-hodoscope paddles to beam-monitor bars contribute to the analysis of one setting.

The results can be summarized as follows:

- In the analyzed run sets, the relative standard deviations of the extracted pion momenta are of the order 0.1% to 0.3%. The sample includes all variations between

TABLE V: Preliminary summary of the results of the analysis of nine sets of Summer 2018 time-of-flight data for various channel momenta and polarity, p_0, as well as collimator positions, x_c. The extracted momenta p_μ and p_π have been corrected for energy losses in the GEM at the IFP (Sec. E).

#	x_c (mm)	$(dp/p)_c$	dL_1 (mm)	p_μ (MeV/c)	p_π (MeV/c)	$(dp/p)_\mu$	$(dp/p)_\pi$
				$p_0 = -117$ (MeV/c)			
1	−70	+1%	-3.14 ± 2.02	119.20 ± 0.33	119.11 ± 0.40	1.0%	0.9%
2	−35	+0.5%	-2.34 ± 1.40	117.92 ± 0.55	117.93 ± 0.36	−0.1%	−0.1%
3	0	0%	2.05 ± 2.01	118.00 ± 0.70	118.04 ± 0.44	0.0%	0.0%
4	35	−0.5%	-1.62 ± 4.01	117.17 ± 0.57	116.79 ± 0.29	−0.7%	−1.1%
				$p_0 = -161$ (MeV/c)			
5	−35	+0.5%	32.96 ± 1.17	169.35 ± 0.88	169.69 ± 0.37	5.7%	6.0%
6	0	0%	-1.96 ± 1.39	160.19 ± 0.70	160.13 ± 0.25	0.0%	0.0%
7	35	−0.5%	-7.99 ± 2.15	163.07 ± 0.72	163.09 ± 0.40	1.8%	1.9%
				$p_0 = +161$ (MeV/c)			
8	−35	+0.5%	2.94 ± 2.34	161.27 ± 0.57	161.68 ± 0.19	0.5%	0.6%
9	0	0%	0.34 ± 2.69	160.39 ± 0.54	160.66 ± 0.16	0.0%	0.0%
10	35	−0.5%	-4.84 ± 3.66	160.08 ± 0.45	159.77 ± 0.21	−0.2%	−0.6%

different detector combinations of a given set. Poorer statistics limited the muon-momentum precision, and the relative standard deviations are of the order 0.5% for muons.

- A direct comparison of the extracted muon and pion momenta shows a relative agreement of 0.3% or better. In half of the settings in Table V, the agreement is even better than 0.1%. These comparisons show that the needed precision for the momentum determination can be achieved.

- The expected change of average momentum with a change in the collimator setting is mostly seen in the extracted data. Comparing set 1 with set 3 gives the expected +1% momentum increase, and comparing set 4 with set 3 shows a change of about −0.5% within two standard deviations. Set 2 and 3 show the same average momentum, and we believe the collimator was not set properly. The momenta in set 8

are 0.5% higher, and the momenta in set 10 are about 0.5% lower than in set 8, as expected.

Unexplained is the unrealistically large deviations of the particle momenta in sets 5 and 7 compared to set 6. Although one set should have larger momenta and the other lower momenta compared to the central setting 6, both show momentum increases. The estimated path offsets are also unusually large for sets 5 and 7.

- The difference between the extracted and assumed path-length difference is typically of the order of 2 mm with a standard deviation of a few millimeters. The most notable exceptions are the sets 5 and 7.

b. Systematic uncertainties We have started to investigate possible systematic uncertainties in the final results.

- Assumed path length in the simulation. While the upstream and downstream positions of the beam hodoscope are controlled by the dowel pins of the sliding table to about 0.4 mm, the two positions of the beam monitor are less reproducible. Also, the absolute distance between the beam hodoscope in its downstream position to the beam monitor in its upstream position, L_0 has not yet been surveyed precisely. All these uncertainties, however, do not appreciably affect the precision of the momentum measurement.

  We have studied this effect with two simulations of a 117 MeV/c data set. In one simulation we assumed the standard detector positions with a difference between the upstream and downstream locations of the sliding table of 660 mm; in the other simulation we assumed in the reference setup L_0 that the beam hodoscope was positioned 50 mm too far upstream, i.e., an assumed 50 mm shorter path difference for ΔL_1, a value of 610 mm. Results of the analysis of the experimental data based on either of the two simulations are given in Table VI. The analysis reconstructed the correct path-length difference and obtained consistent muon and pion momenta for all three path-length differences. The effect of a wrongly assumed path length results primarily in errors in the energy-loss calculation as well as changes of the detector

TABLE VI: Results of the analysis of the experimental time-of-flight distributions for a nominal channel momentum of 117 MeV/c and flight path between beam hodoscope C8 and beam monitor bar 1 based on two different Geant4 simulations: one with the correctly assumed path-length difference of $\Delta L_1^{\rm sim} = 660$ mm and one where the path-length difference was assumed to be 50 mm too short.

Item	$\Delta L_1^{\rm sim} = 660$ mm	$\Delta L_1^{\rm sim} = 610$ mm
Electron time mismatch, Δt_1^e	0.6 ± 1.2 ps	168.0 ± 1.2 ps
Extracted path offset (L1)	0.2 ± 0.4 mm	50.4 ± 0.4 mm
Derived path-length difference, $\Delta L^{\rm exp}$	660.3 ± 0.4 mm	660.5 ± 0.4 mm
Muon time mismatch, Δt_1^μ	-12.0 ± 13.7 ps	216.3 ± 13.7 ps
Extracted muon momentum, p_1^μ	118.2 ± 1.1 MeV/c	118.2 ± 1.1 MeV/c
Muon time mismatch, Δt_2^μ	-3.8 ± 14.1 ps	224.3 ± 14.1 ps
Extracted muon momentum, p_2^μ	117.6 ± 0.8 MeV/c	117.6 ± 0.8 MeV/c
Muon time mismatch, Δt_3^μ	43.6 ± 16.0 ps	271.8 ± 16.0 ps
Extracted muon momentum, p_3^μ	117.3 ± 0.5 MeV/c	117.3 ± 0.5 MeV/c
Pion time mismatch, Δt_1^π	21.5 ± 13.3 ps	286.1 ± 13.3 ps
Extracted pion momentum, p_1^π	116.1 ± 0.7 MeV/c	116.3 ± 0.7 MeV/c
Pion time mismatch, Δt_2^π	17.7 ± 15.0 ps	284.9 ± 15.0 ps
Extracted pion momentum, p_2^π	116.7 ± 0.5 MeV/c	116.7 ± 0.5 MeV/c
Pion time mismatch, Δt_2^π	94.2 ± 17.8 ps	360.1 ± 18.0 ps
Extracted pion momentum, p_3^π	116.4 ± 0.4 MeV/c	116.5 ± 0.4 MeV/c

acceptance and opening angles of apertures. If offsets appear to be too large, the simulation can be redone in an iterative procedure with improved geometry.

- A wrongly calibrated TDC affects the time measurements. The path-length differences will be reconstructed wrongly, Eq. (2). Up to first order effects in the timing, $\alpha t + \beta$, do, however, cancel in the determination of the particle speeds β, Eq. (7). Nonlinearities will affect the speed determination. We have not seen such nonlinearities.

- Our method to determine the average particle speed $\beta_i^{\rm exp}$ makes use of the path-length differences $\Delta L_i^{\rm sim}$ and particle speeds $\beta_i^{\rm sim}$ in the simulation. These two

parameters need to be determined from simulated distributions and various ways to extract the parameters are possible. We have used, both the difference of the z positions of the detector and the mean value of the path-length distribution to estimate ΔL_i. We also have used two methods to estimated β_i^{sim}: the mean value of the speed distributions, and a Gaussian fit it. All these methods gave essentially identical results.

- At present, we see the biggest source of systematic uncertainties in any effect that changes the shape or position of the time-of-flight peak that has not been accounted for in the simulation. In the simulation, we have mostly used the standard beam parameterization that we adjusted to previous measurements of the beam properties. We have also used a beam parameterization that was extracted from data of the Summer 2018 measurements. The latter was not as well tuned as the previous one. As the beam tune frequently changed last summer and was not always perfectly optimized, we may have encountered more background in the data than is accounted for in the simulation. Also, some components of the setup were found to be slightly off their nominal position. Those changes in the geometry of the setup that have not yet been included in the simulation can also contribute to underproduced background.

5. Discussion

The Summer 2018 test measurements have shown that the setup is capable of determining muon and pion momenta with the required precision. However, we have also found in some of the analyzed datasets systematic deviations from the expected results that we have not yet been able to explain. We have learned:

- Combined results from various detector combinations achieve a high statistical precision. To investigate systematic effects, however, we would need enough statistics per data point. For a determination of the time-of-flight to about 1 ps with a system resolution of about 120 ps, we need at least $120^2 = 14,000$ events. We have not

achieved this statistics for muons and pions at 117 MeV/c and 161 MeV/c, and not for electrons and muons at 210 MeV.

- More surveyed and dowel-pin-controlled detector positions, including for the beam monitor, and possibly improved rigidity of the setup are needed for the study of systematic uncertainties and independent verification of the results for the extracted path-lengths.

- While the obtained system time resolution of ≈ 125 ps was not far off the design value of less than 100 ps, the best possible the time resolution is desirable.

- We have not made full use of the measured particle trajectories in this analysis. Also, some steering of the beam was needed to compensate for energy losses due to the GEM detector in the IFP. These ad-hoc adjustments were resulting in an angled beam. For the best possible momentum measurements the beam needs to be on axis, tight, and well focused.

- Linear mis-calibrations of the TDC cancel in the analysis of the muon and pion momentum. Those mis-calibrations, however, will impact the path-length determination and, therefore, an important checkpoint for systematic effects. An independent calibration of the TDC will help constrain sources of systematic errors.

B. Beam distribution measurements

In August 2018, a series of measurements were taken in parallel with the TOF studies to characterize the use of the PiM1 magnetic channel as a spectrometer. We placed four GEM planes in the target region, where the additional fourth plane was intended for GEM detector development studies. The GEM detectors covered a $10\,\text{cm} \times 10\,\text{cm}$ area in the target region of PiM1 and provided high quality tracks for MUSE. The position resolution was of the order of $150\,\mu\text{m}$, which met our systematic requirements for tracking as outlined in the Technical Design Report. We were also able to use our Beam Hodoscope (BH) detector and the HIPA RF signal to identify particle types on an event-by-event basis and construct particle-species-separated track ensembles. In order to have a relatively

high flux of each particle type, a large portion of our data was taken at a momentum of +161 MeV/c. Also included in the set-up were a jaw before ASM11 and a collimator near the IFP. Additionally, we prepared two movable GEM detectors to be placed at the IFP for certain sets of measurements. The IFP-GEMs provided initial particle tracks before the final channel bending magnet, ASM12. These GEMs also allowed for a direct measurement of the matrix elements between the IFP and target region for comparison to simulation. With this experimental set-up, we performed the following types of measurements:

1. Quadrupoles between IFP and the PiM1 target ON, with and without the two GEM planes at the IFP. Data were taken for e, μ and π at various central momenta.

2. Quadrupoles between IFP and the PiM1 target OFF, with and without the two GEM planes at the IFP. Data were taken for e, μ and π at various central momenta.

The measurements with the quadrupoles ON or OFF allowed us to study the influence of focusing effects of the quadrupoles on the bending of the particles at the ASM12 dipole, and the beam distribution at the target. Section III B 1 addresses this. The motivation behind taking data with and without GEMs at the IFP was to study energy loss due to the GEM material, and compare its effects on momenta and beam sizes at the PiM1 target with a simple Geant4 simulation of the GEMs. This comparison is presented in Section III B 2 for all three particle types. Next, we move on to a comparison of our experimental results with g4beamline simulations and TURTLE simulations of the entire PiM1 channel in Sections III B 3 and III B 4, respectively. Note that all results in this section are presented in transport coordinates: in the PiM1 area +z is along the beamline, +x is to beam right, and +y is vertically downward.

1. Beam distributions at target with quadrupoles ON or OFF

Here we present a comparison of the centroids of our particle distributions at the target position with the last 6 quadrupoles ON or OFF. The results are shown in Table VII and VIII. All quoted uncertainties are statistical only. We know that a systematic uncertainty exists from a warping of the distributions caused by inefficiencies in the GEMs but

we do not have an estimate for this effect. Experimental GEM distributions can be seen in Figure 58.

IFP GEMs In	Quads On Centroid Position (mm)	Quads off Centroid Position (mm)
e	3.7 ± 0.11	11.2 ± 0.10
μ	1.9 ± 0.27	0.9 ± 0.24
π	0.4 ± 0.09	-8.8 ± 0.16

TABLE VII: Particle ensemble centroid positions with quadrupoles on and off and the IFP GEM planes installed, for a central momentum of +161 MeV/c

IFP GEMs Out	Quads On Centroid Position (mm)	Quads off Centroid Position (mm)
e	1.9 ± 0.09	8.7 ± 0.14
μ	0.6 ± 0.30	1.2 ± 0.45
π	0.4 ± 0.09	-0.2 ± 0.12

TABLE VIII: Particle ensemble centroid positions with quadrupoles on and off and the IFP GEM planes removed, for a central momentum of +161 MeV/c

Comparing Table VII with VIII, we see that the centroid position values at the PiM1 target are shifted significantly when the IFP GEMs are in place. This is caused by momentum loss of the beam as it interacts with the GEM material. Furthermore, it is interesting to see that there is a 1 cm deviation in the centroid positions from one particle type to the next, when the IFP GEMs are in place and the quads are turned off.

2. Momentum loss due to IFP-GEMs: Geant4 simulation versus data

Geant4 simulations of only two GEM planes, an extended region of air with plastic vacuum windows at the IFP and beam were performed to study how energy losses in the windows, air and GEMs at the IFP affect the electrons, muons and pions in the beam. These simulations were run both with and without GEM planes at the IFP. The simulations used a pencil beam with no dispersion to approximate the PiM1 beam at the

IFP. For completeness, the simulations were also run with a momentum bite of ± 0.5% around the central momentum for a more realistic description of our beamline set-up, but this was found to have an effect on the order of less than 10^{-3} on the mean momentum loss. Appendix E shows the initial particle momentum going into the IFP region in red and the particle momentum as it leaves the IFP as a distribution in black. To present the results in a more human-readable format we compile the results into Table IX showing the initial momentum and the mean final momentum after passing through the IFP material and GEM planes. Similarly, we list the momentum loss of particles traversing the IFP region without the GEMs in Table X.

P Loss due to IFP GEMs	117 MeV/c	161 MeV/c	210 MeV/c
e	116.51(0.4%)	160.47(0.3%)	209.44(0.3%)
μ	116.22(0.6%)	160.43(0.4%)	209.51(0.2%)
π	115.85(1%)	160.26(0.5%)	209.42(0.3%)

TABLE IX: A Geant4 simulation to study momentum loss for all 3 particle species and all 3 MUSE momenta due to GEMs at the IFP. The values in parenthesis indicate the percent of the central momentum that is lost.

P Loss due to IFP Material	117 MeV/c	161 MeV/c	210 MeV/c
e	116.741(0.22%)	160.728(0.16%)	209.717(0.13%)
μ	116.599(0.34%)	160.705(0.18%)	209.746(0.12%)
π	116.408(0.51%)	160.617(0.24%)	209.701(0.14%)

TABLE X: A Geant4 simulation to study momentum loss for all 3 particle species and all 3 MUSE momenta due to air and magnet windows at the IFP. The values in parenthesis indicate the percent of the central momentum that is lost.

Since the central bend angle of the ASM12 dipole magnet is 75°, a 1% change in momentum corresponds to a shift in the bend angle through the dipole of 0.75°. This shift, when combined with the 7.5 m lever arm between the ASM12 dipole and the target, yields a position change of 10 cm. Our simple estimate here is consistent with the simulations

presented in Section II D, that 1-cm offsets in position distributions at the target between different particle types correspond to roughly 0.1% momentum differences. We note that from our simulation, in particular the 117 MeV/c column of Table IX, we expect a maximum relative shift of 4 cm between particles at any momentum, and for 161 MeV/c in particular we expect a shift of no larger than 1 cm between particle types. We also note that the simulation indicates that the 2 GEM planes roughly double the momentum loss at the IFP compared to the loss induced by air and the windows.

We now compare Geant4 results with experimental results. We focus on our experimental data taken when the quadrupoles were turned off. In addition to comparing the energy loss in simulation with data, we want to determine the variation in the bending of the different particle types through the ASM12 dipole after they interact with material at the IFP. For our results, we compare relative differences between particle types at a single momentum setting. As an arbitrary choice, we compare all differences to the values, position and momentum, given by the μ's. Usually in our kinematics the e's lose less momentum than the μ's so that they are at $+x$ or beam right, of the μ's, while π's lose more momentum and appear at $-x$ or beam left of the μ's. We see that this is the case for 161 MeV/c and the simulation and experiment agree. For 210 MeV/c the simulation predicts that e's lose more momentum than the μ's and our data reflects this.

As can be seen in Table XI, our simulation recreates the expected differences in particle distribution to within 0.003% when GEMs are placed at the IFP position for 161 MeV/c. We can also see agreement between simulation and experiment on the order of 0.05% when GEMs are not placed at the IFP. As an additional check we performed both a simulation and measurement of momentum loss for a central momentum of 210 MeV/c with IFP GEMs in place. We again see agreement between simulation and experiment on the order of 0.05%. Again the uncertainties are purely statistical in nature. We have do not have a firm number for the experimental systematic uncertainties.

Beam Momentum	GEM Position	Particle Type	δx at target			Momentum Difference Relative to μ (%)	
			Mea. (mm)	Relative to μ (mm)			
			Abs.	Rel.	Sim.	Mea.	Sim.
161	In	e	11.2 ± 0.10	10.3 ± 0.26	10	0.103%	0.1%
		μ	0.9 ± 0.24	-	-	-	-
		π	-8.8 ± 0.16	-9.7 ± 0.29	-10	-0.097%	-0.1%
	Out	e	8.7 ± 0.14	7.5 ± 0.47	2	0.075%	0.02%
		μ	1.2 ± 0.45	-	-	-	-
		π	-0.2 ± 0.12	-1.4 ± 0.46	-6	-0.01%	-0.06%
210	In	e	-14.7 ± 0.13	-9.9 ± 0.37	-10	-0.099%	-0.1%
		μ	-4.8 ± 0.35	-	-	-	-
		π	-19.1 ± 0.10	-14.3 ± 0.36	-10	-0.143%	-0.1%

TABLE XI: Comparison between experimental data and Geant4 simulation for 161 MeV/c and 210 MeV/c. We compare experiment and simulation if the IFP GEMs are in place or removed, and we separate out each particle type. We show the measured absolute position of the particle distributions at the PiM1 target and the relative difference between each particle type and the μ distribution. We compare our measured values to simulation for both the relative position and momentum, using the assumption that a 1% difference in momentum corresponds to a 10 cm shift in position at the target. For 161 MeV/c the e and π distributions appear on opposite sides of the μ distribution, however this is not the case for 210 MeV/c, which is in agreement with simulation.

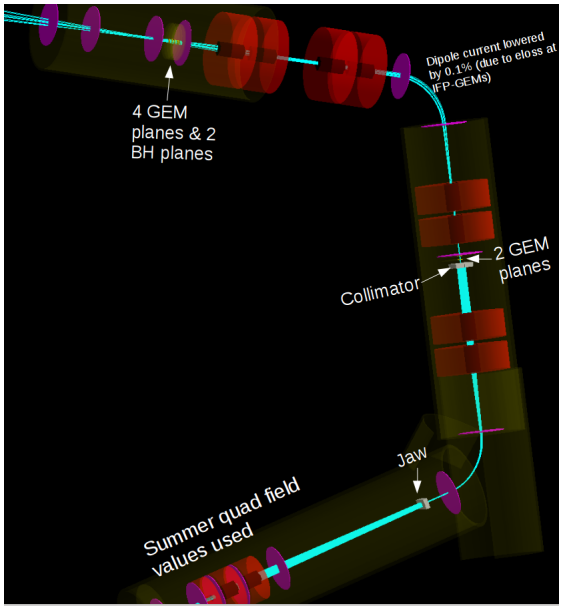

FIG. 57: A visualization in g4beamline simulation of 5000 μ^+ sample events from a point source which is shown in Fig. 36. Only μ^+ parent particles are propagated. The picture shows the jaw, collimator, GEM planes and beam hodoscope planes that were added to the simulation to match the experimental set-up.

The previous section demonstrated that Geant4 simulations of just the material at the IFP give results that are consistent with data. Now, we transition to a simulation of the entire beamline using the g4beamline simulation software. We updated the g4beamline default simulation presented in Section II E to match it with the actual beamline set-up, including matching the material type to account for energy loss and multiple scattering. We also added shields around the GEM detectors and beam hodoscope planes to be consistent with the cuts applied in the analysis of the summer data, in which only those tracks were considered that were detected by the GEM and beam hodoscope detectors. Figure 57 shows a visualization of the updated beamline. The details are given below:

1. We added a jaw consisting of two vertical copper blocks and two horizontal copper blocks at 6.678 m distance from the production target. We matched the aperture

size to what was used during data taking (±1.07 cm in x and y). Each block is 10 cm long along the beam direction.

2. We added a collimator made of copper blocks at the IFP. We set the slit opening to ±0.5 cm along the x direction. Each copper block is 20 cm wide along x, 40 cm high along y and 10 cm long along the beamline.

3. We added two GEM planes after the collimator. The first plane is 8 cm away from the downstream end of the collimator. The second GEM plane is 8 cm away from the first GEM plane. The active material is made of Mylar, Aluminum, Kapton, Copper layers and GEM gas (70 % Argon, 30% CO_2). We placed a shield around each GEM plane to kill particles that did not hit the active material of the GEM detector. This is consistent with the cuts applied to the data.

4. We replaced the virtual detector at the beam hodoscope location with two beam hodoscope planes, each made of vinyltoluene plastic. Each plane is 2 mm thick and 10 cm diameter. The spacing between the two planes is 2 cm. We placed a shield around each GEM plane to kill particles that did not hit the active material of the GEM detector, consistent with data analysis.

5. We added four GEM planes near the PiM1 target location, with 6.5 cm space between each GEM plane. The first GEM plane is placed 2 cm downstream of the second beam hodoscope plane. The fourth GEM plane is placed 35 cm upstream of the target location.

6. We updated the fields of the quadrupoles to summer 2018 settings. We also flipped the polarities of QSL17 and QSL18, consistent with the experimental settings.

7. We lowered the dipole current of the second dipole by 0.1% because the particles lost energy when they interacted with the GEM material at the IFP.

Here we compare preliminary g4beamline results and experimental results for the beam distributions at the IFP and the PiM1 target for a 161 MeV μ^+ beam. The input beam source used in the simulation is a point beam source shown in Fig 36. Fig 58 shows

the spatial and angle distributions at the IFP. Only those events are shown which are detected by the two GEM detectors at the IFP, the two beam hodoscope planes and the four GEMs at PiM1 target, in g4beamline as well as the data. In each distribution, we scaled the simulation by a constant factor given by (peak height in data/peak height in simulation). Both simulation and measured distributions show that the beam spot is very narrow at the IFP, due to the collimator. There is a reasonable agreement between the simulation and experimental measurements. We see a dip in the y distribution near $y = 0$ in the experimental measurement, but not in the simulation. This is because there are dead GEM strips at that location which have not been taken into account in the simulation. Another source of discrepancy could be attributed to the fact that the fringe fields of the dipoles are not yet taken into account in the simulation.

Fig 59 shows the spatial and angle distributions of the beam at the PiM1 target, after removing events that were not detected by any of the six GEM planes or the two beam hodoscope planes. Again, we see a qualitative agreement between g4beamline and measured distributions. We believe that the level of agreement can be improved further by improving the dipole field maps in the simulations, and resolving at least some of the issues with the data analysis which are discussed in introduction of Section III.

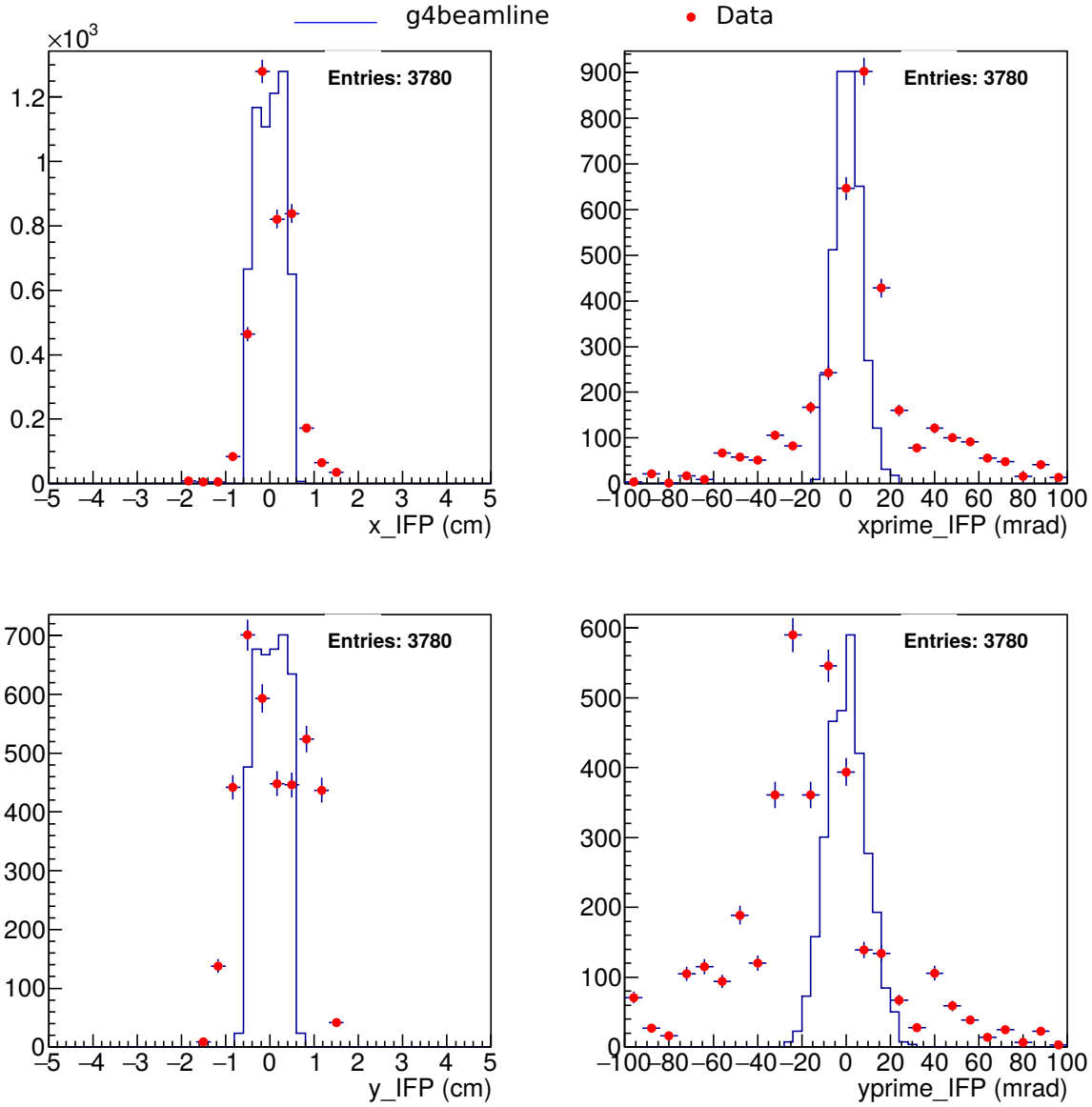

FIG. 58: A comparison of beam distributions, at the IFP, between g4beamline simulation and experimental measurements. Only μ^+ parent particles are propagated. Central momentum is 161 MeV. The simulation plots are scaled by a constant factor given by (peak height in data/peak height in simulation). ***Upper Right***: x' distribution. ***Upper Right***: x' distribution. ***Lower Left***: y distribution. ***Lower Right***: y' distribution.

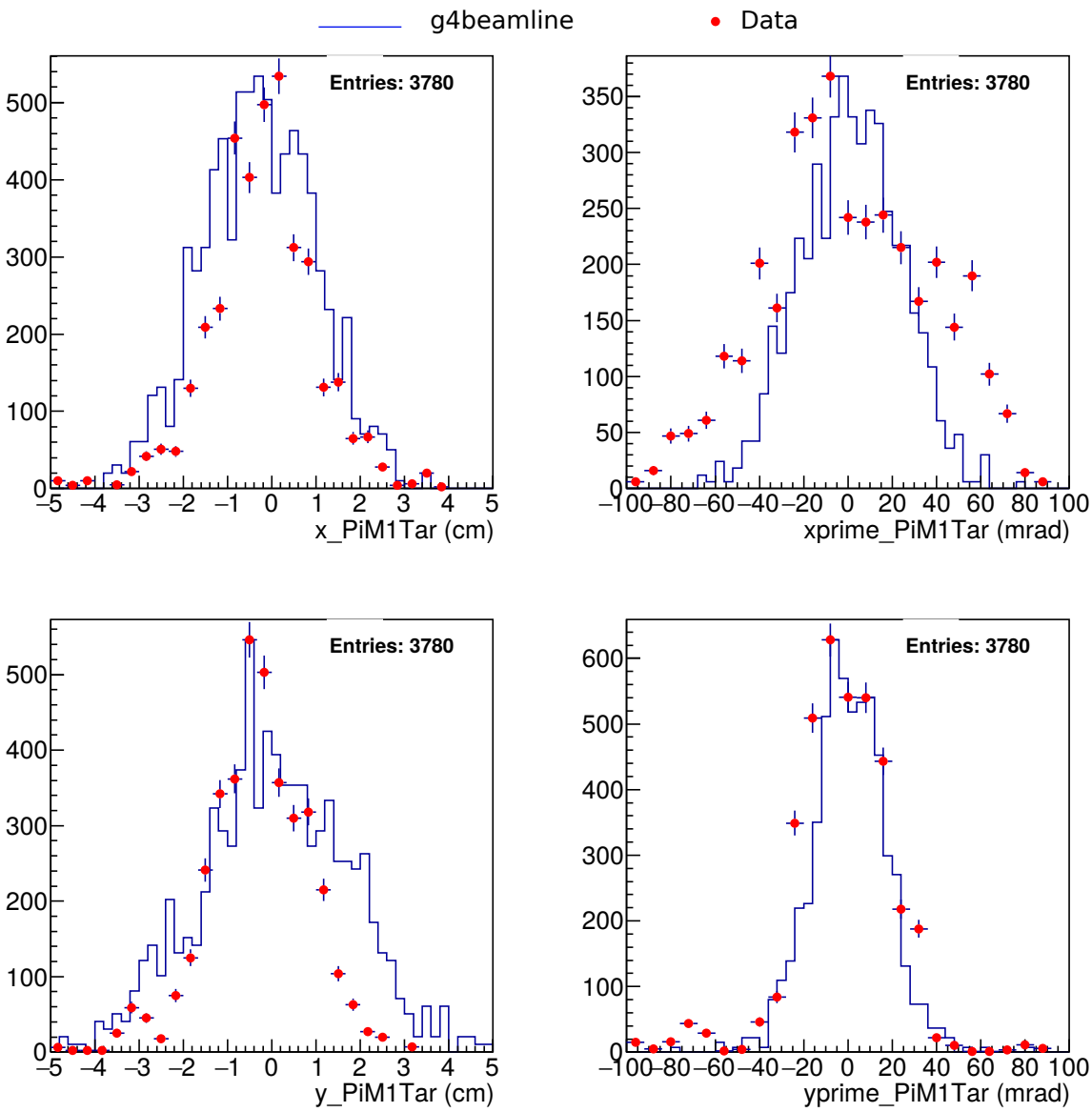

FIG. 59: A comparison of beam distributions, at the PiM1 target, between g4beamline simulation and experimental measurements. Only μ^+ parent particles are propagated. Central momentum is 161 MeV. The simulation plots are scaled by a constant factor given by (peak height in data/peak height in simulation). ***Upper Left***: x distribution. ***Upper Right***: x' distribution. ***Lower Left***: y distribution. ***Lower Right***: y' distribution.

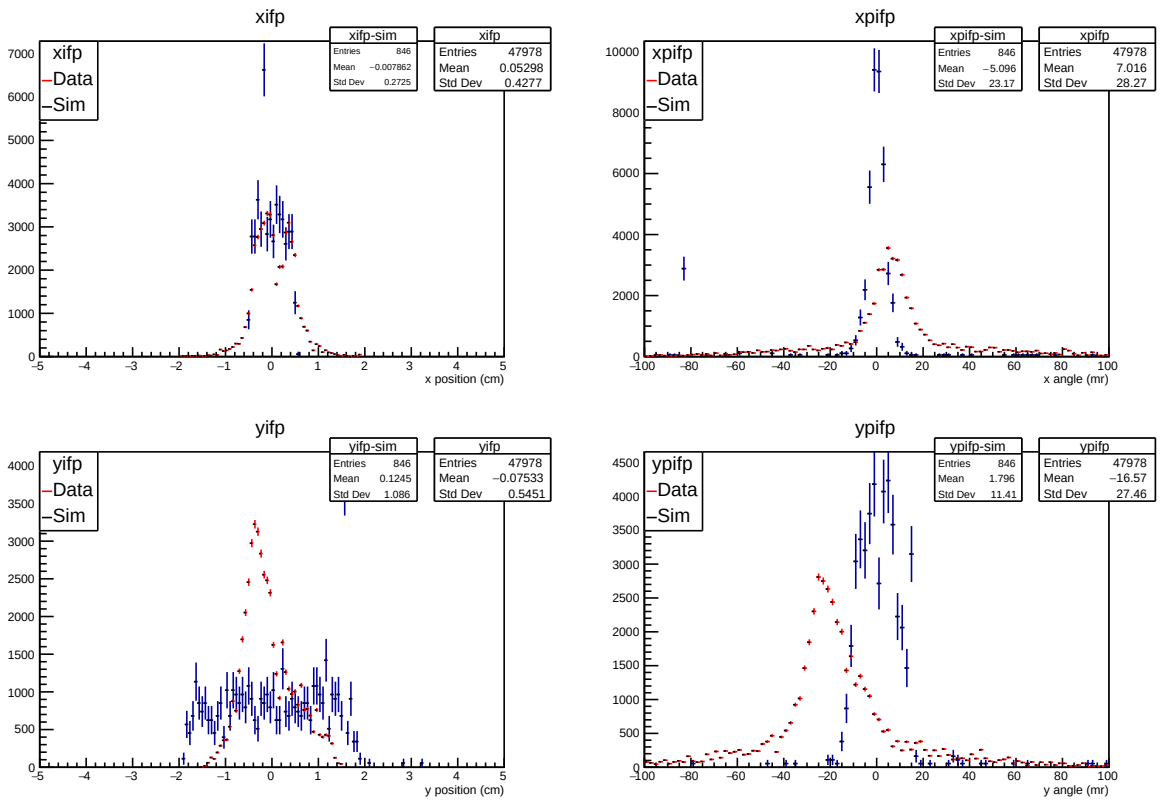

FIG. 60: A comparison between TURTLE and experimental data at the IFP

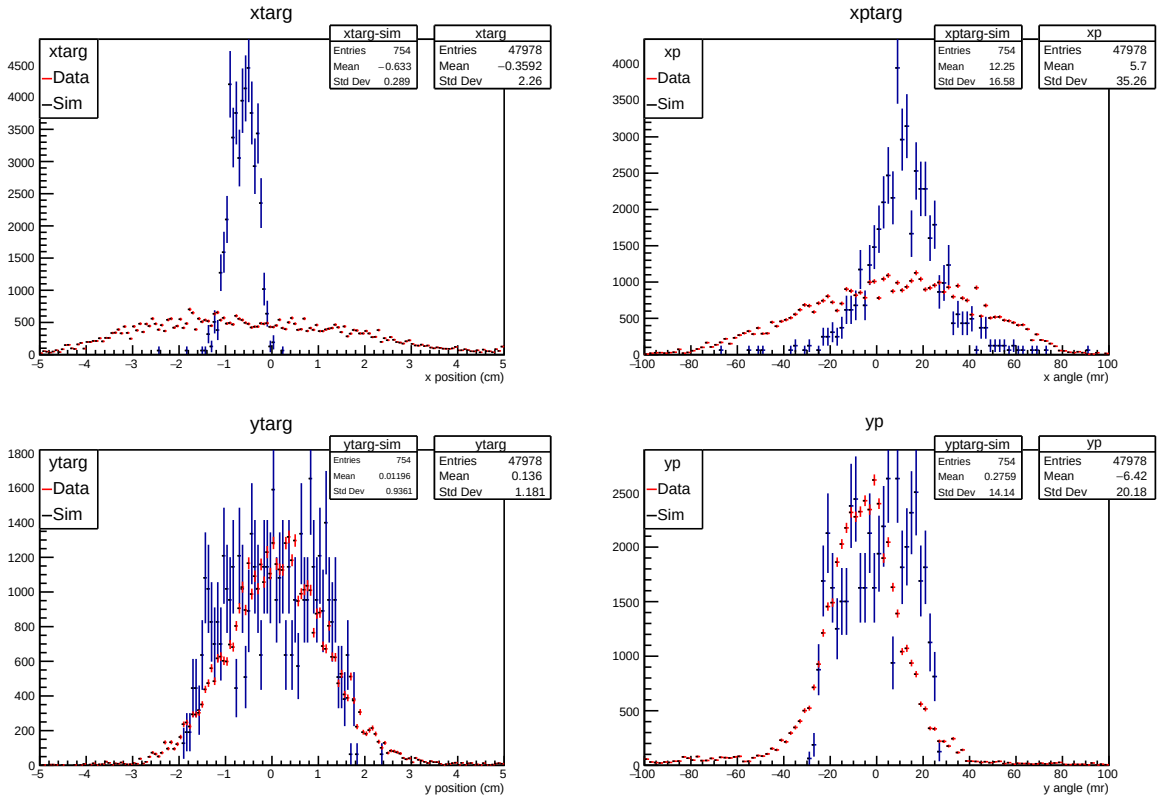

FIG. 61: A comparison between TURTLE and experimental data at the PiM1 Target

The TURTLE simulation inputs were modified in the same way as the g4beamline inputs to simulate the 2018 data. We adjusted the default simulation to use quadrupole fields as set, and added in FS11 jaws, the narrow collimator, and a thin carbon slab to mimic the multiple scattering caused by the GEMs at the IFP.

The resulting simulation at the IFP is shown in Fig. 60. The x distributions, which are constrained by the slot, and the x' distributions agree reasonably well in shape. The y distribution is too wide in the simulation, indicating a smaller effective source size in the data or apertures in the beamline that are not in the simulation. The y' distribution is about the right size, but the data are not centered. We note that the GEM chambers at the IFP were placed by hand, not surveyed, and their alignment relative to the beam is not certain. Also, since there were only 2 GEM chambers at the IFP, and there were some inefficiencies seen, the experimental distributions are somewhat modified from reality.

The resulting simulation at the target is shown in Fig. 61. The x and x' distributions are wider in the data than in the simulation, even though the distributions at the IFP match reasonably well. From the dispersion discussion and the experimental setup, this could arise because the momentum distributions at the IFP are broader than the simulation predicts, or because the simulation does not accurately reproduce the momentum and multiple scattering spread of the beam going through the GEMs. The y and y' distribution are moderately close to the data, so the multiple scattering effects of the GEMs are probably reasonably accounted for.

To conclude, TURTLE provides a reasonable qualitative description of the measured data, which perhaps would be improved if energy loss in material were better modeled. We expect G4beamline is more refined in its treatment of material effects, and the better description of the x and x' distributions at the target confirm this. It also appears that the beamline has apertures that limit the source size in y more than we currently have modeled, but this difference might also be do in part to the GEM performance.

5. Conclusion

We have demonstrated that we can experimentally measure differences in the distributions of e, μ, and π in the PiM1 beamline. These data compared with simple estimates or matrix elements from TURTLE suggest that particles from the channel have very similar average momentum, with differences no more than of order 0.1%. The differences can be described by a simple Geant4 simulation of material at the IFP to within 0.05% of the position of the distribution by momentum and energy loss mechanisms that arise from particles passing through the entrance and exit windows, along with air, at the IFP region. This good agreement between simulation and experiment, for several experimental configurations and two momenta, allows us to conclude that particles traversing the PiM1 beamline bend uniformly through the ASM12 dipole, and have momenta that are consistent and can be determined relatively within the experimental requirements of 0.2 - 0.3%, complementing the TOF technique and adding a determination for electrons as well. With such a precise measure of the momentum we are well suited to perform the

MUSE experiment and achieve our stated accuracy within the limits of our systematic uncertainty.

Furthermore, we have shown that beam distributions at the IFP and the PiM1 target location measured in the summer 2018 data are in reasonable agreement with the TURTLE and G4beamline simulations. It appears that the better treatment of energy loss in G4beamline leads to better agreement with target x and x' distributions than we get with TURTLE. These results indicate that we have a fairly good understanding of the beamline and our data. Further improvements are expected as we fine-tune the dipole field maps and improve the data analysis procedures.

We also note that both G4beamline and TURTLE are in fair agreement with each other when comparing production source size and IFP and PiM1 target distribution sizes. The good agreement of the simulations with each other and the data gives confidence that the electron beam is small and the properties of electron and pion beams are consistent with each other.

IV. ERROR BUDGETS

In this section we discuss the uncertainties for the MUSE beam momentum measurement.

The requirements from the TDR were summarized in Appendix A. A 0.2 - 0.3% measurement of the average momentum will give the desired 0.1% cross section systematic uncertainty from the knowledge of momentum. If we were to simply use the average momentum instead of the full momentum distribution in the analysis, it would lead to an effect several times smaller.

TOF measurements described in Section III A have been demonstrated to achieve the required 0.2 - 0.3% uncertainty in momentum, for π's and μ's. The pion determination is typically 2 - 3 times better statistically due to the larger number of pions in the beam. The analyses done in all cases yield muon and pion average momenta that are consistent within uncertainties. The analysis found some outliers however, with the extracted path length providing an indication of issues in the measurement, but as yet no clear understanding of what the problem is. The uncertainties are statistical; we are actively exploring pos-

sible systematic uncertainties. The main potential issue identified to date is unidentified backgrounds under the TOF peaks, shifting their positions; the nature of this problem makes it hard to quantify. Now that we have used the production TOF system for the first time, we recognized and described several issues and consequent improvements that we are undertaking.

The dispersion measurements summarized in Section III B 5 appear to be fully capable of 0.1% relative momentum measurements, since 0.1% momentum differences, for particles from the same point at the IFP, lead to of order cm shifts in the target position, which are easily observed. We do not at this point claim better than a 1-cm determination, since, although no difference was observed in the distribution of particles at the IFP, we do not consider the measurement at the IFP with the somewhat inefficient 2-GEM telescope to be adequate to make strong claims. We used simulations to account for interactions with material in the IFP region, which generated small differences between the distributions of different particle types at the target, Because the pions and electrons both are generated from small sources, systematic uncertainties from modeling the beam line are reduced, as compared to muons which have an extended source. But the consistency of the distributions measured indicates that the modeling systematic is small. Also recall that the IFP and target distributions are reasonably well modeled by both G4beamline and TURTLE.

The value of the TOF technique is that absolute momenta can be determined, while the value of the dispersion measurement is that its uncertainties do not increase with momentum and electron (relative) momenta can be determined. The combination of the two provides redundancy. The ultimate limiting systematics for the two techniques in our setup are not yet clear.

V. SUMMARY

This report seeks to answer the questions posed by the PSI BVR committee on the understanding of the PiM1 beam line, and the resulting beam properties. As a result of the studies contained herein, the MUSE collaboration is confident that we can determine

the momentum settings of e, π, and μ in the PiM1 beamline with the necessary 0.3% accuracy. Here we summarize the answers to the specific questions posed.

a. ***Modelling of the source distributions for different particle types, to ensure that the small differences observed between beam properties of pions, muons, and electrons are consistent with expectations.*** In section II B we review the simulations performed in ROOT and Geant4 to analyse the initial source distributions and find that the electron / positron and pion source distributions appear to be small, and that the muon source is somewhat larger (approximately 1 cm) as expected. The channel properties should be therefore essentially identical for $e^{\pm}$ and π, giving very simmilar beam spots, aside from minor differences due to multiple scattering and energy loss, as observed in our test data presented at the BVR. Thus the simulations produce results consistent with our observed beam properties.

b. ***Clarification of the discrepancies presented between the G4beamline vs. TURTLE simulations of the PiM1 beam line.*** As demonstrated in II E, and preceeding sections, the collaboration has invested substantial time and effort in improving both the G4beamline and TURTLE simulations, and bringing their input parameters into alignment, both with each other and with the known and observed beam line properties. This effort has come to fruition with TURTLE and G4beamline producing results that agree with each other to first order. Remaining minor differences are attributable to the magnet fringe fields which are included in TURTLE, but not yet incorporated in G4beamline. However, over all the level of agreement gives great confidence that we can understand the propogation of the beam through the system to the experimental area.

c. ***Discussion of the properties of the beam line employed as a spectrometer.*** In section II D we present TURTLE simulations pertaining to using the beamline as a spectrometer and results of such measurements taken in summer 2018 are presented in Sec. III B 5. These results demonatrate that this is a feasible mechanism for determining the comparison between the momenta of the various particle species.

d. ***A description of beam properties measurements taken, and presentation of an error budget associated with the critical electron/muon momentum measurements.*** There have been many beam properties measurements made throughout the test beam times. Major results include demonstration of the feasibiliity of the beamline

as a spectrometer technique (Sec. III B 5), measurement of beam distributions and comparison with beam simulations (Sec. III B 5), comparison of energy losses measured and anticipated (Sec. III B 5), and the demonstration of the use of time of flight to determine pion and muon momenta to the necessary level of precision (Sec. III A). An error budget for these measurements is presented in IV. Alongside analyses of the data, these sections present improvements which will be made to practises and procedures in order to further improve the outcome of such measurements. However, even in their current commissioning form, before we have had the opportunity to fully perfect all calibrations and fully survey all detector positions with the final accuracy, they conclusively demonstrate their feasibility to achieve the required accuracy.

e. ***Conclusion.*** In the course of this report, we have examined and determined the properties of the PiM1 beam from source to target area using multiple simulation methods, and through many test measurements. In most cases, the results from various simulation packages accord with eachother, and the data. Where discrepancies exist, they are explained and a method to remedy the issue for the final experimental analysis is presented, where appropriate. On the basis of the forgoing, we conclude with confidence that we can determine and understand the beam properties of the PiM1 beamline with sufficient accuracy to successfully perform the MUSE experiment.

Appendix A: Beam Momentum Systematic Goal

We recapitulate here the considerations presented in the MUSE Technical Design Report (TDR) [9] that lead to a goal of determining the beam momentum at the level of 0.2 - 0.3%.

Figure 1 on page 6 of the TDR shows how the cross sections are changed if the radius is 0.84 vs. 0.88 fm. There is a 6% change in the cross sections over the Q^2 range of the MUSE experiment. A 5σ determination of the radius difference then corresponds to knowing how much the cross sections decrease to an uncertainty of 1.2%.

Our goal in the experiment is to keep as many of the systematic uncertainties as possible several times smaller than this, preferably at the level of 0.1% on the cross sections, so that they are nearly negligible in the final result, not appreciably affecting the total uncertainty. The goal is also because, almost invariably, some systematic uncertainties end up larger than planned. Note that the absolute uncertainty is not the concern, since absolute cross sections will not be sufficiently precise to be used without normalization. We are instead concerned with how the systematics change the slope of the cross sections with Q^2.

Figure 55 on page 97 of the TDR shows how the cross sections are changed when the momentum of a monochromatic beam is changed. Over the angle range of the experiment, 20° - 100°, a 0.1% change in the momentum changes the overall cross sections by about 0.15%, but only changes the relative cross sections at 20° vs. 100° by about 0.01 - 0.05% depending on momentum. The effect is slightly more (but still within this range) for electrons than for muons. Thus the 0.1% goal on the relative cross sections translates into a ≈0.2 - 0.4% or so requirement on the beam momentum.

Figure 55 also shows that for a uniform 3% wide momentum distribution, simply using the average momentum instead of the full momentum range in calculating the cross sections changes the result by a negligible amount, 0.02% or less.

Figure 48 on page 82 of the TDR reproduces the full momentum distribution estimate of Figure 55 for a more realistic incident muon momentum distribution, calculated with Geant to take into account detector and target energy-loss effects. The effect explored in Figure 55, the difference between using a full momentum distribution vs. the average momentum, increases to 0.03% or less, which remains negligible.

To conclude, a 0.2% average beam momentum determination will limit the systematic uncertainty on the cross section slope to about 0.1%, which is more or less negligible compared to the 1.2% uncertainty goal. The effect is smaller in most of the kinematics, so a 0.3% beam momentum determination is in our view adequate. We plan to determine the momentum distribution[3] as input in determining a more precise result, but the experiment is insensitive to this. Even if the average momentum is used instead of the full beam momentum spectrum, the effects of the averaging are very small, well below 0.1%.

Appendix B: Subcommittee Report

We include here the sucommittee report from the BV49 meeting that was sent to the MUSE collaboration.

MUSE Subcommittee Report BVR49

The scientific interest in the proton radius puzzle remains high, though the scientific landscape has become less clear. A recently published spectroscopic result on electronic Hydrogen based on the 2s-4s transition favors the muon Hydrogen result, while another, yet unpublished measurement based upon the 1s-3s transition disagrees with the muonic result and appears in line with the previous world average on electronic spectroscopy and the electron scattering data. It is clear that while more work in the atomic physics arena is needed, a compelling, and timely, muon scattering experiment such as MUSE would be of very great value. MUSE is particularly attractive in that it can compare muon and electron data in a way that compensates some, but not all, systematic effects. The committee believes that the scientific case for MUSE remains compelling.

The MUSE collaboration is to be congratulated for making very significant progress toward the realization of a complete experimental apparatus. The collaboration is approaching the point at which all subsystems meet design specifications. The remaining challenges largely concern the assembly and integration of all components and installation on the beamline.

Progress on the liquid hydrogen target is particularly notable. The collaboration has met

[3] The most straightforward way to determine the momentum distribution is to measure the flux of the different particle species into PiM1 as a function of the collimator position, as the collimator is scanned across the acceptance, correcting for any variation of the primary proton beam current. Collimator edge scattering essentially cancels since the momentum range is small and x' varies little. TOF measurements only determine the average momentum, while beam spot shape measurements are not well enough simulated at present to be a reliable measurement.

essentially all of the hardware milestones presented at BRV48. The successfully cool down using Ne is a very major accomplishment and the fact that initial reports suggest a rather short cool down time that is consistent with calculations indicates that target is well understood and approaching operational readiness. The collaboration is to be commended for the productive coordination with PSI operational staff concerning safety and other operational issues.

Very significant progress on all detector systems have been made. Of particular note is the continuing progress in the reduction of electronic noise. Noise reduction is always a tedious process in a new setup and MUSE has carried out a long and diligent effort in the simplification and optimization of cabling and connectors for the GEM detectors. Noise levels in the GEM detectors now appear to be at an acceptable level. Similarly, the troublesome noise and pickup problems with the straw tube trackers seems to have been addressed with the use of new cards which may obviate the need for extensive and potentially cumbersome RF shielding.

The fabrication plan for the straw tubes has changed with the intention to carry out final assembly of the tubes on site at PSI to avoid damage during shipping. The current schedule calls for the completion of ˜1000 tubes by May 2018. This appears to be a very aggressive goal but the collaboration appears comfortable with this schedule. Since the committee was not given detailed information concerning production rates, etc., we can only wish them well.

Following the discussion at BVR48, the overall mechanical design of the apparatus has been modified to allow graceful removal from the beamline. The design allows the removal of the entire MUSE apparatus, intact, from the beamline. This appears to be a sound approach that will allow minimal interference between experiments. Estimates of the time required to insert/remove the entire apparatus were somewhat uncertain but are expected to be on the order of 1-2 weeks. One naturally expects this transition time to become shorter with experience. The committee was pleased to learn that the collaboration is working closely with the PSI survey and alignment group to ensure that suitable fiducials are incorporated into the design to permit proper alignment among the MUSE components as well as between the experimental apparatus and the beamline.

As noted above, one of the attractive features of the MUSE project is the fact that the experiment is capable of precision measurement of the scattering of both electrons and muons and is therefore capable of directly determining if electrons and muons probe the proton in the same fashion. Of course, for such a comparison to be valid, it is incumbent on the experiment to clearly establish that all systematic effects are well understood. In particular, those aspects that are asymmetric between electrons and muon must be fully understood and clearly described. Among these asymmetries are physics effects, such as QED corrections that

ultimately limit the sensitivity of direct comparison between muon and electron scattering. But others represent instrumental effects in which electrons and muon are treating differently.

A particularly notable difference lies in the way in which the overall electron and muon momenta will be determined to the required precision of 0.2-0.3%. Muon and pion momenta can be determined by time-of-flight. The electron momenta have to be calibrated by a novel method using the beam-line as a spectrometer. While initial measurements demonstrating this technique have been presented, the committee does not believe that the MUSE collaboration has presented a sufficient understanding of the beamline to justify the claim that systematic effects, including those entering the critical momentum measurement, are sufficiently well understood. The beam has been studies by G4beamline and Turtle simulation, where the former models the different source distribution of particle species in the production target, while the later simply calculates the trajectories of an assumed initial distribution. The statement presented to the committee was that the two simulations strongly disagree, with the cause of the disagreement not yet identified.

Before approving the allocation of significant production beam time, the committee recommends that the MUSE collaboration prepare a detailed report that discusses all relevant issues related to the beam line simulations. This report should include, but not necessarily be limited to clarification of G4beamline vs. Turtle discrepancies, discussion of the properties of the beamline employed as a spectrometer, and a description of the measurements taken and presentation of the error budget associated with the critical electron/muon momentum measurements.

In particular, we are interested in potential differences in the source distributions between the different particle species at the production target. These might cause differences in the phase space distribution of particles propagating down the beam line and ultimately bias the momentum determination. The measurement presented indicated only small differences between beam properties of pions, muons and electrons. This is good news for the experiment.

Nevertheless, we want to be assured that these findings are consistent with expectations from some basic modelling of the source distributions.

The committee recognizes the difficulty associated with the fact that detailed field maps of the upstream beam line are not available. However, we believe, that the basic elements available (simulation of source distribution and transport through an idealized beamline) should be sufficient to obtain a realistic uncertainty estimate. It is absolutely incumbent on the collaboration to clearly demonstrate that the

beamline is sufficiently well understood that potential systematic effects are sufficiently under control to allow a credible measurement.

Upon completion of this report, the review committee further recommends that it be reviewed by an external committee with the requisite expertise to assess that the understanding of the beamline is indeed sufficient. The allocation of future, substantive beam time will be contingent on the completion of this review.

Appendix C: TURTLE Input Deck

We use TURTLE-DECAY, but for this study we only consider parent particles. Our standard TURTLE input deck for a nearly point-like muon beam being transported by PiM1 follows. Parentheses and slashes serve to define comments. Each line begins with a code indicating what the line is defining:

- 1: defines the beam
- 3: defines drifts through a field-free region
- 4: defines bending magnets,
- 5: defines quadrupole magnets,
- 6: defines slits,
- 7: defines shifts of the beam center (used, e.g., for asymmetric slits),
- 9: defines a repeating region of code, and
- 16: defines various calculation parameters.

Details of the definitions can be found in the TURTLE manual, however there are multiple versions of the manual due to the extensive history of TURTLE. PSI maintains online descriptions not available in many manuals, which are available on its internal network through http://pc102.psi.ch. We have suppressed histogram definitions for brevity.

```
/MUSE 155MeVc parent muons/
(Number of Particles)
 1000000
(Aperture Constraints)
13. 10. ;
13. 110. ;
(Units Changes from Default)
15. 11. /MeVc/ 0.001 ;
15. 12.0 /MeV/ 0.001 ;
(Take homogeneous beam distribution instead of gaussian)
16. 20. ;
(Seed for random generator fixed for each run at the same value)
16. 30. 5. ;
(Parent Particle Mass)
(16. 3. 1. /e/ ;)
16. 3. 105.66 /Mu/ ;
(16. 3. 139.57 /Pi/ ;)
(Switch on Multiple Scattering - 165 = MS on, 166 = MS off = default)
16. 165. /mult/ ;
(16. 166. /mult/ ;)
(Beam Definition)
1. 0.1 30.0 0.1 80.0 0.0 1.5 155. /BEAM/ ;
(Switch on Second Order)
17. /SECO/ ;
(Design Momentum)
16. 11. 155. /P0_2/ ;
(Drift: distance between Production-Target-M and QTA11)
6. 1. 16. 3. 16. ;
3. 0.958 ;
6. 1. 16. 3. 16. ;
(QTA11)
16. 101. 7.5 ;
2. 1000. ;
5. 0.324 -0.9854 7.5 /QTA1/ ;
2. 1000. ;
```

```
(Drift)
6. 1. 16. 3. 16. ;
3. 0.131 ;
6. 1. 16. 3. 16. ;
(QTB11)
16. 101. 11.5 ;
2. 1000. ;
5. 0.475 -1.0894 11.5 /QTB1/ ;
2. 1000. ;
(Drift)
6. 1. 16. 3. 16. ;
3. 0.110 ;
6. 1. 16. 3. 16. ;
(QTB12)
16. 101. 11.5 ;
2. 1000. ;
5. 0.475 1.1965 11.5 /QTB2/ ;
2. 1000. ;
(Drifts)
6. 1. 16. 3. 16. ;
3. 0.176 ;
6. 1. 16. 3. 16. ;
3. 1.0 ;
6. 1. 16. 3. 16. ;
3. 1.0 ;
6. 1. 16. 3. 16. ;
3. 1.0 ;
6. 1. 16. 3. 16. ;
3. 1.0 ;
6. 1. 16. 3. 16. ;
(FS11 slits, in x then y. Estimate)
9. 100. ;
  6. 1.0 8. ;
  1. 14.266 12.30 5.0 0.730 980.2 0.622 2.921 0.0 /Cu/ ;
  3. .001 ;
```

```
9. 0. ;
9. 100. ;
  6. 3.0 8. ;
  1. 14.266 12.30 5.0 0.730 980.2 0.622 2.921 0.0 /Cu/ ;
  3. .001 ;
9. 0. ;
(3. 0.334 /DR5/ ;)
(Drift)
6. 1. 16. 3. 16. ;
3. 0.653 ;
6. 1. 16. 3. 16. ;
(ASM11)
6. 3. 5. ;
16. 5.0 6.0 ;
16. 7.0 0.45 ;
16. 8.0 2.8 ;
16. 12.0 0.55 /R11/ ;
16. 13.0 -0.8 /R12/ ;
2. 27.9 /WE11/ ;
4. 0.77539 4.3641 0.0 /ASM1/ ;
6. 3. 3.6 ;
4. 0.77539 4.3641 0.0 /ASM1/ ;
2. 27.9 /WE12/ ;
6. 3. 5. ;
(Drift to KSD11)
6. 1. 16. 3. 16. ;
3. 0.818 ;
6. 1. 16. 3. 16. ;
(Drift to QSL11)
6. 1. 16. 3. 16. ;
3. 0.539 ;
6. 1. 16. 3. 16. ;
(QSL11)
16. 101. 12. ;
2. 1000. ;
```

```
5. 0.59 -1.2731 12.0 /QSL1/ ;
2. 1000. ;
3. 0.112 ;
(QSL12)
16. 101. 12. ;
2. 1000. ;
5. 0.59 0.9086 12.0 /QSL2/ ;
2. 1000. ;
(Drift to DR8)
6. 1. 16. 3. 16. ;
3. 1.018 /DR8/ ;
(3. 0.689 /DR8/ ;)
6. 1. 16. 3. 16. ;
(Horizontal Beam Shift in cm before the slit - to model IFP collimator)
(7. -3.0 0.0 0.0 0.0 0.0 0.0 ;)
(Slit is open)
9. 100. ;
  6. 1.0 10. ;
  1. 14.266 12.30 5.0 0.730 980.2 0.622 2.921 0.0 /Cu/ ;
  3. .001 ;
 9. 0. ;
(Shift Beam back after slit)
(7. 3.0 0.0 0.0 0.0 0.0 0.0 ;)
(Carbon Absorber)
(16. 160. ;)
(9. 5. ;)
(  6. 50.0 50.0 ;)
  (1. 3.564 9.70 49.62 0.660 525.95 0.053 0.241 0.0 /C_Pi/ ;)
  (1  3.277 9.54 49.62 0.660 525.95 0.046 0.217 0.0 /C_Mu/ ;)
(  3. .001 ;)
( 9. 0. ;)
(16. 161 ;)
(Dump Distribution to FOR070.DAT file)
(16. 181.0 70.0 0. ;)
(Drifts)
```

```
6. 1. 16. 3. 16. ;
3. 0.412 ;
6. 1. 16. 3. 16. ;
(QLS13)
16. 101. 12. ;
2. 1000. ;
5. 0.59 0.9086 12.0 /QSL3/ ;
2. 1000. ;
(Drift)
6. 1. 16. 3. 16. ;
3. 0.112 ;
6. 1. 16. 3. 16. ;
(QSL14)
16. 101. 12. ;
2. 1000. ;
5. 0.59 -1.2732 12.0 /QSL4/ ;
2. 1000. ;
(Drift)
6. 1. 16. 3. 16. ;
3. 1.311 ;
6. 1. 16. 3. 16. ;
(ASM12)
6. 3. 5.0 ;
16. 5.0 6.0 ;
16. 7.0 0.45 ;
16. 8.0 2.8 ;
16. 12.0 -0.8 /R21/ ;
16. 13.0 0.55 /R22/ ;
2. 27.9 /WE21/ ;
4. 0.77539 4.3641 0.0 /ASM2/ ;
6. 3. 3.6 ;
4. 0.77539 4.3641 0.0 /ASM2/ ;
2. 27.9 /WE22/ ;
6. 3. 5. ;
(Drift)
```

```
6. 1. 16. 3. 16. ;
3. 0.684 ;
6. 1. 16. 3. 16. ;
(QSL15)
16. 101. 12. ;
2. 1000. ;
5. 0.59 0.5440 12.0 /QSL5/ ;
2. 1000. ;
(Drift)
6. 1. 16. 3. 16. ;
3. 0.112 ;
6. 1. 16. 3. 16. ;
(QSL16)
16. 101. 12. ;
2. 1000. ;
5. 0.59 -0.7506 12.0 /QSL6/ ;
2. 1000. ;
(Drifts)
6. 1. 16. 3. 16. ;
3. 1.038 /DR16/ ;
6. 1. 16. 3. 16. ;
(QSL17)
16. 101. 12. ;
2. 1000. ;
5. 0.59 0.9086 12.0 /QSL7/ ;
2. 1000. ;
(Drift)
6. 1. 16. 3. 16. ;
3. 0.163 ;
6. 1. 16. 3. 16. ;
(QSL18)
16. 101. 12. ;
2. 1000. ;
5. 0.59 -1.2732 12.0 /QSL8/ ;
2. 1000. ;
```

```
(Drift)
6. 1. 16. 3. 16. ;
3. 1.536 /TARG/ ;
(Drift)
3. 2.0 ;
SENTINEL
SENTINEL
```

Appendix D: G4beamline Input File

Here we provide the input file for the g4beamline simulation, which we created to compare this simulation with TURTLE. In this study, we only considered parent particles. The beam source is a nearly point-like muon beam with 155 MeV central momentum. The parameters of the beam source are read-in from an ASCII file called g4_in.txt. We have added comments to assist in understanding the code. They begin with a # sign. Note that we have introduced line breaks in some of the commands shown below so that they fit within the page. These line-breaks must be removed before compiling the code, otherwise it will fail to compile without errors. A detailed description of a typical input file is discussed in **Section** 4 of the G4beamline User's Guide (http://muonsinc.com/muons3/g4beamline/G4beamlineUsersGuide.pdf).

```
##########################################################################################
#   History:
#
#   Original author: L. Desorgher
#   Revised to match Turtle input deck the P Reimer (PER)
#   Revised to match Turtle by Priya, Univ. of Michigan (PRoy)
#   Dipole Fieldmaps revised to match ASM11 and ASM12 to Turtle (PER)

##########################################################################################

param -unset firstEvent=1
param -unset nEvents=100000
```

```
param -unset lastEvent=100000
param -unset beamPart=mu+

##### Define channel momentum
param -unset pChannel=155

##### Allow the user to specify a different momentum
param -unset pOffset=1.0

##### For beamline momentum other than 155, we scale current in the magnets
param scale=$pChannel/155

param -unset map1=ASM1.g4blmap
param -unset map2=ASM2.g4blmap

##### Add ability to scale magnets sets
param -unset scaleDipole=1.000295
param -unset scaleQSL=1
param -unset scaleQT=1

##### Define output file name and type
param sepChar="_"
param file=MuSEBeam_$beamPart$sepChar$pChannel$sepChar$pOffset
param histoFile=$file.root

##### Overwelming reccomendation was qgsp_bert_hp for physics engine
param -unset physicsName=QGSP_BERT_HP
physics $physicsName

param partName=$beamPart
param tuneP=abs($pChannel)
param -unset beamAngle=22.5
param zProdTarget=-958
param startZ=$zProdTarget
```

```
##### convert kG/mm to T/m
param kGpmm_to_Tpm=100

##### Quad iron shield parameters
param RIRON=800
param killInPipe=0
param pipeColor=0,1,1,0.4
param killInIron=1
param ironColor=1,0,0,0.4
param absorbAllColor=1,1,0,0.05
param killAllColor=$absorbAllColor
param -unset killInShield=1
param shieldColor=$killAllColor
particlecolor e+=1,1,1 e-=1,1,1 mu+=0,1,1 mu-=0,1,1

##### Track cuts to keep only mu+
trackcuts keep=mu+

collective
param worldMaterial=Vacuum
param maxstep=10 deltaChord=0.5
start x=0. y=0. z=0. initialZ=$startZ

##### Adjust centerline to 22 degrees
cornerarc z=$zProdTarget angle=$beamAngle centerRadius=10

##### Read-in the beam source from ASCII file
beam ASCII file=g4_in.txt

##### Define virtual detector plane
param MuSEDetColor=1,0,1,1
param MuSEDetLength=15
param MuSEDetRadius=500
virtualdetector MuSEDet radius=$MuSEDetRadius length=$MuSEDetLength color=$MuSEDetColor
```

```
##### Define QSL quadrupole magnets with rounded + aperture
param LQSL=590
param RQSL=120
genericquad QSL fieldLength=$LQSL coilHalfWidth=50 coilRadius=150 poleTipRadius=125
ironRadius=$RIRON ironLength=$LQSL kill=$killInIron ironColor=$ironColor
##### Remove the line-break between poleTipRadius and ironRadius before compiling

##### Define shielding tube
tubs SHIELD innerRadius=$RIRON*1.1 outerRadius=$RIRON*1.2 kill=$killInShield
color=$shieldColor
##### Remove the line-break between kill and color before compiling

##### Read-in field for dipoles
fieldmap ASM1 file=$map1
fieldmap ASM2 file=$map2

######################
#  Beam elements
######################

place SHIELD z=$startZ-100 length=10 innerRadius=0 outerRadius=$RIRON*1.1
rename=SheildStart
##### Remove the line-break between outerRadius and rename before compiling

##### Place virtual detector at Production Target location
place MuSEDet z=$startZ+$MuSEDetLength rename=Det0

##### Place virtual detector at start of quad QTA11
place MuSEDet z=-$MuSEDetLength rename=Det0a

##### Define QTA11 parameters
param LDRIFT1=0
param PDRIFT1=$LDRIFT1/2

##### Length magnet in mm
```

```
param LQTA1=324

##### Radius aperture in mm
param RQTA1=75.0

##### QTA11 defocuses mu+ in X. So, gradient should be negative
param BQTA1=-0.9854*$scale*$scaleQT
param GradQTA1=$BQTA1/$RQTA1*$kGpmm_to_Tpm

##### Define QTA11 quadrupole magnet
param RIRON=500
genericquad QTA11 fieldLength=$LQTA1 apertureRadius=$RQTA1 gradient=$GradQTA1
ironRadius=$RIRON ironLength=$LQTA1 kill=$killInIron ironColor=$ironColor
##### Remove the line-break between gradient and ironRadius before compiling

##### Place QTA11 at 162 mm wrt. ProdTarget @ -958 mm. 162+958 mm = 1120 mm
param PQTA1=$LDRIFT1+0.5*$LQTA1
place QTA11 z=$PQTA1

##### Place virtual detector between QTA11 and QTB11
param LDRIFT2=131
place MuSEDet z=$PQTA1+0.5*$LQTA1+0.5*$LDRIFT2+0.5*$MuSEDetLength rename=DetAQTA1

##### Define QTB11 parameters
param LDRIFT2=131
param PDRIFT21=$PQTA1+0.5*$LQTA1+0.5*$LDRIFT2
param LQTB=475
param RQTB=115.0

##### Define field gradient for QTB1. It defocuses mu+ in X
param BQTB1=-1.0894*$scale*$scaleQT
param GradQTB1=$BQTB1/$RQTB*$kGpmm_to_Tpm

##### Define QTB11 quadrupole magnet
genericquad QTB11 gradient=$GradQTB1 fieldLength=$LQTB coilHalfWidth=50 coilRadius=150
```

```
poleTipRadius=125 ironRadius=$RIRON ironLength=$LQTB kill=$killInIron ironColor=$ironColor
##### Remove the line-break between coilRadius and poleTipRadius before compiling

##### Place QTB11 at 692.5 mm wrt. ProdTarget @ -958 mm. 692.5+958 mm = 1650.5 mm
param PQTB1=$PDRIFT21+0.5*$LDRIFT2+0.5*$LQTB
place QTB11 z=$PQTB1

##### Place virtual detector between QTB11 and QTB12
param LDRIFT20=110
place MuSEDet z=$PQTB1+0.5*$LQTB+0.5*$LDRIFT20+0.5*$MuSEDetLength rename=DetAQTB1

##### Define QTB12 parameters
param LDRIFT20=110
param PDRIFT22=$PQTB1+0.5*$LQTB+0.5*$LDRIFT20

##### Define field gradient for QTB12. It focuses mu+ in X
param BQTB2=1.1965*$scale*$scaleQT
param GradBQTB2=$BQTB2/$RQTB*$kGpmm_to_Tpm

##### Define QTB12 quadrupole magnet
genericquad QTB12 gradient=$GradBQTB2 fieldLength=$LQTB coilHalfWidth=50 coilRadius=150
poleTipRadius=125 ironRadius=$RIRON ironLength=$LQTB kill=$killInIron ironColor=$ironColor
##### Remove the line-break between coilRadius and poleTipRadius before compiling

##### Place QTB12 at 1277.5 mm wrt ProdTarget at -958 mm. 1277.5 + 958 mm = 2235.5 mm
param PQTB2=$PDRIFT22+0.5*$LDRIFT20+0.5*$LQTB
place QTB12 z=$PQTB2

##### Place virtual detector after QTB12, close to its end
place MuSEDet z=$PQTB2+0.5*$LQTB+0.5*$MuSEDetLength+500 rename=DetAQTB2

param LDRIFT3=3586
param PDRIFT3=$PQTB2+0.5*$LQTB+0.5*$LDRIFT3
param LDRIFT4=1334
param PDRIFT4=$PDRIFT3+0.5*$LDRIFT3+0.5*$LDRIFT4
```

```
place SHIELD rename=SHEILD_A z=$PDRIFT4/2-250 length=$PDRIFT4+2500

##### Place virtual detector before start of dipole ASM11
place MuSEDet z=6384.0-10-0.5*$MuSEDetLength-2 rename=Det1

#*****************************************************************
# Change beam angle to 75 deg and place next set of beam elements
#*****************************************************************

##### Define bending radius, arc, angle parameters
param ASMAngleDeg=75.
param ASMAngleRad=$ASMAngleDeg*pi/180.
param L_center_line_ASM=2.*775.39-20
param ASMRadius=$L_center_line_ASM/$ASMAngleRad

##### Place cornerarc to bend the beamline
cornerarc z=$PDRIFT4+0.5*$LDRIFT4 angle=$ASMAngleDeg/2. centerRadius=$ASMRadius
radiusCut=$ASMRadius-160
##### Remove the line-break between centerRadius and radiusCut before compiling

param PASM1=$PDRIFT4+0.5*$LDRIFT4+0.5*$L_center_line_ASM
place SHIELD length=950 z=$PASM1 innerRadius=3*$RIRON outerRadius=3.1*$RIRON
initialPhi=-60 finalPhi=60
##### Remove the line-break between outerRadius and initialPhi before compiling

##### Define ASM11 dipole current and place the dipole
### The map is set to 1Tesla so current/intensity gives strength of dipole in Tesla
param BASM1=-0.591271616286*155.0/210.0*$scale*$scaleDipole
place ASM1 z=$PASM1 current=$BASM1
cornerarc z=$PASM1 angle=$ASMAngleDeg/2. centerRadius=$ASMRadius
radiusCut=$ASMRadius-160
##### Remove the line-break between centerRadius and radiusCut before compiling

place SHIELD rename=sheild_bend z=$PDRIFT4+$L_center_line_ASM length=4000
```

```
innerRadius=2.0*$RIRON outerRadius=2.1*$RIRON initialPhi=65 finalPhi=295
##### Remove the line-break between length and innerRadius before compiling

param LDRIFT5=1357
param PDRIFT5=$PASM1+0.5*$L_center_line_ASM+0.5*$LDRIFT5
param beginCenter=$PASM1+0.5*$L_center_line_ASM

##### Place virtual detector after ASM11, close to its end
place MuSEDet z=6384.01+$L_center_line_ASM+10+0.5*$MuSEDetLength+100 rename=Det2

##### Define QSL11 parameters
param BQSL11=-1.2731*$scale*$scaleQSL
param GradBQSL11=$BQSL11/$RQSL*$kGpmm_to_Tpm

##### Place QSL11 at 9586.8 mm wrt ProdTarget @ -958 mm. 9586.8+958 mm=10544.8 mm
param PQSL11=$PDRIFT5+0.5*$LDRIFT5+0.5*$LQSL
place QSL rename=QSL11 gradient=$GradBQSL11 z=$PQSL11

##### Define QSL12 parameters
param LDRIFT6=112
param PDRIFT6=$PQSL11+0.5*$LQSL+0.5*$LDRIFT6
param BQSL12=0.9086*$scale*$scaleQSL
param GradBQSL12=$BQSL12/$RQSL*$kGpmm_to_Tpm

##### Place QSL12 at 10288 mm wrt ProdTarget @ -958 mm. 10288+958mm=11246 mm
param PQSL12=$PDRIFT6+0.5*$LDRIFT6+0.5*$LQSL
place QSL rename=QSL12 gradient=$GradBQSL12 z=$PQSL12

param LDRIFT7=1018-0.5*$MuSEDetLength
param PDRIFT7=$PQSL12+0.5*$LQSL+0.5*$LDRIFT7

##### Place virtual detector at IFP i.e. 11650 mm wrt. ProdTarget @ -958 mm.
place MuSEDet z=11650 rename=Det3

##### Define QSL13 parameters
```

```
param LDRIFT8=512
param PDRIFT8=$PDRIFT7+0.5*$MuSEDetLength+0.5*$LDRIFT7
param BQSL13=0.9086*$scale*$scaleQSL
param GradBQSL13=$BQSL13/$RQSL*$kGpmm_to_Tpm

##### Place QSL13 at 12408 mm wrt ProdTarget @ -958 mm. 12408+958mm=13366 mm
param PQSL13=$PDRIFT8+$LDRIFT8+0.5*$LQSL
place QSL rename=QSL13 gradient=$GradBQSL13 z=$PQSL13



##### Define QSL14 parameters
param LDRIFT9=112
param PDRIFT9=$PQSL13+0.5*$LQSL+0.5*$LDRIFT9
param BQSL14=-1.2732*$scale*$scaleQSL
param GradBQSL14=$BQSL14/$RQSL*$kGpmm_to_Tpm

##### Place QSL14 at 13110 mm wrt. ProdTarget @ -958 mm. 13110+958 mm=14068 mm
param PQSL14=$PDRIFT9+0.5*$LDRIFT9+0.5*$LQSL
place QSL rename=QSL14 gradient=$GradBQSL14 z=$PQSL14

param LDRIFT10=1311
param PDRIFT10=$PQSL14+0.5*$LQSL+0.5*$LDRIFT10

##### Place virtual detector at start of dipole ASM1
param PASM2=$PDRIFT10+0.5*$LDRIFT10+0.5*$L_center_line_ASM
place MuSEDet z=$PASM2-775.39-10-0.5*$MuSEDetLength-2 rename=Det4

#*********************************************************************
# Change beam angle and place next set of beam elements
#*********************************************************************
param endCenter=$PDRIFT10+0.5*$LDRIFT10

place SHIELD rename=SHIELD_B z=($endCenter+$beginCenter)/2.0
length=$endCenter-$beginCenter
##### Remove the line-break between z and length before compiling
```

```
##### Place cornerarc to bend the beamline
cornerarc z=$PDRIFT10+0.5*$LDRIFT10 angle=$ASMAngleDeg/2.
centerRadius=$ASMRadius radiusCut=$ASMRadius-160
##### Remove the line-break between angle and centerRadius before compiling

##### Place dipole magnet ASM12
### The map is set to 1T so current/intensity gives strength of dipole in T
param BASM2=-0.591271616286*155.0/210.0*$scale*$scaleDipole
place ASM2 z=$PASM2 current=$BASM2
cornerarc z=$PASM2 angle=$ASMAngleDeg/2. centerRadius=$ASMRadius
radiusCut=$ASMRadius-160
##### Remove the line-break between centerRadius and radiusCut before compiling

##### Place virtual detector at end of ASM12
place MuSEDet z=$PASM2-775.39+$L_center_line_ASM+10+0.5*$MuSEDetLength+2
rename=Det5
##### Remove the line-break between z and rename before compiling

##### Define QSL15 parameters
param LDRIFT11=684
param BQSL15=0.5440*$scale*$scaleQSL
param GradBQSL15=$BQSL15/$RQSL*$kGpmm_to_Tpm

##### Place QSL15 at 17246.6 mm wrt. ProdTarget @ -958 mm. 17246.6+958mm=18204.6 mm
param PQSL15=$PASM2+0.5*$L_center_line_ASM+$LDRIFT11+0.5*$LQSL
place QSL rename=QSL15 gradient=$GradBQSL15 z=$PQSL15

##### Define QSL16 parameters
param BQSL16=-0.7506*$scale*$scaleQSL
param GradBQSL16=$BQSL16/$RQSL*$kGpmm_to_Tpm
param LDRIFT12=112

##### Place QSL16 at 17948.6 mm wrt. ProdTarget @ -958 mm). 17948.6+958mm=18906.6 mm
param PQSL16=$PQSL15+$LQSL+$LDRIFT12
```

```
place QSL rename=QSL16 gradient=$GradBQSL16 z=$PQSL16

##### Define QSL17 parameters
param BQSL17=0.9086*$scale*$scaleQSL
param GradBQSL17=$BQSL17/$RQSL*$kGpmm_to_Tpm
param LDRIFT13=1038

##### Place QSL17 at 19576.6 mm wrt ProdTarget @ -958 mm. 19576.6+958 mm=20534.6 mm
param PQSL17=$PQSL16+$LQSL+$LDRIFT13
place QSL rename=QSL17 gradient=$GradBQSL17 z=$PQSL17

##### Define QSL18 parameters
param BQSL18=-1.2732*$scale*$scaleQSL
param GradBQSL18=$BQSL18/$RQSL*$kGpmm_to_Tpm
param LDRIFT14=163

##### Place QSL18 at 20329.6 mm wrt ProdTarget @ -958 mm. 20329.6+958 mm=21287.6 mm
param PQSL18=$PQSL17+$LQSL+$LDRIFT14
place QSL rename=QSL18 gradient=$GradBQSL18 z=$PQSL18

##### Place virtual detector at PiM1Target
param targetLocation=22159.5
place MuSEDet z=$targetLocation rename=DetTar

##### Place virtual detector at beam hodoscope before PiM1Target.
place MuSEDet z=$targetLocation-1000 rename=DetBH
place SHIELD rename=SHIELD_TAR z=$targetLocation innerRadius=2*$MuSEDetRadius
outerRadius=2.1*$MuSEDetRadius length=5000
##### Remove the line-break between innerRadius and outerRadius before compiling

##### Place virtual detectors (beam counters) after PiM1Target.
place MuSEDet z=$targetLocation+1500 rename=DetBC1

place MuSEDet z=$targetLocation+2500 rename=DetBC2
```

```
##### Write the output file
ntuple partOut detectors=Det* require=DetTar
```

Appendix E: Momentum Loss Simulations

In this Appendix we show the Geant4 simulations of how the momentum spectra of beams of different particles are changed by energy loss effects at the IFP. Note that the vertical scale of the plots is logarithmic. In all cases we start with a monochromatic pencil beam. The simulations are done both with and without GEM planes installed. The initial momentum is shown in red. The momentum distribution after passing through the IFP material is in black. The range of the plots is limited to particles likely to be able to pass through the ASM12 bending dipole and reach the target region. We show only a pencil beam with no dispersion; a full simulation with up to $\pm$ 0.05% momentum dispersion showed less than a 10^{-3} effect on the mean momentum loss.

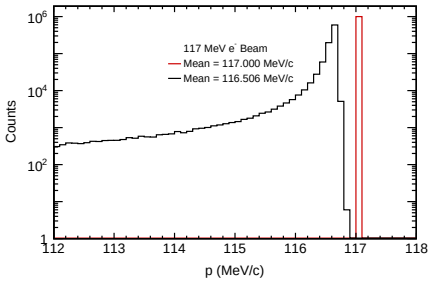

(a) e momentum loss.

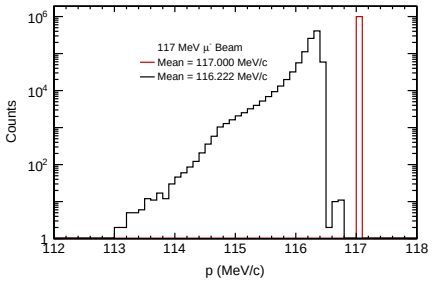

(b) μ momentum loss.

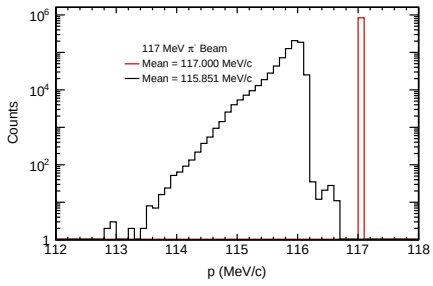

(c) π momentum loss

FIG. 62: Momentum loss using a $-117\,\mathrm{MeV/c}$ pencil beam through the IFP with GEMs.

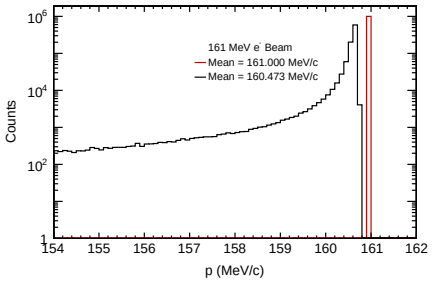

(a) e momentum loss.

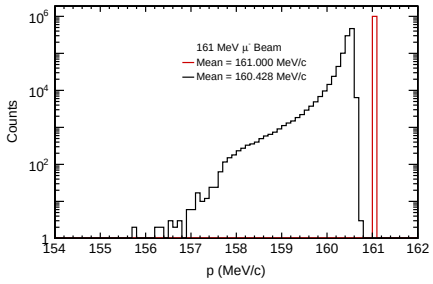

(b) μ momentum loss.

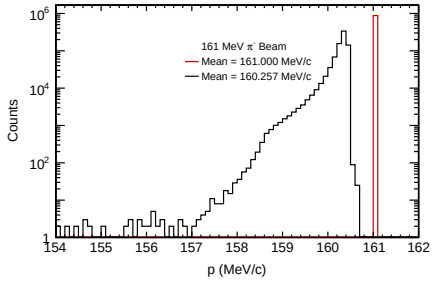

(c) π momentum loss

FIG. 63: Momentum loss using a $-161\,\mathrm{MeV/c}$ pencil beam through the IFP with GEMs.

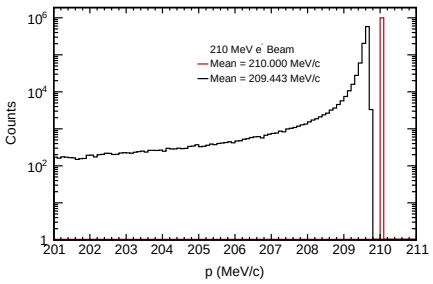

(a) e momentum loss.

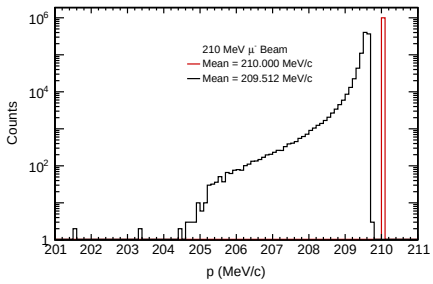

(b) μ momentum loss.

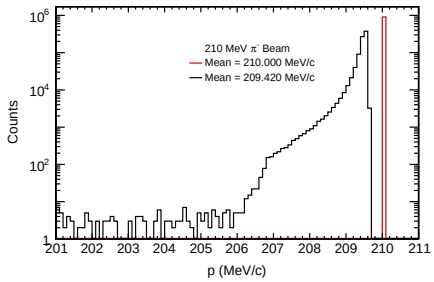

(c) π momentum loss

FIG. 64: Momentum loss using a $-210\,\mathrm{MeV/c}$ pencil beam through the IFP with GEMs.

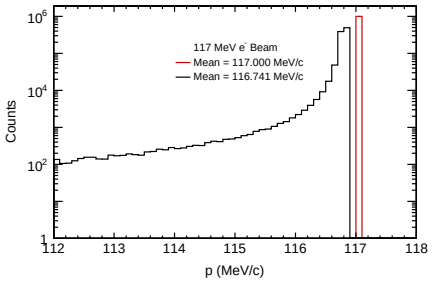

(a) e momentum loss.

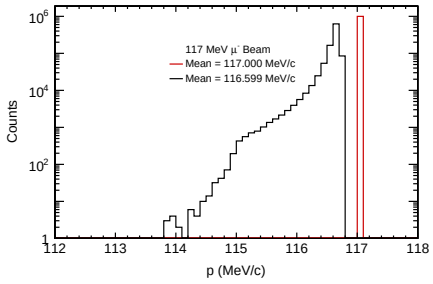

(b) μ momentum loss.

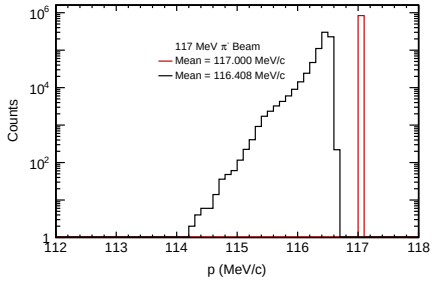

(c) π momentum loss

FIG. 65: Momentum loss using a $-117\,\mathrm{MeV/c}$ pencil beam through the IFP, without GEMs.

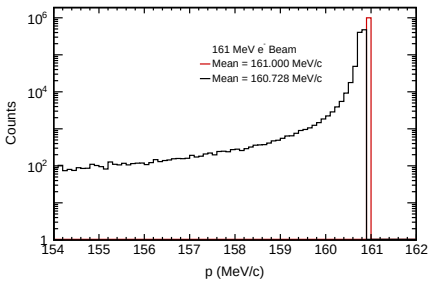

(a) e momentum loss.

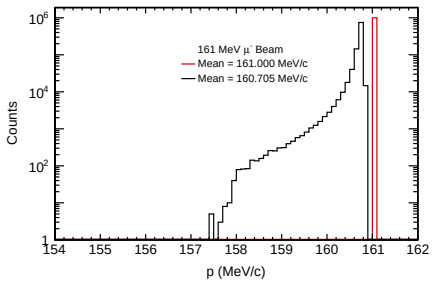

(b) μ momentum loss.

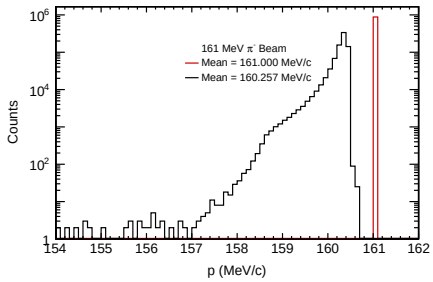

(c) π momentum loss

FIG. 66: Momentum loss using a $-161\,\mathrm{MeV/c}$ pencil beam through the IFP, without GEMs.

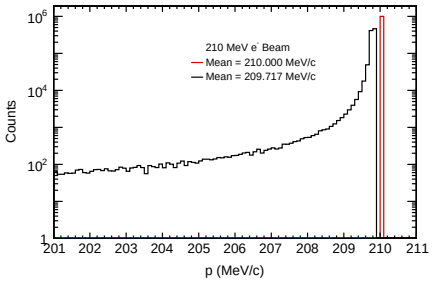

(a) e momentum loss.

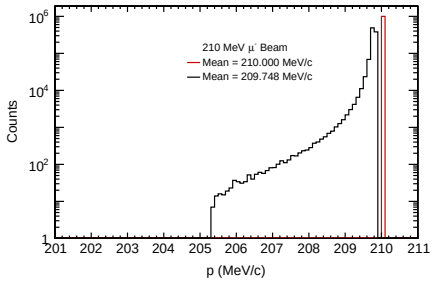

(b) μ momentum loss.

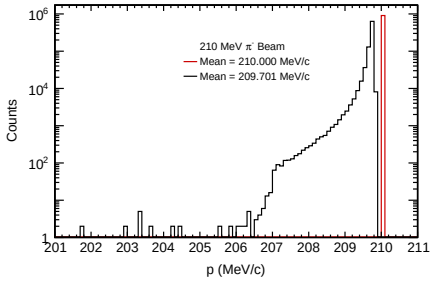

(c) π momentum loss

FIG. 67: Momentum loss using a $-210\,\mathrm{MeV/c}$ pencil beam through the IFP, without GEMs.

[1] K. Brown and C. Iselin, (1974), dECAY TURTLE, CERN Report 74-2.

[2] F. Berg *et al.*, Phys. Rev. Accel. Beams **19**, 024701 (2016).

[3] A. Knecht, (2017), private communication.

[4] T. Roberts, (2018), `http://www.muonsinternal.com/muons3/G4beamline`.

[5] S. Agostinelli *et al.* (GEANT4), Nucl. Instrum. Meth. **A506**, 250 (2003).

[6] R. Molloy and S. Blitz, (2013).

[7] S. Incerti *et al.*, Medical Physics **45**, e722 (2018).

[8] D. Wright and M. Kelsey, Nuclear Inst. and Methods in Physics Research A **804**, 175 (2015).

[9] R. Gilman *et al.* (MUSE), (2017), arXiv:1709.09753 [physics.ins-det].